2016

FLOW VISUALIZATION OF BUOYANT INSTABILITY IN A CROSS-FLOW: AN IMPLICATION FOR FLAME SPREAD OVER FOREST FUEL BEDS

Nikolay Gustenyov
University of Kentucky, nikolaygustenyov@gmail.com
Digital Object Identifier: http://dx.doi.org/10.13023/ETD.2016.073

STUDENT AGREEMENT:

I represent that my thesis or dissertation and abstract are my original work. Proper attribution has been given to all outside sources. I understand that I am solely responsible for obtaining any needed copyright permissions. I have obtained needed written permission statement(s) from the owner(s) of each third-party copyrighted matter to be included in my work, allowing electronic distribution (if such use is not permitted by the fair use doctrine) which will be submitted to UKnowledge as Additional File.

I hereby grant to The University of Kentucky and its agents the irrevocable, non-exclusive, and royalty-free license to archive and make accessible my work in whole or in part in all forms of media, now or hereafter known. I agree that the document mentioned above may be made available immediately for worldwide access unless an embargo applies.

I retain all other ownership rights to the copyright of my work. I also retain the right to use in future works (such as articles or books) all or part of my work. I understand that I am free to register the copyright to my work.

REVIEW, APPROVAL AND ACCEPTANCE

The document mentioned above has been reviewed and accepted by the student's advisor, on behalf of the advisory committee, and by the Director of Graduate Studies (DGS), on behalf of the program; we verify that this is the final, approved version of the student's thesis including all changes required by the advisory committee. The undersigned agree to abide by the statements above.

Nikolay Gustenyov, Student

Dr. Kozo Saito, Major Professor

Dr. Haluk Karaca, Director of Graduate Studies

FLOW VISUALIZATION OF BUOYANT INSTABILITY IN A CROSS-FLOW: AN IMPLICATION FOR FLAME SPREAD OVER FOREST FUEL BEDS

THESIS

A thesis submitted in partial fulfillment of the requirements for the degree of Master of Science in Mechanical Engineering in the College of Engineering at the University of Kentucky

By

Nikolay Gustenyov

Lexington, Kentucky

Director: Dr. Kozo Saito, Professor of Mechanical Engineering

Lexington, Kentucky

2016

ABSTRACT OF THESIS

FLOW VISUALIZATION OF BUOYANT INSTABILITY IN A CROSS-FLOW: AN IMPLICATION FOR FLAME SPREAD OVER FOREST FUEL BEDS

This thesis reports small-scale laboratory experiments designed to visualize the flow over a heated plate. A low-speed wind tunnel was built, and a heating plate was flush mounted on the wind tunnel floor to provide a uniform heat flux over its surface. A paper thin cloth soaked with commercially available Vaseline was placed on top of the heating plate to produce thick smoke streaks that were carried downstream by a horizontal airflow. Both LED light and a laser sheet of approximately 30-degrees open angle were separately used to illuminate this flow, the latter advanced downstream with 1-cm interval from the heated plate's upstream edge. A camera with full-frame CMOS sensor recorded time series of flow patterns from four different angles. From these images, the following four flow structures were identified: (1) organized horizontal flow of vortex tubes, (2) weak vortex tubes interactions, (3) strong vortex tubes interactions (transition regime), (4) chaotic turbulent flow. Flow structure analysis showed that smoke flow height increased with horizontal distance from the heated plate and reduced with flow velocity. Scaling analysis was conducted to assess the validity of observed scale model flow structure to the USDA Forest Service medium scale wind tunnel burns.

KEYWORDS: Fire Research, Flow Visualization, Fire Spread, Scaling Laws, Vortices

Nikolay Gustenyov

April 21, 2016

FLOW VISUALIZATION OF BUOYANT INSTABILITY IN A CROSS-FLOW: AN IMPLICATION FOR FLAME SPREAD OVER FOREST FUEL BEDS

By

Nikolay Gustenyov

Dr. Kozo Saito
Director of Thesis

Dr. Haluk Karaca
Director of Graduate Studies

April 21, 2016

ACKNOWLEDGMENTS

Although this thesis is an individual work, the following people have made significant contribution in ensuring success of the project. Dr. Kozo Saito shared his great experience in combustion and scale modeling to support my exploration of the theory behind the phenomena observed. Dr. Nelson Akafuah provided organizational support and guided me in the laboratory work. Dr. Ahmad Salaimeh greatly contributed in visualization and data post processing. Dr. John Stencel provided instructive comments and evaluation of the work done in order to achieve the best possible result. Dr. José Graña-Otero, his lectures expanded my knowledge in the Engineering Field and he was always kind to give an advice and answer my questions inside and outside the class. I would also like to thank Dr. Mark Finney and Dr. Sarah McAllister from the USDA Missoula Fire Sciences Laboratory for providing the necessary data and help in brainstorming. Despite the fact that all people above are much more experienced than me, they gave me just enough freedom to develop my own view of the problem. All IR4TD members supported me as a family throughout my time in graduate school.

TABLE OF CONTENTS

LIST OF TABLES

LIST OF FIGURES

NOMENCLATURE

u	horizontal wind velocity
v	vertical velocity component of gas flow
L_w	depth of the flame zone
L_f	average flame height
L_a	average plume height
ρ_1	density of combustible gases and air
$\Delta\rho_1$	density change of combustible gases and air
ρ_2	density of unburnt fuel
H	height of discrete fuel particles (fuelbed)
L_e	preheating length (distance ahead the flame where significant heat transfer occurs)
ω	frequency factor (represents time dependent behavior/instability such as vortex shedding)
l_2	distance between two valleys or width of a flame tower
l_c	length of crib sticks
b_c	thickness of crib sticks
b_o	space between crib sticks
Θ_1	temperature of combustible gases and air
$\Delta\Theta_1$	temperature change of combustible gases and air
Θ_2	temperature of burning materials
$\Delta\Theta_2$	temperature change of burning materials
q_f	heat value per unit mass of crib materials
Q_λ	latent heat per unit mass of crib materials
c_p	specific heat of combustible gases and air at atmospheric pressure
c_2	specific heat of crib materials
t	time scale
g	acceleration due to gravity
E	irradiance received by radiometer
J	mechanical equivalent of heat

F_i	inertial force of air and gas
F_b	buoyant force of air and gas
Q	heat generated
Q_r	radiant heat received by unburnt fuel
Q_{c1}	heat stored in air and gas associated with temperature rise
Q_{c2}	heat stored in unburnt fuel
I	fire intensity
λ	latent heat per unit mass of fuel
$Ø$	ratio of consumed fuel to the total fuel available
R	horizontal fire spread velocity
w	downstream pulsing frequency
$F_{i,up}$	inertial force in the upstream location
$F_{i,down}$	inertial force in the downstream location
D	dimension of fuel particle
a	thermal diffusivity

CHAPTER 1: INTRODUCTION

1.1 Motivation for research

Wildland fire is a general term describing any non-structure fire that occurs in a natural landscape. These fires can be extremely destructive events leading to significant social and economic losses, especially at wildland-urban interfaces where large amounts of resources are utilized to protect people's property. Expenses related to wildland fires, including preventative measures such as early fuel management strategies (thinning, harvesting, mechanical treatments and prescribed burning), are continuously growing [11]. Fire suppression is the most obvious cost associated with wildfires; between 1991 and 2000 the U.S. Forest Service spent an average of $580 million annually while from 2001 to 2010 this figure doubled to $1.2 billion. Moreover, state budgets related to wildland fire fighting have also increased; according to the National Association of State Foresters (NASF), the annual expenses by state forestry agencies in 2008 exceeded $1.6 billion [1]. In addition, considerable costs are incurred to restore the losses and damage caused by wildfires. However, money is unimportant compared to human injuries or death; life lost is the most tragic consequence of fires.

In reality, wildland fires are an integral part of establishing and maintaining a healthy ecological balance in forests and grasslands. This enlightenment was a result of research started in 1920's; it identified changes in ecological conditions in the western US which were ascribed to fire suppression efforts and in which considerable changes in the structure, composition and fuel loads in forests were documented to adversely influence fire severity in comparison to previously experienced frequent but low-to-moderate-intensity wildfires [2]. In 1910 Hoxie proposed control burns in California forests every 1-3 years [7]. Later, in 1924, Lee supported this idea by proposing "If the fire is not too severe, the burning may be beneficial to forest succession, as light fires usually help to kill back the underbrush, open resinous cones, stimulate germination and encourage the development of the major forest tree species" [3]. Others also found ecological and financial advantages of more frequent and less intense wildland fires that could be considered to be part of nature [4-6, 8]. Almost twenty years later in the 1940's, the US Department of Forestry started using controlled fires as a silviculture tool in

Southwest US where Native American culture, which supported light fires, was dominant [9]. Any fire is potentially dangerous; even a controlled fire can lead to a disaster. However, nowadays, forestry agencies don't only fight wildfires but also use them to maintain ecological balance. As a result, controlled burns and even wildland fires have to be assessed relative to their design or impact and then controlled in a manner providing ecological, safety and economic benefits.

Even with large expenditures and the substantial infrastructure dedicated to fire suppression in the US, the amount of area burned annually by wildfires has increased during the last decade [10]. Furthermore, despite the fact that people have been dealing with wildfires for centuries, the mostly unpredictable and extreme behavior of wildfires significantly complicates assessments of how to respond and then the impact of any response. This difficulty motivates research into wildland fires even more because predicting the path of wildfires is extremely important in the efforts of forestry services and fire managers. Reliable predictions of wildland fires' behaviors could save lives as well as reduce costs of such events; needed within such predictions are improved fire spread models which can improve firefighting strategies [12]. Also, understanding wildfire spread mechanisms is paramount because, although the heat transfer mechanism controlling fire spread are generally well-studied, they are still under question for wildland fires. To answer this question, the mechanisms that govern ignition and flame spread under different conditions have to be investigated and the role of radiation and convection must be identified [13, 14].

With a deeper knowledge in the basic fire spread mechanisms and combustion principles controlling them, predictive capabilities would be enhanced which will result in an improvement in the efficacy, efficiency and safety associated with strategies used to control prescribed fires and wildfires. However, the measurement data needed for a better understanding of wildfire behavior are typically not accessible because it is not possible to instrument these fires. Nevertheless, laboratory-scale fire experiments under certain conditions have showed behavior similar to real wildland fires [59]; this correspondence means that both of them are governed by the same physics and, importantly, perhaps

carefully planned and studied laboratory-scale fires can offer the insight needed to improve understanding the mechanisms of wildfire spread.

1.2 Fire research

1.2.1 Ignition and fire spread

Initially, investigations of fire spread were motivated by a need of improving fire suppression strategies [14, 15]. Significant amounts of data are available that relate to wildfire behavior, however most studies have been limited by uncertainties in conditions, like type of fuel, moisture contents and weather conditions. Mathematical models have been developed to predict fire behavior that use known fuel properties such as load, bulk density, fuel particle size, heat content and moisture. For instance, Rothermel's surface fire spread model utilized its own fuel model [16, 17] but the variety of wildland fuels that exist and the possibility of rather quick changing weather patterns can dramatically reduce the predictive capabilities of such a model. In fact, most current wildfire behavior models are based on full-scale observations which correlate, for instance, fire spread rates with the fuel type and weather conditions instead of dealing with the fundamental physics controlling behavior. Hence, an extreme need yet exists for investigating and understanding the fundamental physics governing wildfire spread [14].

Since wildfires normally consume solid fuels such as wood, this particular type of fuel was considered in this thesis. To start the oxidation reaction, i.e. ignition, enough thermal energy must be transferred to the fuel particle. This energy or heat stimulates the emission of combustible pyrolysis gases from the particle's surface which then react with oxygen from surrounding air and ignites, burning with a heat release rate larger than the rate of heat loss to the environment [13, 14]. Part of the released heat is transferred to the unburnt fuel particles and the ignition cycle, which then creates conditions for continuous fire spread [18].

Fuel ignitability is crucial for initiating and sustaining wildfires [19], and is started through either spontaneous or piloted ignition. Spontaneous ignition occurs without interaction between an external pilot flame and unburnt fuel; this type of ignition requires intense heat flux to sustain burning and therefore is rare. In contrast, piloted ignition is the dominant mechanism because of the presence of radiation and convection

heating of unburnt fuel plus its interaction with open flame [20]. Due to the contact between the flame and the unburnt fuel, piloted ignition can occur at lower temperatures and is responsible for wildfire spread.

Figures 1.1 presents a pictorial scene of fire spread through a fuelbed made of cardboard tines that are oriented vertically and evenly distributed along a horizontal surface; Figure 1.2 shows a temperature-versus-time plot of the tines in the fuelbed. Flame propagation through the discrete fuelbed in Figure 1.1 is through a series of ignitions of spatially separated but consecutive fuel particles. The process of preheating of a single particle (tine) to its ignition temperature can be divided into three stages.

- During the first stage, the flame approaches a particle (circled in blue). Due to low-intensity heat transfer at this stage, temperature of the particle increases by only a few degrees.
- During the second stage, the fire front is closer to the particle with a distance that enables the flame to occasionally touch or lick the particle. Flame licking causes temperature peaks during this stage but the temperature of the air between the licking events tends to be lower than temperature of the particle (Figure 1.2). Therefore, the average temperature of the particle increases gently because convective cooling of the particle takes place between peaks.
- During the third stage, the last stage prior to ignition, the average temperature of air is higher than particle's temperature because flame licking occurs more and more often and the time between peaks is smaller than the width of the temperature peaks shown in the Figure 1.2. While convective cooling still occurs during stage 3, convective heating of the particle is dominant. As a result of the temperature rise, combustible pyrolysis gases accumulate around the leeward side of the particle.
- Ignition takes place after the concentration of pyrolysates attain a critical level; the flame initially attaches to the top of the leeward side of the particle and then propagates downward [14, 51].

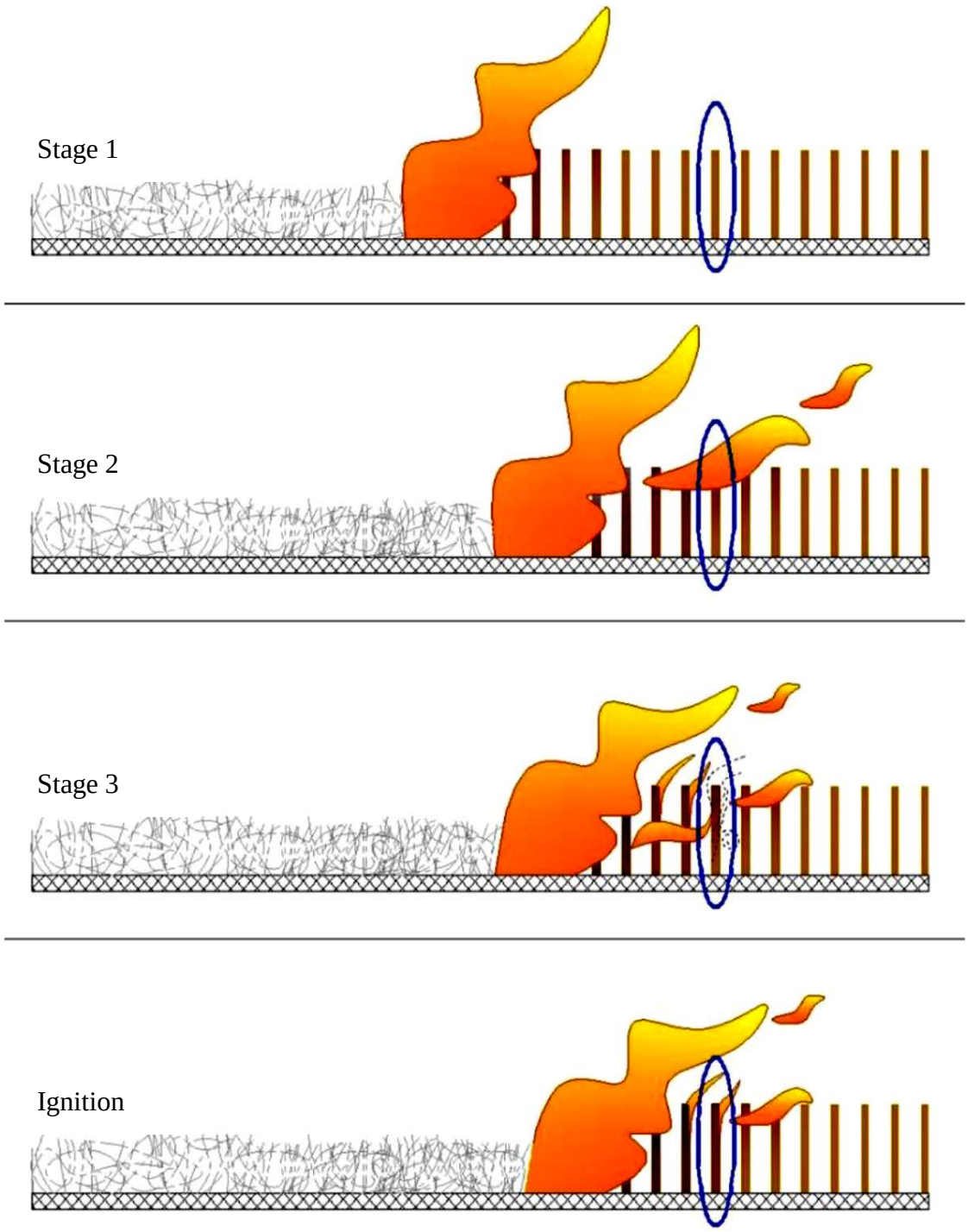

Figure 1.1 The three stages leading to ignition of a fuel particle in a discrete fuelbed [90].

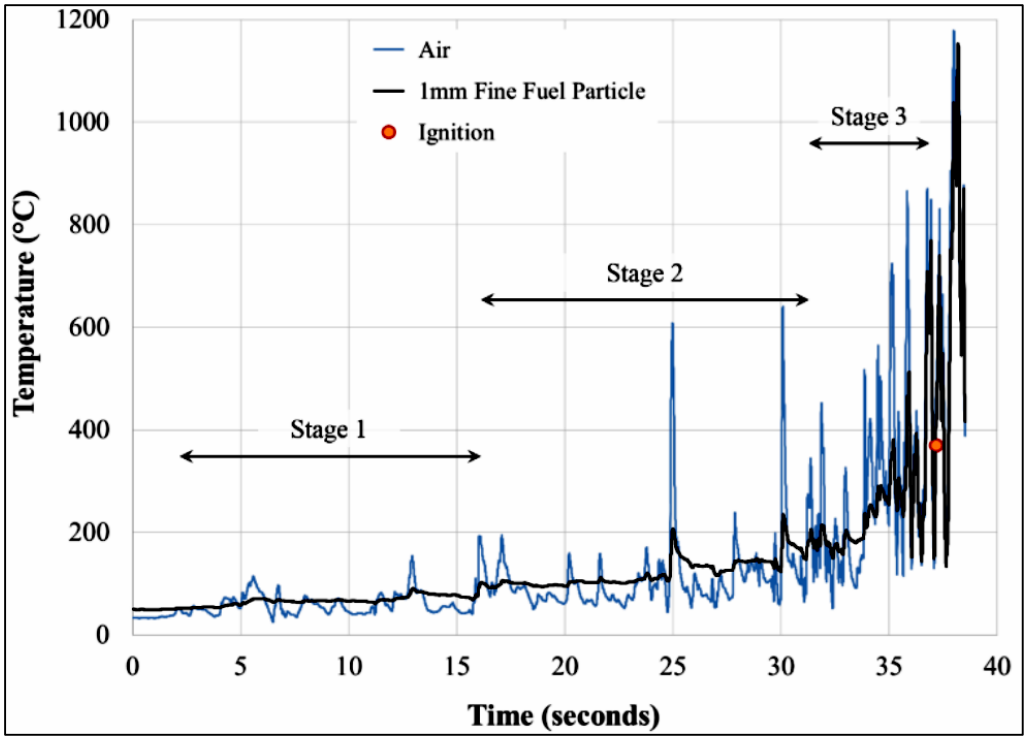

Figure 1.2 Temperature history of a particle and air surrounding it in a fuelbed [90].

It is a common practice to assume that ignition of a fuel takes place at a fixed temperature [14] if a specific, controlled condition for ignition and a particular fuel are used. However, application of a fixed ignition temperature for wildfires may not be possible due to the complexities of the heating regime, and environmental and fuel conditions [21, 22].

1.2.2 Governing heat transfer mechanisms

The transfer of heat from a source to an unburnt fuel is one of the main governing phenomena in fire spread. Defined as the energy exchange within or between media caused by temperature gradients, heat transfers from hot to cold but not reverse. The three modes of heat transfer include conduction, convection and radiation. Temperature gradients within fluids drive the so-called buoyancy force which leads to fluid motion. In fluid mechanics this motion is called convection which represents mass transfer within a fluid. However, in thermodynamics term “convection” normally means convective heat transfer. Heat transfer by convection occurs either on a large scale by a moving heated fluid (advection) or on a small scale through thermal diffusion associated with the random motion of molecules and their interactions which transfers kinetic energy.

Convective heat transfer is tied with fluid mechanics, and if gas flow efficiently transfers thermal energy from a source to an unburnt fuel, flame propagation will occur. All three modes of heat transfer (radiation, conduction and convection) contribute to wildfire spread but in different ways [23].

Because wildland fuel is normally considered to be discrete, conduction is usually assumed to be negligible due to a lack of contact between fuel particles [13]. Additionally, the interior of large fuel pieces such as trees acts as a heat sink which takes heat from the particle's surface and reduces emission of pyrolysis gasses and its burning potential [24]. In contrast, both radiation and convection are responsible for heat transfer from flames to the unburnt fuel, and thereby contribute to fire spread. Generally, it has been assumed that radiation provides the energy needed to sustain pyrolysis reactions and burning, while convection supplies the energy required to preheat unburnt fuel ahead of the flame front to its ignition point and to bring new fuel to the fire [24].

Historically, a majority of scientists assumed radiation to be the main heat transfer mechanism for wildfire spread [25-35]. Radiation was also assumed to be dominant for upward flame spread along a vertical wall under natural convection and fire propagation through a horizontal, continuous fuel bed under a high horizontal wind [36-38]. A rational for this assumption [25] was that a well-developed flame zone would block surrounding winds and therefore prevent the ignition of adjacent fuel from convective heating. However, fire spread models introduced by Weber and Sullivan included both radiative and convective heat transfer modes [39-46]. Butler et al. [49] proposed that convective cooling of the fuel particle's surface tends to be significant as fire approaches and, as a result, convective heating could be extreme immediately before and at the ignition time. Emori and Iguchi et al. [47], studying flame spread through horizontal and inclined fuel beds made of excelsior and vertically oriented paper strips coated with candle wax, showed that flame spread in these cases was governed by convection. Additionally, Emori and Saito focused on understanding how the spread of convection driven fires was different than the spread of radiation driven fires [50]. They showed that a pool fire is driven by radiation whereas a wooden crib fire is driven by convection, and that these differences have to be considered in the governing principles of flame

propagation. Recently, Finney et al. [14, 58] further developed the idea that, before ignition, convective heat transfer either from direct flame impingement or natural convective heating circulation played a more substantial role than previously believed in wildland fire spread. For example, laboratory ignition tests [59] on live pine needles in which heating was accomplished by radiation or convection showed that the pine needles could not be ignited by radiation alone even at heat fluxes as high as 80 kW/m^2 for periods of 10 minutes [59, 60]. In contrast, these live pine needles exposed to a convective heating flux of 25 kW/m^2, a value less than 1/3rd of that used during the radiation heating tests, ignited in less than 10 seconds. Based on these and other test results, the following was concluded: "Convective cooling of the fine-sized fuel particles in wildland vegetation is observed to offset efficient heating by thermal radiation until convective heating by contact with flames and hot gasses occurs." [59]

1.3 Present research objectives

The goal of this study was to determine the applicability of non-reactive flow experiments in fire research and apply scaling laws to correlate three different scales of experimentation (small-scale non-reactive flow, middle-scale burning in a wind tunnel and full-scale wildfire). Additionally, infrared visualization of convective-driven ignition of a wood sample was of strong interest.

1.3.1 Advantages of using infrared thermography

Figures 1.1 and 1.2 show the three stages of heating a fuel particle to its ignition temperature. However, a particle's response to an approaching fire during stages 1 and 2 is invisible to the human eye. Even during the stage 3, when a particle surface turns black, the vision offered by the human eye cannot offer information about processes which occur on the particle surfaces because temperature changes have to be understood. Thermocouples can be used to measure temperature changes but have severe limitations because it is necessary to attach the thermocouple to the surface of the particle if accurate temperatures are to be acquired. The need of the attachment of thermocouples makes utilization in fire experiments difficult because solid fuel particles change shape (bend, expand or shrink) during heating and ignition. Thermocouples also measure temperatures at the point of attachment, a very small area relative to the total area of a particle.

Therefore, if heat propagation through a fuel particle is to be tracked during heating and ignition with thermocouples it would be necessary to attach a number of thermocouples along the body of each particle. This requirement significantly complicates experimental procedures.

Infrared thermography is a possible alternative to thermocouples. It has already become popular in heat transfer and fluid dynamics research mainly because of its non-contact capabilities for measuring temperature [52] and allows visualization of infrared radiation emitted from the surface of objects. The emitted thermal energy is affected by the surface characteristics (emissivity) as well as its temperature [53]. Relative to wildfire research, infrared thermography is particularly beneficial in investigating heat transfer processes within a fuelbed during fire propagation [54]. It was successfully applied to investigate the transient pyrolysis location in upward spreading flame along wood and PMMA samples [55, 56] and sub-surface layer defects [57].

Naturally, there are limitations in applying infrared thermography in fire research. Some properties of solid fuels such as emissivity change during combustion and these changes complicate the measurement of accurate temperatures. Infrared cameras are usually calibrated using a “black” body of known temperature; the emissivity of a “black” body is one. The emissivities of other surfaces are normally lower than one and this difference between the value of one for an ideal “black” body and the actual emissivity of a surface has to be considered to obtain accurate temperature readings.

Wood is one of the main types of fuel consumed by wildfire and wood samples have been used in fire experimentation. According to variety of sources, emissivity of wood is between 0.65 and 0.95 [124–126], depending on type of wood. This range of emissivity values gives certain inaccuracy in temperature readings when different types of wood are burned. The effect of emissivity variation was studied during the research for this thesis, as is described in Chapter 3.

1.3.2 Elimination of chemical reaction to visualize and study gas motion caused by the interaction of horizontal flow and buoyancy-induced flow

While some studies are focused on chemistry of combustion or heat transfer mechanisms, fluid dynamic aspect of fire behavior was of particular interest for this

thesis. Depending on ambient conditions, gas flow around flames can be laminar, transitional or turbulent; these flow regimes result in different gas behavior within the flame [61]. In wildfire applications, the flow is normally considered to be turbulent [62]. Because the oxidizer (air) and the fuel (pyrolysis gases) are not initially premixed, wildfire flames are classified as a diffusion type. In laminar diffusion flames, buoyant convection is an agent which transports burn products from the flame and replaces them with oxygen (fresh air) to sustain the reaction [64]. Recently, Finney et al. [14, 58] stated that wildfires are essentially dynamic but the causes and mechanisms of their nature are yet not well investigated. The dynamic interactions between the flame, fuel and the gas flow field instill difficulties in wildfire research that may not be present in other types of fires [65].

Unsteady flame behaviors, such as flickering, pulsing and vortex shedding, that are caused by the interaction between the diffusion flame and gas flow has been observed many times in flames originating from circular nozzles or jets, as well as in wildfires [66-71]. The presence of wind has a critical effect on wildland fire behavior - it causes time dependent vortex shedding which improves convective heat transfer capabilities [72-74]. Therefore, the study of convective heat transfer from a static, or time-averaged, perspective cannot address important questions and, as a result, would prevent accurate predictions of wildfire behaviors.

A series of wind tunnel, fire spreading experiments using engineered cardboard fuelbeds have been conducted [59] in which two dynamic features were identified within the flame zone, including convective peaks and valleys separated by regular spacings that moved back-and-forth in a span-wise direction in the flame (Figure 1.3); the number of columns depended on the fuel properties and fuelbed geometry. The same type of behavior was observed in the progressing front of a wildfire when the flame split into columns. This behavior is of paramount interest in this thesis because, although most previous laboratory fire studies have used a well-defined fuel under controlled environments in conjunction with the use of scaling laws [90], no results have been reported in which the complicating effects of chemical reactions associated with flames have been eliminated from the investigations. Hence, this work focuses mainly on fluid

dynamic aspects of fire spread by eliminating the chemical reactions of flames by using an electrical heater as the thermal energy source.

Eliminating the chemical reaction significantly simplifies the study of dynamics; additionally, the use of electrical heater allows precise temperature control. Moreover, investigating and understanding the role of buoyancy forces becomes easier when temperatures are known precisely without chemical reactions and makes it possible to apply scaling laws with variable temperatures and heat fluxes. Hence, Chapter 2 includes an overview of scaling laws used in fire research plus assumptions that are made for the current study.

Importantly, the absence of a flame permits visualization of the flow field which is normally masked by it. While other fire experiments mostly have concentrated on the flame itself, the objective of the present work is to study fluid dynamic mechanisms in the absence of a flame, using visualization as one of the main tools of investigation. Therefore, this thesis introduces a new approach for investigating the time-dependent nature of fire behavior and the role of convection heat transfer in fire spread with a main motivation to define the distance ahead of a fire front where convective heat transfer is effective.

Detailed experimental method and results are discussed in Chapter 4, plus suggestions for the future study are given in Chapter 5.

Figure 1.3 Peaks and valleys in propagating fire front [90].

CHAPTER 2: SCALE MODELING IN FIRE RESEARCH

2.1 Introduction to Scale Modeling

Scale modeling has been developed to study and provide insight into physical phenomena. The idea is to identify the physics governing a phenomenon, such as force, energy, inertia and momentum, and then to develop dimensionless numbers called Pi-numbers or Pi-groups which represent relationships between characteristic parameters of the phenomenon. A scale model is an experimental model of a full-scale or prototype system that is designed to represent the essential physical behavior of a full-scale or prototype system; scale models enable the demonstration of behaviors or properties of an original system without examining it in its full-scale. Scale modeling identifies governing mechanisms of a phenomenon and then helps to expand the understanding of it. Scale modeling also allows experiments to be conducted in a representative manner by using a usable scale or size when prototypes or full-scale are either too large or small to be readily studied [83]. A common practice is to use scale modeling for simplifying a phenomenon and for studying its essential physics [84].

A fundamental requirement of scale modeling is that the model and the prototype are governed by the same physics [85]. First, a detailed analysis of the original phenomena is required to define the important governing mechanisms and those which may be insignificant and can be ignored. This analysis step is essential and is the most challenging step in scale modeling [86]. Second, accurate relationships between parameters which characterize the original phenomenon must be developed [87]. These relationships are a set of dimensionless products of the governing parameters (Pi-numbers) and are called the function relationships [50, 84, 88, 89]. A scale model can be considered to be valid if each Pi-number associated with it has a corresponding prototype Pi-number that is related to the scale model via a multiplicative constant (scale factor).

Unfortunately, it is exceedingly difficult to scale a physical phenomenon considering all parameters involved. Therefore, partial modeling is normally applied which considers parameters of primary importance [85]. As depicted in Figure 2.1, during partial modeling, a limited set of assumptions are developed which then have to be validated through an experimental scale modeling study to compare experimental

outcomes with the prototype. Additional validation may be accomplished via computational techniques [114]. Overall, if similarities between the prototype and scale model are not strong, then the assumptions used during the development of the important parameters and relationships must be reviewed.

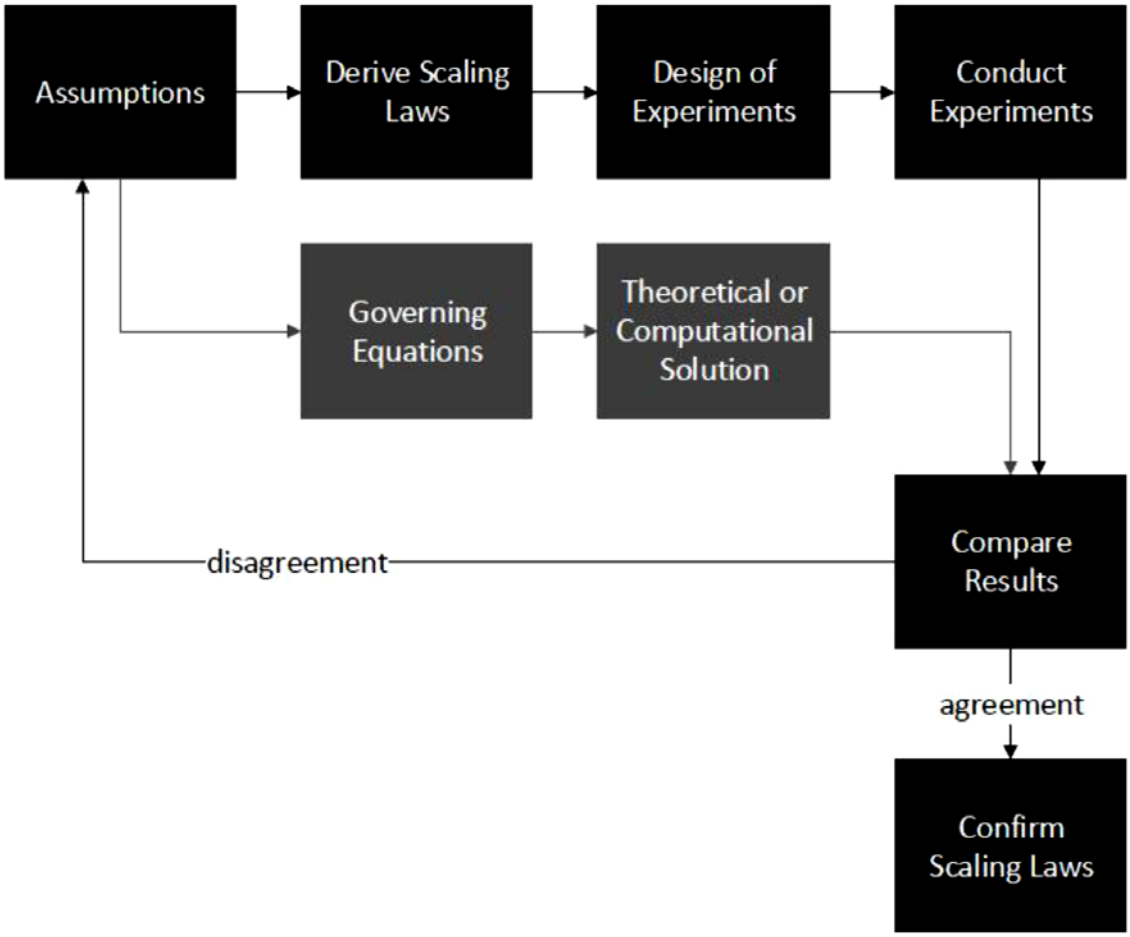

Figure 2.1 Steps in scale model development [83, 84, 90].

According to Saito [91], there are three approaches in developing scaling laws, including:

1. Parameter approach;
2. Equation approach;
3. Law approach.

The parameter approach is based on Buckingham's Pi theorem [92, 93] and is sometimes referred as the “Pi-theorem” or “method of repeating variables” [90]. It was

initiated by Aimé Vaschy, Dimitri Riabouchinsky, and Lord Rayleigh (John William Strutt), but comprehensively presented by E. Buckingham in 1914 [90, 93-96]. This approach involves a number of parameters which characterize the phenomenon and form dimensionless groups (Pi-numbers) which are used to accomplish scaling.

The equation approach starts with derivation of governing equations and specification of the boundary conditions of the phenomenon. Since governing equations are dimensionally homogeneous, the involved parameters can be arranged in dimensionless groups [84, 94]. Williams used this approach in 1969 to form 28 Pi-groups related to fire scaling [97]. The inherent beauty of this approach is that the governing equations can completely describe the phenomenon and, therefore, all components are conserved during formation of the dimensionless Pi-groups [7]. However, the applicability of the equation approach is limited to cases where the governing equations are either well known or can be accurately stated.

The law approach begins with a quantitative analysis of forces, energies and masses involved in the phenomenon [84]. Hottel advocated for the law approach in 1959 because he believed that the parameter approach and Buckingham's Pi theorem led to misunderstandings in scale modeling that introduced variables without identifying their physical meaning [85]. Hottel also expressed his disappointment in the equation method because it requires well-developed governing equations to derive the scaling laws even though these governing equations are not a fundamental requirement for scaling [85].

The use of the law approach in scaling fires has been supported by numerous studies [85, 99, 100]. Moreover, wildfire scientists who have studied the role of buoyancy forces in fire front behavior have also established initial sets of laws for such wildfire investigations. Nevertheless, a number of examples exist in which both parameter and equation approaches have been successfully applied to fire research [101, 50, 100]. Although Emori was the pioneer of the law approach, he used the parameter approach in his fire research because the audience in this arena was familiar with it. Importantly, he developed the same Pi-groups using law and parameter approaches which suggested that, once the assumptions are correct, reliable scaling laws can be derived using any of the approaches [83].

2.2 Scale modeling in fire research

As discussed in Chapter 1, instrumenting of large scale fire is complicated or even impossible due to lack of control and the danger of the event. In contrast, laboratory environments are much easier to control and safer. Hence, many scale model methods have been established that use a variety of fuels, including match sticks, excelsior, plywood, cardboard, paper, live and dead fuels, wood cribs of different packing densities and liquid fuels. Additionally, multiple experimental equipment like burn chambers, wind tunnels, and designated, open control fields and forests have been studied [13, 58, 76-82].

Spalding [102] and Williams [97] used scaling laws to study fires and realized that the total number of Pi-groups exceeded the number of degrees of freedom. Hence, the initial 28 Pi-numbers developed by Williams to scale fire phenomenon were extremely impractical. Therefore, the number of Pi-groups was reduced to 11 and finally to one or two, and proved ultimately to be sufficient for determining useful scaling relations [105]; one of these useful relations was the Froude number (Fr) which includes inertial and buoyant forces of importance in fires [105]. However, at this period of time in fire research, no specific, proven method was available to reliably reduce 28 Pi-numbers to just a few. Fortunately, Emori and Schuring [84] developed a relaxation theory to achieve this goal.

Emmons [103, 104] worked with pool fires and paper strips arrays, and Emori and Saito [50] investigated pool fires concluding that they were radiative-driven while crib fires were convective-driven. Then, cooperative work between Emori and Saito established useful and reliable methods for fire scaling [50, 101, 47] in which two separate methods for scaling of radiative-driven and convective-dominated fires were developed. Initially, 17 Pi-groups were identified for scaling convective-driven crib fires and 14 for pool fires [50].

2.3 Assumptions for the current study

This study is based on non-reactive flow experiments investigating flow instabilities caused by the interaction between buoyant and inertia forces. Elimination of chemical reactions, i.e. flames, significantly reduces the quantity of Pi-numbers required for scaling. However, a maximum possible similarity is required and used to validate the

experimental approach. Strong relations must be achieved between small–scale, non-reactive experiments, middle-scale fire experiments in a wind tunnel [59] and full-scale wildfires. The following assumptions were made for the present study.

First, it was assumed that air and gas flows within and around flames are turbulent, i.e. turbulent fire spread [47, 62, 106]. This means that inertial and buoyant forces dominate the viscous force [107]. This assumption was supported by critical assessments of previous studies which classified flow fields within crown [110, 111], grass [108], crib [50, 109] and wind tunnel fires [83, 98] as turbulent. Figure 2.2 shows turbulent fire spread in two different environmental conditions: a – wind tunnel experiments with cardboard fuels; and, b – grassland fires [90].

Figure 2.2 Turbulent flame zone in: a – wind tunnel burn, b – grassland wildfire [90].

Second, it was assumed that heat transfer from the flame to unburnt fuel is mainly due to convection. According to literature, the dominant heat transfer mode in large grass fires, crib fires and wind tunnel experiments is convection [50, 112, 113].

Third, it was assumed that fire propagates along a horizontal surface with horizontal wind in the direction of fire spread. Hence, fire spread in a single direction was considered. The horizontal airflow (wind) is assumed to be constant and controlled in two cases (wind tunnel burns and non-reactive flow experiments).

Fourth, it was assumed that the vertical (upward) component of the flow velocity is mainly due to buoyancy.

Fifth, it was assumed the fuelbeds were continuous and uniform, consisting of discrete fuel particles. Since one scale model did not include combustion, any fuel dependences in other two models were neglected. In other words, the same fuel

properties were assumed for wind tunnel experiments and wildland fires. Therefore, all Pi-numbers associated with fuel properties were automatically satisfied. However, heat fluxes were used in the models that represented heat from the flames.

2.4 Scaling of convective-driven fires

Recent studies on wildland fires [58, 59] have demonstrated that fire spread through wildland fuel beds is turbulent and governed by convective heat transfer from the fire front and hot combustion products. Therefore, the scaling laws for convective-driven fires were taken as the foundation for this study [47].

Previous studies by Finney et al. [58] established that the flame front of a progressing fire splits into towers separated by valleys, as depicted in Figure 2.2. The widths of the towers and valleys have been shown to remain nearly constant despite the fact that they are moving back and forth in span-wise direction along the flame front [83, 59, 90]. Figure 2.3 schematically shows behavior of a flame propagating to the right.

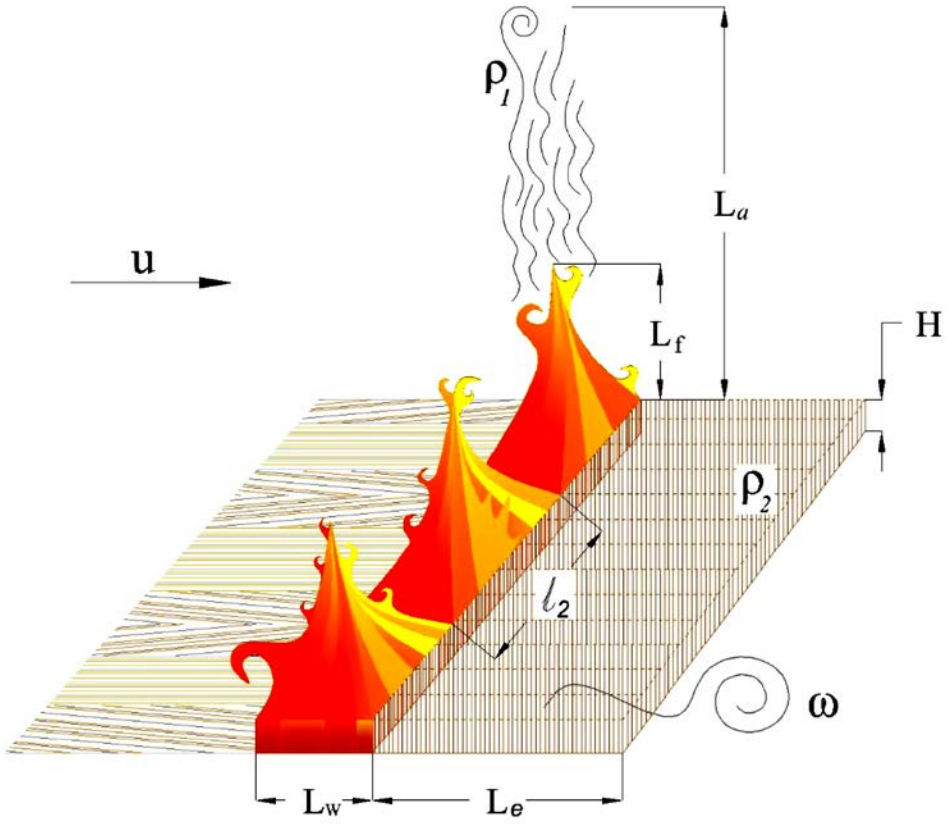

Figure 2.3 Schematic of flame spread over a fuelbed [90].

As shown in Figure 2.3, the parameters used in the scaling were:

- u – horizontal wind velocity;
- L_w – depth of the flame zone (where combustion takes place);
- L_f – average flame height;
- L_a – average plume height;
- ρ_1 – density of hot gases in the plumes;
- ρ_2 – density of unburnt fuel;
- H – height of the discrete fuel particles (fuelbed);
- L_e – preheating length (distance ahead the flame where unburnt fuel experiences significant heat transfer from the flame);
- ω – frequency factor (represents a time dependent behavior/instability such as vortex shedding);
- l_2 – distance between two valleys or width of a tower (it also represents wave length within a fire front).

All 17 Pi-numbers for convective-driven crib fires developed by Emori and Saito [50] are presented below. They were adapted for the type of fire depicted in Figure 2.3.

Table 2.1 Pi-numbers for convective-driven crib fires [50].

$\pi_1 = \frac{\Delta\rho_1}{\rho_1}$	$\frac{Density\ change\ of\ combustible\ gas\ and\ air}{Density\ of\ combustible\ gas\ and\ air}$
$\pi_3 = \frac{v}{u}$	$\frac{Vertical\ velocity\ component\ of\ gas\ flow}{Lateral\ velocity\ component\ of\ gas\ flow}$
$\pi_7 = \frac{\Theta_2}{\Theta_1}$	$\frac{Temperature\ of\ burning\ materials}{Temperature\ of\ combustible\ gas\ and\ air}$
$\pi_8 = \frac{\Delta\Theta_1}{\Theta_1}$	$\frac{Temperature\ change\ of\ combustible\ gas\ and\ air}{Temperature\ of\ combustible\ gas\ and\ air}$
$\pi_9 = \frac{\Delta\Theta_2}{\Theta_1}$	$\frac{Temperature\ change\ of\ burning\ materials}{Temperature\ of\ combustible\ gas\ and\ air}$
$\pi_{15} = \frac{\rho_1}{\rho_2}$	$\frac{Density\ of\ combustible\ gas\ and\ air}{Density\ of\ crib\ materials}$

Table 2.1 (continued)

$\pi_{16} = \frac{L_f}{l_c}$	$\frac{Flame\ height}{Length\ of\ stick}$
$\pi_{17} = \frac{H}{l_c}$	$\frac{Height\ of\ crib\ (fuelbed)}{Length\ of\ stick}$
$\pi_{18} = \frac{b_c}{l_c}$	$\frac{Thickness\ of\ sticks}{Length\ of\ stick}$
$\pi_{19} = \frac{b_0}{b_c}$	$\frac{Space\ between\ sticks}{Thickness\ of\ sticks}$
$\pi_{20} = \frac{q_f}{Q_\lambda}$	$\frac{Heat\ value\ per\ unit\ mass\ of\ crib\ material}{Latent\ heat\ per\ unit\ mass\ of\ crib\ material}$
$\pi_{21} = \frac{c_2}{c_1}$	$\frac{Specific\ heat\ of\ crib\ materials}{Specific\ heat\ of\ gas\ at\ atmospheric\ pressure}$
$\pi_{22} = \frac{l_c}{ut}$	$\frac{Length\ of\ stick}{Lateral\ velocity * time\ scale}$
$\pi_{23} = \frac{l_c g}{u^2}$	$\approx \frac{Buoyant\ force}{Inertial\ force}$
$\pi_{24} = \frac{Et}{\rho_2 l_c q_f}$	$\approx \frac{Heat\ radiated\ from\ burning}{Heat\ generated}$
$\pi_{25} = \frac{c_1 \Delta\Theta_1}{q_f}$	$\approx \frac{Heat\ stored\ in\ gas\ due\ to\ temperature\ rise}{Heat\ generated}$
$\pi_{26} = \frac{l_c g}{q_f J}$	$\approx \frac{Work\ done\ by\ buoyant\ force}{Heat\ generated}$

It was clear that satisfying all 17 Pi-numbers simultaneously would be impractical. Hence, the relaxation technique of Emori et al. [47] was used that simplified the above scaling requirements into the following seven physical parameters entailing two forces and five heats.

- $F_i = \rho_1 l_2 L_a u^2$ = inertial force of air and gas;
- $F_b = \Delta\rho_1 l_2 L_w L_a g$ = buoyant force of air and gas;

- $Q = Øq_f\rho_2 l_2 H L_w = IL_w t$ = heat generated;
- $Q_r = El_2 L_e t$ = radiant heat received by unburnt fuel;
- $Q_{c1} = c_p\rho_1 L_a l_2 L_e \Delta\Theta_1$ = heat stored in air and gas associated with temperature rise;
- $Q_{c2} = c_2\rho_2 l_2 H L_e \Delta\Theta_2$ = heat stored in unburnt fuel;
- $Q_\lambda = \lambda\rho_2 l_2 H L_e$ = latent heat of fuel.

Where [47]: *cp* – specific heat of gas at atmospheric pressure;

c_2 – specific heat of fuel;

E – irradiance received by radiometer;

g – gravitational acceleration;

H – fuelbed height;

I – fire intensity;

l_2 – width of fuelbed [47] - was replaced as flame tower width (Figure 2.3);

q_f – heat value per unit mass of fuel;

t – characteristic time;

$\Delta\Theta_1$ – temperature change of air and gas;

$\Delta\Theta_2$ – temperature change of fuel;

λ – latent heat per unit mass of fuel;

$Ø$ – ratio of consumed fuel to the total fuel available.

These seven physical parameters were used to form six independent Pi-numbers, as follows [47]:

$$\pi_1 = \frac{F_i}{F_b} = \frac{\rho_1 u^2}{\Delta\rho_1 L_w g} = Froude\ number$$

$$\pi_2 = \frac{Q_r}{Q} = \frac{El_2 L_e}{IL_w}$$

$$\pi_3 = \frac{Q_{c1}}{Q} = \frac{c_p\rho_1 l_2 L_a R\Delta\Theta_1}{IL_w}$$

$$\pi_4 = \frac{Q_{c2}}{Q} = \frac{L_e}{L_w}$$

$$\pi_5 = \frac{Q_\lambda}{Q} = \frac{\lambda L_e}{Øq_f L_w}$$

$$\pi_6 = \frac{F_i ut}{Q} = \frac{\rho_1 l_2 L_a u^3}{I L_w}$$

Where: $R = Le/t$ = horizontal fire spread velocity;

$I = Øq_f \rho_2 l_2 H/t$ = fire intensity.

Recent research by Finney's group has shown a strong correlation between Froude (Fr) and Strouhal (St) numbers. This correlation was established through research and observations of a variety of fuel types and burning conditions including full-scale crown fires, control burns over grassland, large-scale crib fires and wind tunnel burns of engineered cardboard [83]. The temperature of combustion gases can easily be above overcome 1000K regardless of burning conditions, indicating that fires generate strong buoyant forces which interact with the inertia force of air. In an upstream location of a fire, external wind and fire-induced flow are also present, both of which are governed by inertia [83]. The interaction between the buoyant and inertial forces causes flame instabilities with a repeating pattern which then lead to the formation of Gorlter vortices in the downstream direction [83]. Hence, it was concluded that, in the present investigation, the inertial force in the upstream direction ($F_{i,up}$) had to be considered separately from inertial force in the downstream direction ($F_{i,down}$). This distinction resulted in the following Pi-number [83, 47] which represents the relationship between the inertial force causing vortex shedding downstream of a flame and inertial force of air flow upstream of a flame [83]. It can be used to scale pulsing frequency of a fire front.

$$\pi_7 = \frac{F_{i,down}}{F_{i,up}} = \frac{L_e w}{u} = Strouhal\ number$$

Where: w – downstream pulsing frequency.

Because fire spread velocity is also important for appropriate scaling, another Pi-number was introduced, as defined in the following. With this addition, the total number of relevant Pi-numbers to be assessed for use in the current study was eight.

$$\pi_8 = \frac{R}{u} = \frac{Fire\ spread\ velocity}{Lateral\ velocity\ component\ of\ gas\ flow}$$

2.5 Scaling laws for the current study

The first step in the present work was to validate the wind tunnel fire scale model, using as a basis the already-developed scaling laws [83] that were adapted and modified for application to the experiments under study herein. For example, π_5 was ignored because its fuel dependence [83] was assumed to be the same in all models; therefore, it was automatically satisfied. Additionally, π_6 was neglected because the u^3 term would have caused very high wind velocity for the scale model and that would have changed the nature of the phenomenon under investigation.

Thus, the following Pi-numbers were used to perform scaling analysis.

$$\pi_1 = \frac{F_i}{F_b} = \frac{\rho_1 u^2}{\Delta\rho_1 L_w g} = Froude\ number$$

$$\pi_2 = \frac{Q_r}{Q} = \frac{E l_2 L_e}{I L_w}$$

$$\pi_3 = \frac{Q_{c1}}{Q} = \frac{c_p \rho_1 l_2 L_a R \Delta\Theta_1}{I L_w}$$

$$\pi_4 = \frac{Q_{c2}}{Q} = \frac{L_e}{L_w}$$

$$\pi_7 = \frac{F_{i,down}}{F_{i,up}} = \frac{L_e w}{u} = Strouhal\ number$$

$$\pi_8 = \frac{R}{u} = \frac{Fire\ spread\ velocity}{Lateral\ velocity\ component\ of\ gas\ flow}$$

Table 2.2 shows scaling predictions for the full-scale fire based on parameters of a wind tunnel burn. The original form of this table was interactive and could be used to predict parameters of the full-scale fire by entering parameters for the scale model. For example, parameters of the scale model entered on the left hand side of Table 2.2 predicted the parameters on the right hand side of the table; only the wind velocity for the real fire had to be assumed and, in general, is the only factor which can be easily measured even before a fire is initiated. It was concluded that most of the predicted parameters were reasonable, based on previous observation [75], except for the width of flame peak which had not been scaled; it will be dropped from further consideration in

this thesis with the recommendation that additional investigations of scaling laws for fires should include this parameter.

Table 2.2 Parameters and their relations used to correlate wind tunnel experiments to wildfire (primed symbols represent a real fire and unprimed symbols represent the scale model). The row labeled "width of flame peak" is bolded to indicate it was not scaled in this study and is to be dropped from further consideration herein.

Scaling Parameter	**Scale Model**		**Relation**	**Real Fire**	
Horizontal wind velocity	*u [m/s]*	1.00	u' must be assumed	*u' [m/s]*	10.00
Flame depth	L_w *[m]*	0.50	$L'_w = \left(\frac{u'}{u}\right)^2 * L_w \quad from\ \pi_1$	L_w' *[m]*	50.00
Preheating length	L_e *[m]*	0.10	$L'_e = \left(\frac{L_w{}'}{L_w}\right) * L_e \quad from\ \pi_4$	L_e' *[m]*	10.00
Flame burst frequency	*w [1/s]*	0.50	$w' = \left(\frac{L_e u'}{L_e{}' u}\right) * w \quad from\ \pi_7$	*w' [1/s]*	0.05
Velocity of flame spread	*R [m/s]*	0.10	$R' = \left(\frac{u'}{u}\right) * R \quad from\ \pi_8$	*R' [m/s]*	1.00
Width of flame peak	$\boldsymbol{l_2}$ **[m]**	**0.50**	$\boldsymbol{l'_2 = \left(\frac{L_e L_w{}'}{L_e{}' L_w}\right) * l_2 \quad from\ \pi_2}$	$\boldsymbol{l_2}$**' [m]**	**0.50**
Height of fire plume	L_a *[m]*	1.20	$L'_a = \left(\frac{L_e{}' V}{L_e V'}\right) * L_a \quad from\ \pi_3$	L_a' *[m]*	12.00

Table 2.3 is similar to Table 2.2 except that it shows relations for reverse scaling calculations. The geometrical similarity requirement demands flame depth (L_w) to be scaled in the same manner as the other lengths. However, this demand is not practical because L_w has to be significantly smaller than fuelbed length if the experimentation is realistic and has burnt fuel behind the flame zone and unburnt fuel ahead of the flame zone. All parameters were scaled based on the scaling laws and gave reasonable values confirmed by wind tunnel burns [59].

Table 2.3 Parameters and their relations used to correlate wildfire to wind tunnel experiments. Where prime represents a real fire while no prime stands for a scale model.

Scaling Parameter	Real Fire		Relation	Scale Model	
Horizontal wind velocity	u' [m/s]	8.00	$u = \left(\sqrt{\frac{L_w}{L_w'}}\right) * u' \ \ from\ \pi_1$	u [m/s]	1.79
Flame depth	L_w' [m]	10.00	$L_w \ \ must\ be\ assumed$	L_w [m]	0.50
Preheating length	L_e' [m]	6.00	$L_e = \left(\frac{L_w}{L_w'}\right) * L_e' \ \ from\ \pi_4$	L_e [m]	0.30
Flame burst frequency	w' [1/s]	0.05	$w = \left(\frac{L_e' u}{L_e u'}\right) * w' \ \ from\ \pi_7$	w [1/s]	0.22
Velocity of flame spread	R' [m/s]	0.60	$R = \left(\frac{u}{u'}\right) * R' \ \ from\ \pi_8$	R [m/s]	0.13
Height of fire plume	L_a' [m]	5.00	$L_a = \left(\frac{L_e V'}{L_e' V}\right) * L_a' \ \ from\ \pi_3$	L_a [m]	1.12

To correlate the non-reactive flow experiments to wind tunnel burns [59, 83] and wildfires, it is necessary that strong similarities in behavior are confirmed by the scaling laws, i.e. the scale models and prototype must satisfy the same set of Pi-numbers. However, because of the non-reactive nature of the experiments, some of the Pi-numbers described above can be eliminated from consideration. The reasons for eliminating these Pi-numbers are given in the following.

- π_2 was ignored because it involves irradiance received by a radiometer (E). When wind tunnel fire experiments are compared to wildfire this value is similar for both, i.e. E ≈ E'. However, in non-reactive flow experiments the irradiance is much smaller due to the use of a lower temperature, an absence of flame and the horizontal location of a heater which prevented radiative heat transfer downstream to where potential unburnt fuel would be located. Therefore, π_2 was considered not to be applicable and was ignored.
- π_4 was assumed to be automatically satisfied. It was not applicable for the non-reactive flow experiments because L_w represents heater width which was constant for any wind speed which would have affected preheating length (L_e).

- π_5 was ignored because it includes a fuel dependence (Ø) which was not applicable for the non-reactive, no-fuel, experiments.

In addition, in personal discussions with Saito [115] it was suggested that π_2, π_4, π_5, and π_6 could be ignored because they were either automatically satisfied or had minor influence on the outcomes. Therefore, the following Pi-numbers were selected as primary ones for the research conducted herein.

$$\pi_1 = \frac{F_{i,up}}{F_b} = \frac{\rho_1 u^2}{\Delta\rho_1 L_w g} = Froude\ number$$

$$\pi_3 = \frac{Q_{c1}}{Q} = \frac{c_p \rho_1 l_2 L_a R \Delta\Theta_1}{I L_w}$$

$$\pi_7 = \frac{F_{i,down}}{F_{i,up}} = \frac{L_e w}{u} = Strouhal\ number$$

These Pi-numbers were used to validate applicability of non-reactive flow experiments in fire research. The results are discussed in Chapter 4.

CHAPTER 3: INFRARED THERMOGRAPHY - VISUALIZATION OF CONVECTIVE-DRIVEN IGNITION OF WOOD PARTICLES

3.1 Experimental methods and results

Infrared (IR) thermography is a technique based on the detection of infrared radiation and its visualization through thermograms. Any object with temperature above absolute zero emits infrared radiation and the amount of this radiation increases with an object's temperature [117-119]. An IR camera detects warmer objects which stand out against a cooler background; different levels of IR emission correspond to different temperatures. Thus, an IR camera can be used to detect temperatures of objects, the accuracy of which depends on appropriate calibration of the camera and on the surface properties of the objects.

A surface behavior with regard to thermal radiation depends on its reflection, absorption and transmission. The sum of all three parameters' coefficients is equal to one for all surfaces; however, the value of each parameter depends on the surface. The following five examples are idealized types of behavior [120-122].

- An opaque body does not transmit any radiation that is incident upon it, but some of the radiation can be reflected from its surface and/or absorbed by it, i.e. transmission = 0 and reflection + absorption = 1.
- A transparent body transmits all radiation that is incident upon it, i.e. transmission = 1 and reflection = absorption = 0.
- A white body reflects all incident radiation uniformly in all directions, i.e. reflection = 1 and transmission = absorption = 0.
- A black body absorbs all radiation that is incident upon it regardless of frequency or angle of incidence, i.e. reflection = transmission = 0 while absorption = 1.
- A gray body has uniform reflection, absorption and transmission at all wavelengths.

The surface emissivity of an object characterizes its effectiveness in emitting energy as thermal radiation. Quantitatively, emissivity represents the ratio of the thermal radiation from a surface to the radiation from the "black" body's surface at the same temperature; hence, emissivity has values between 0 and 1. The surface of the "black"

body emits thermal (IR) radiation at the rate of 448 W/m^2 at a temperature of 25^{o}C [123]; any object with an emissivity less than one emits thermal radiation at a lower rate.

IR thermography has been used in fire research [116], but the accuracy of the temperatures that are measured is still under question because of the variation of the values of transmission, absorption and reflection during burning [120-122]. A large number of infrared detectors (IR cameras) are available commercially and an even larger number of lenses and filters can be purchased. Indeed, it is possible to calibrate an IR camera with respect to its use and image post-processing can be applied to enhance results.

IR cameras were recently introduced in wind tunnel fire experiments [90, 116]. Because wood is one of the main fuels consumed by wildfires, it is often used as the fuel particles in fire experiments [90, 116]. It was also used during the current research, one goal of which was to use IR thermography to accurately visualize the ignition of wood particles which were subjected to only convective heat transfer. Although accomplishing this goal may seem to be relatively easy, it is to be realized that the heating of wood changes its surface texture and color (gets darker), which leads to changes in surface emissivity. Hence, image post-processing was a step taken to improve accuracies of the temperature readings; one requirement for accurate post-processing is an understanding of the differences between actual emissivity of a surface and the emissivity of a “black” body to which the camera was calibrated.

The IR camera used during the experimentation was a FLIR SC4000 with resolution of 320 x 256 pixels and a spectral range of 3 - 5 μm. It was fitted with a broadband filter having a spectral range of 3.7 - 4.2 μm to eliminate flame emission and enable the solid, wood surface to be imaged [116]. A super-framing algorithm was employed to reduce the amount of noise and saturation, and to improve the quality of images; it recorded a set of four images (or sub-frames) at progressively shorter exposure times in rapid sequence and then repeated this cycle throughout each IR data acquisition trial. The sub-frames from each cycle were then merged into a single super-frame to combine the best features of all four sub-frames. This process, known as collapsing [116], provided thermal images with high contrast and accurate temperatures over a wide range.

A black ceramic plate with known surface emissivity of 0.96 was used as the "black" body to compare samples with, i.e. its transmission = 0, absorption = 0.96 and reflection = 0.04 (negligible). Wood craft sticks from Creativity Street were used as the wood particle samples. Because their texture and color varied, which could potentially affect their emissivity, ten sticks having different textures and colors were used during the experimentation. The sticks were cut into 50x17x1.5 mm pieces. As shown in Figure 3.1, after painting with a high temperature, flat black paint by Rust-Oleum, either one-half of the wood surface was black with the other half the wood's original color (left hand side of Figure 3.1) or 2 mm black stripes were painted that alternated with 2 mm of the original wood surface (right hand side of Figure 3).

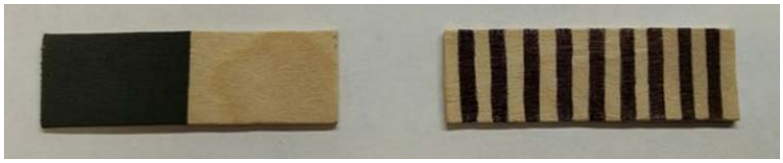

Figure 3.1 Wood particle samples.

The half painted surfaces were used to assess whether the black paint had reflection, absorption and transmission values close to that of the reference "black" body. They were placed next to the "black" body while a high-power light source irradiated the entire surface of the wood particles and the "black" body, simultaneously, at a 35^{o} angle of incidence from vertical; the IR camera was positioned to view the particles and the "black" body at the same angle from vertical – see Figure 3.2, left side. Infrared radiation from the light source that reflected from both the particles and "black" body was measured to determine temperatures while the surface temperatures were also measured using thermocouples attached to them. The difference between the IR radiance and the thermocouple temperatures of the "black" body versus those of the unpainted and painted wood surfaces would signify differences in reflectivities and, consequently, differences in absorption because the transmission values are zero for these surfaces. Ten data acquisition periods were accomplished with different wood samples but no significant differences in the IR data were detected between the black side of the particles and the "black" body. Hence, the black painted wood surface acted as a representative "black" body. Simultaneously it was discovered that the unpainted sides of the wood particles

gave slightly higher radiance readings than the painted surfaces; in other words, the unpainted wood had higher reflectivity and lower absorption than the painted wood surfaces.

The wood particles with painted black stripes were placed on an electrical heater (Figure 3.2, right side) and heated to their ignition temperature; the particles were firmly attached to the heater to sustain intimate contact between the heater and entire surface of the particles. The IR camera was used to record radiance and temperature as the particles were heated at 3 points on the black stripes and 3 points on the unpainted areas between the black stripes. These points were near each other to prevent any inaccuracy due to potential temperature gradients that were on the heater surface. Heater measurements were obtained from the black heating element surface near the wood particles. The temperature of the heater was also monitored using thermocouples.

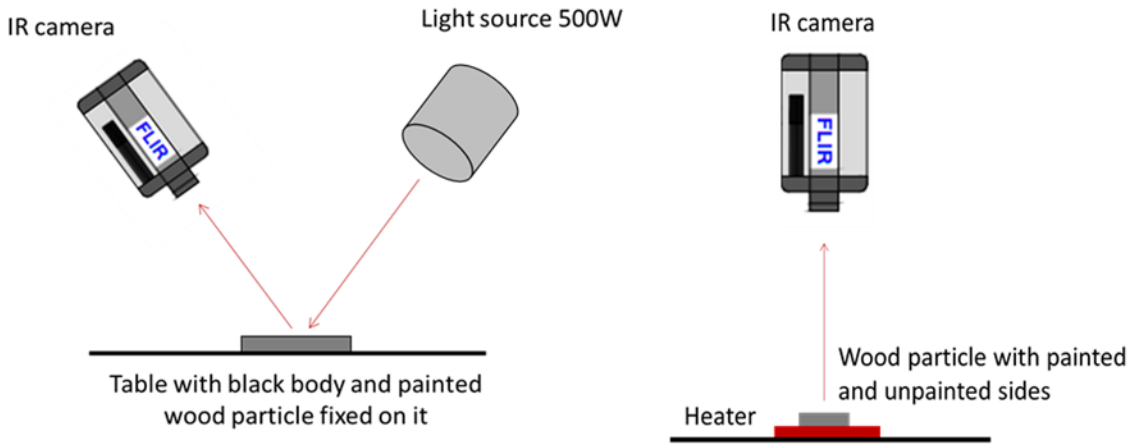

Figure 3.2 Experimental setup for IR imaging.

The graphs in Figures 3.3 and 3.4 summarize the data acquired during these tests. The IR camera measurements were acquired from black stripes, unpainted wood and from the heater surface, and are labeled accordingly in the Figures. Figure 3.3 displays radiance versus time of heating; as the heating time increased, the differences between the radiance of the black painted and unpainted wood particles increased. For example, at room temperature, i.e. time = 20 seconds, the radiances from black and unpainted areas were equal whereas at the end of the heating at 110 seconds the difference between these radiances attained their maximum value. While unpainted wood experienced pyrolysis

during these tests, it is also to be expected that charring of the black stripes could have caused paint decomposition which also would affect radiance measurements. However, as can be seen in Figure 3.4, differences in radiances of unpainted and painted black surfaces did not create significant temperature differences between these surfaces. In fact, between 25ºC and almost 500ºC, the differences between the temperature of black painted and unpainted areas were less than 5% for all wood particles tested.

Therefore, it was concluded that reflection from the black and unpainted areas on the wood caused the differences in both radiance and temperature whereas the emissivity was similar for them. Moreover, the temperature rise and the charring of the surfaces did not significantly affect surface emissivity. Thus, for this particular study, the IR camera could be used to measure wood surface temperatures without the need to consider emissivity adjustments.

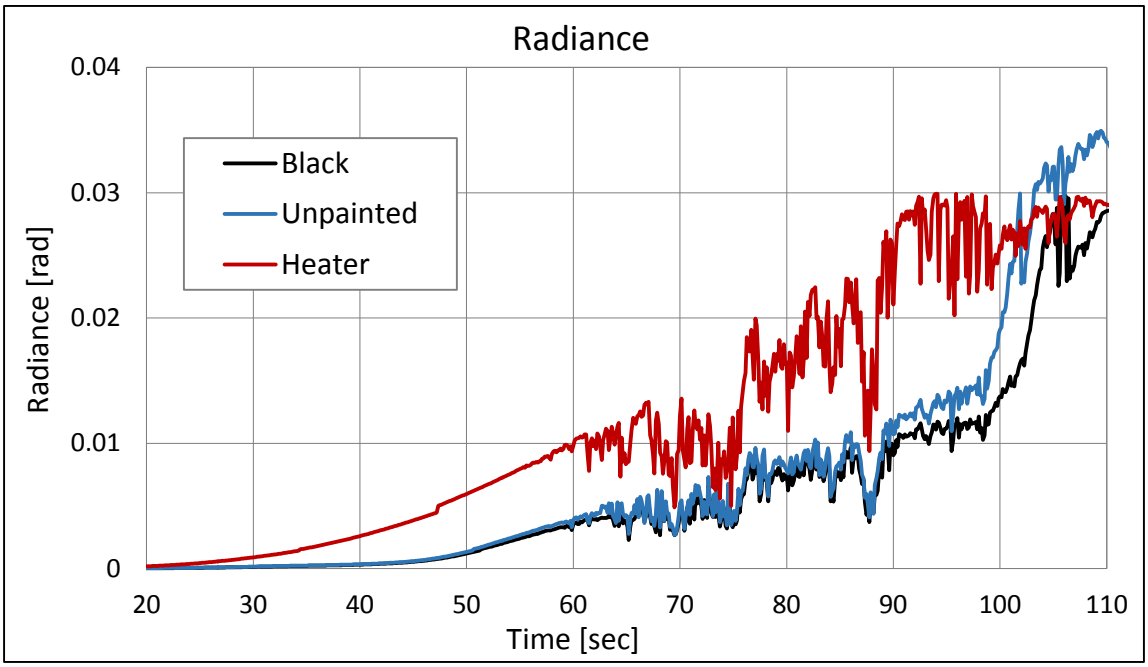

Figure 3.3 Radiance from black and unpainted wood surfaces, and heater surface (IR measurements).

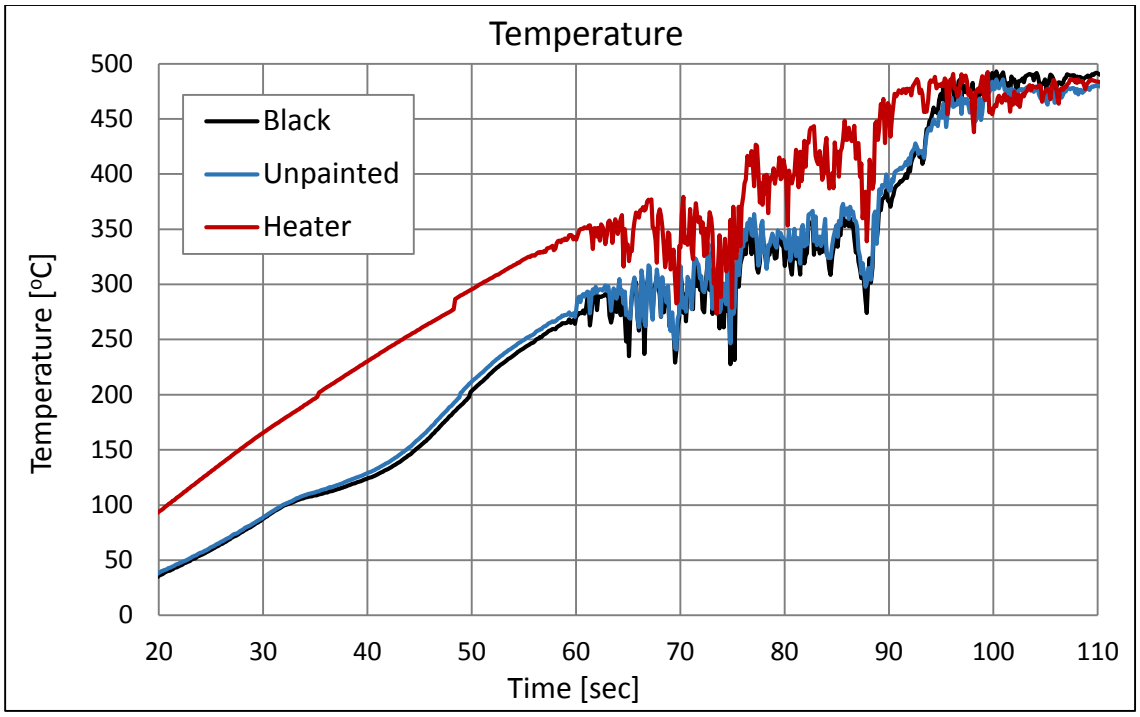

Figure 3.4 Temperature of black and unpainted wood surfaces, and heater surface (IR measurements).

3.2 Experimental setup and results for convective-driven ignition of fuel particles

Figures 3.5 and 3.6 show the experimental setup used for visualizing fuel particle ignition under convective-driven heating. An electrical heater (1.5 kW) coupled with a fan driven by a DC motor induced airflow over the particles with controlled temperatures and velocities. This airflow was directed by two wooden walls thermally insulated with cement boards. The fuel particles were placed downstream of the heating element, and were symmetrically positioned between the side walls. The entire setup was coated with high temperature, flat black paint sprayed from a Rust-Oleum container. The temperature of the hot airflow was controlled using a rheostat and measured using a thermocouple. Both the IR camera and thermocouples measured the temperatures of the wood particles as they were convectively heated on the side facing the hot airflow. Representative temperature histories during an experimental test are displayed in Figures 3.7 and 3.8.

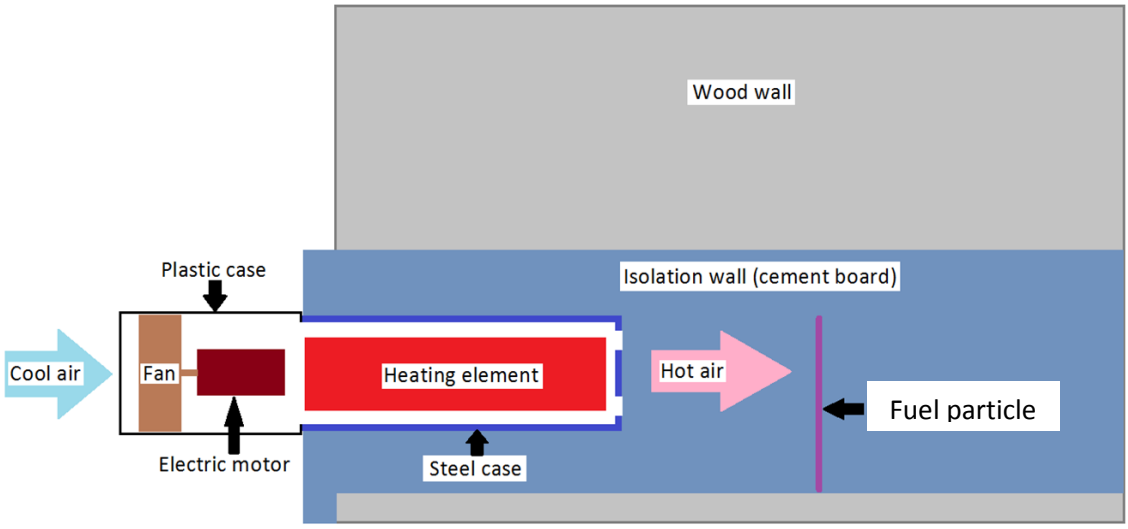

Figure 3.5 Diagram of the experimental setup for studying convective-driven ignition of wood and cardboard particles.

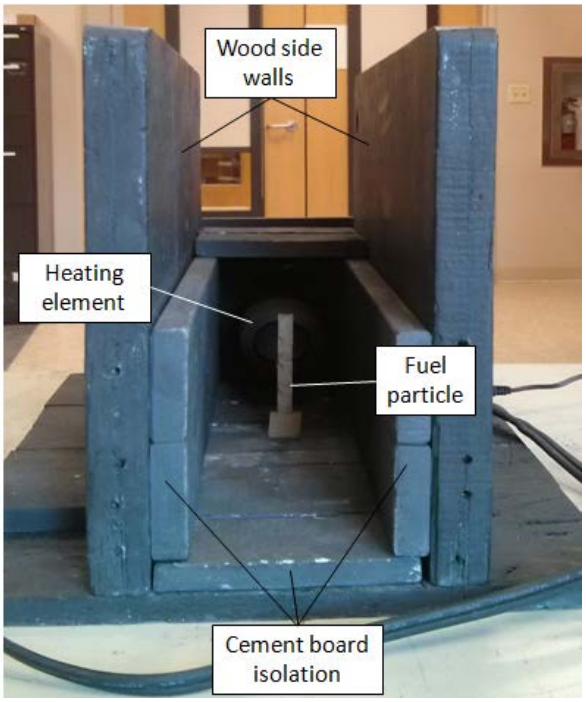

Figure 3.6 Experimental setup for studying the convective-driven ignition of wood and cardboard particles.

The following experimental materials and conditions were used:

- Cardboard particles with variable sizes and moisture content of 5.5 ± 0.5 % by weight. Although cardboard particles were also studied, the focus of this thesis will be the wood particles.
- Wood particles (50x17x1.5 mm) with moisture content of 5.2 ± 0.2 % by weight.
- Distance between the heating element and fuel particles was kept constant at 5 cm.
- Hot airflow velocities measured at the fuel particle location were 0.1, 0.3 and 0.8 m/s. These velocities were the result of 4.5, 6 and 9 volts applied to the DC driven fan, respectively. Voltages lower than 4.5 resulted in nearly zero air flow at the particles and hence were not used; voltages higher than 9 volts were not used because they caused a lowering in the air flow temperature as air velocities became higher than 0.8 m/s.

Figures 3.7 and 3.8 display temperatures of wood particles during their heating. In general, and as displayed in Figure 3.7, the thermocouple and IR results for temperatures were very similar. Hence, Figure 3.8 shows the temperature histories using the IR camera of wood particles heated under different air flows.

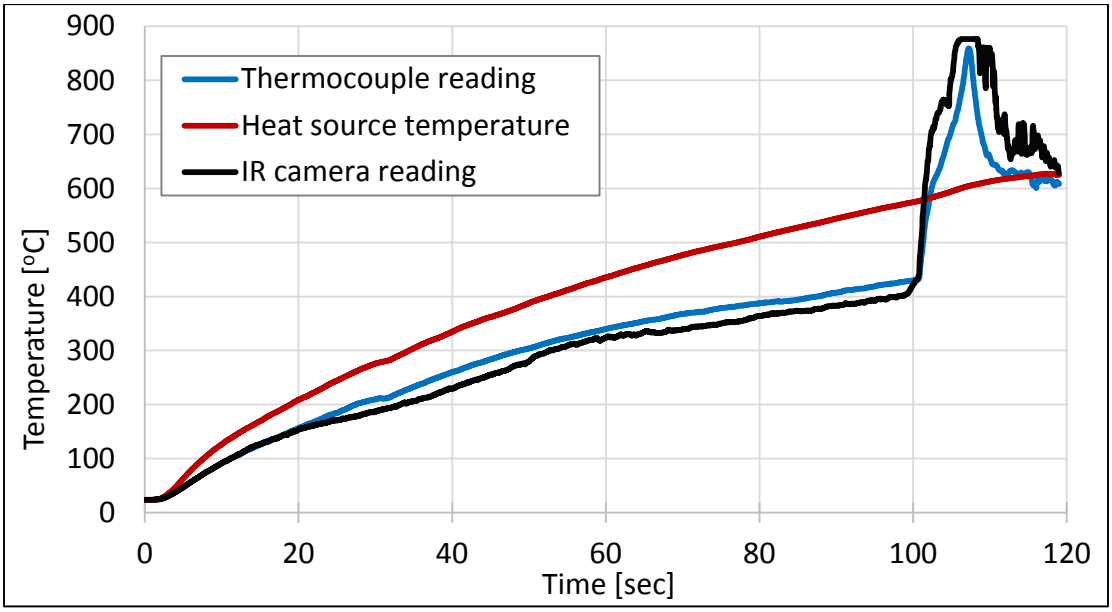

Figure 3.7 Temperature history of a wood particle heated and then ignited by purely convective heat flux, recorded by using an IR camera and thermocouples.

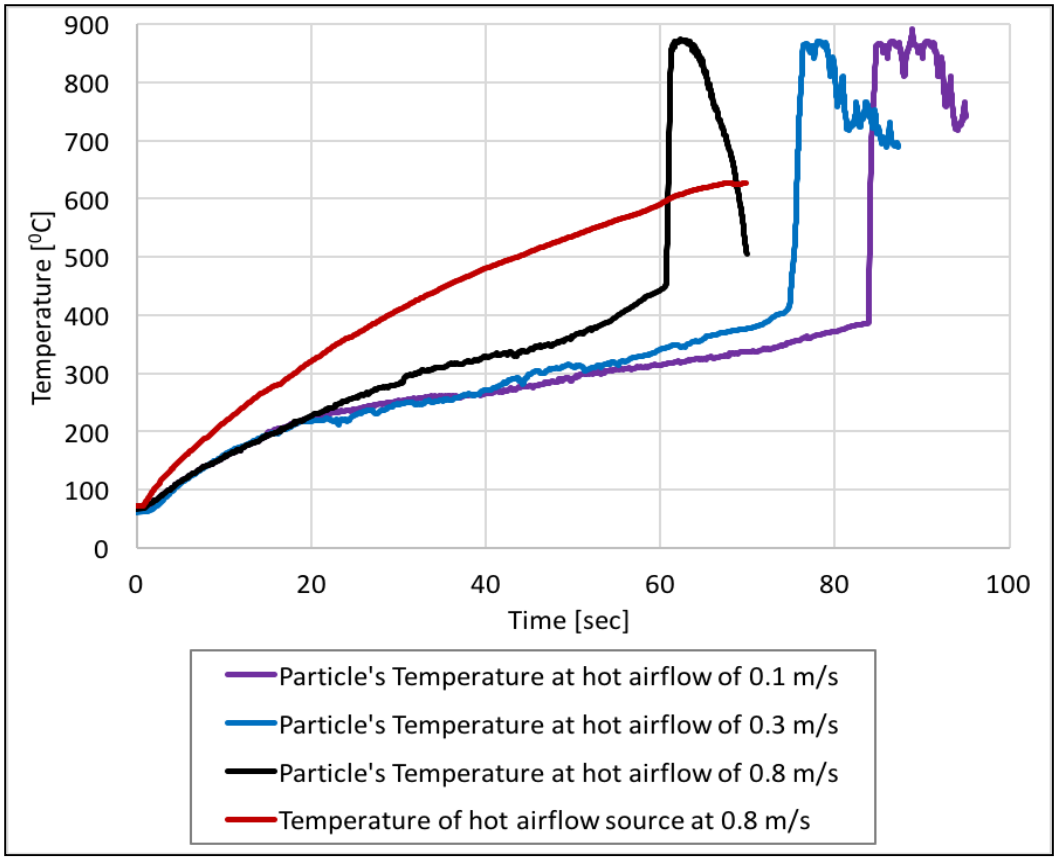

Figure 3.8 Temperature history of wood particles ignited by convective heat flux with different flow velocities, recorded by IR camera. The hot airflow source had similar temperatures for all three flow rates.

As expected, the highest flow velocity resulted in the fastest ignition of the particles when their temperature attained ~400°C. This result supports the following relations, assuming a constant hot airflow temperature.

$$\text{Convective heat flux} \quad q \sim \frac{1}{\delta_T}$$

$$\text{Thermal boundary layer} \quad \delta_T \sim \frac{D}{\sqrt{Pe}}$$

$$\text{Peclet number} \quad Pe = \frac{vD}{\alpha}$$

$$\text{Thus:} \quad q \sim \sqrt{v}$$

Where: D - dimension of the wood particles, v - airflow velocity and α - thermal diffusivity of air.

The data in Figure 3.8 show higher airflow flow velocities caused the wood particles to ignite faster and then burn for a shorter time duration. Flames were first observed to be attached onto the side edges of each particle and then, at airflow velocities of 0.1 and 0.3 m/s, covered the entire surface of the particles that faced the heater. In contrast, at an airflow velocity of 0.8 m/s, flames were not observed on the front side of the particles facing the heater; rather, they were attached onto the back side of the particles, seemed unstable and were less bright in comparison to the lower airflow velocities.

For the 0.8 m/s flow rate, it was surmised that concentration of pyrolysis gases along the front side of the samples was low and stable chemical reactions (flame) could not be established. Pyrolysis gases were transported by the hot airflow to the back side of the particle, where a local stagnation point appeared due to flow separation, and flame was established. Further rise of airflow velocity after ignition resulted in flame detaching from the particle's surface and even it's extinguishing before the samples were completely burned. This behavior is in agreement with heat transfer assessments in which, during preheating, the airflow temperature was hotter than particle's surface and heat was transferred from the air to the particles. In contrast, after ignition, the heat transfer direction was reversed. Therefore, at higher flow velocity with thinner boundary layer, particles firstly experienced higher convective heating and then, after ignition, higher convective cooling which would destabilize or even extinguish the flame. It was thereby concluded that thickness of the boundary layer around the fuel particles played a crucial role in the ignition and combustion of the fuel particles.

At the two lower flow velocities, the flames were stable and bright, and covered the entire surface of the fuel particles. This situation would stimulate high radiative heat fluxes from the particles. Therefore, when considering both convective and radiative heat fluxes from an ignited fuel to an unburnt one, an optimal flow velocity exists which stimulates the highest combined heat transfer. Also, the effective distance for heat transfer via convective or radiative mechanisms could be a function of the horizontal flow rate or wind velocity.

CHAPTER 4: FLOW VISUALIZATION

4.1 Experimental methods and setup for visualization of non-reactive flows

Flow visualization studies were conducted using a specially constructed low-speed wind tunnel with the experimental, visualization section having a transparent acrylic panel through which images were acquired (Figure 4.1). A digital camera, a Canon EOS 5D Mark II, with Canon EF 50 mm f/1.8 lens was used to acquire images. An electrical heater (1.5 kW) coupled with temperature feedback controller were used to generate buoyant-driven upward airflow. To produce white smoke, a paper towel strip soaked uniformly with petroleum jelly (Vaseline) was placed on the heater and, as it became hotter than ~200^{o}C, uniform, thick white smoke was produced.

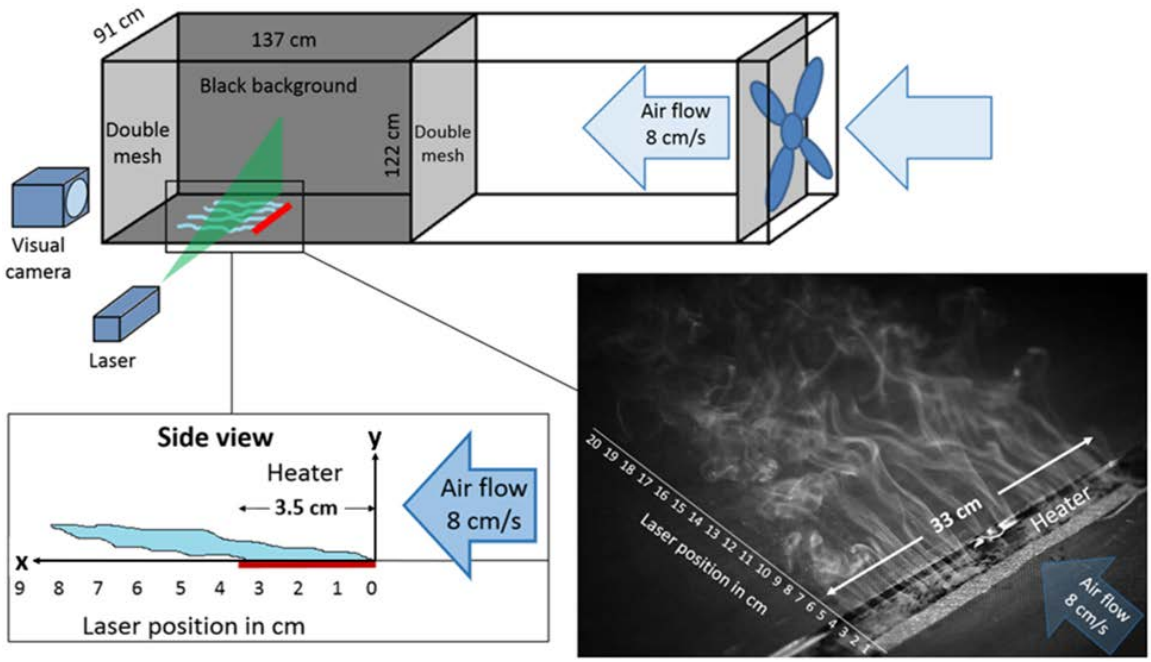

Figure 4.1 Flow visualization experimental setup consisting of a low-speed wind tunnel, heater, a digital camera, and a 300-mW diode pumped, solid state laser with a cylindrical lens and a LED light. Also shown is an image of smoke flowing through the visualization section, illuminated using the LED.

Horizontal airflow was induced in the laboratory wind tunnel using an AC fan. To ensure the uniform air flow throughout the cross section of the wind tunnel, two double mesh sheets with 2x2 mm holes were placed between the fan and the test section, and one double mesh sheet was placed downstream of this section. Both the back and bottom

sides (the base) of the test section were painted low luster (flat) black to reduce light reflection and increase the contrast between the white smoke and the background. More than 300,000 digital images were acquired during the tests while using this set-up.

The heater had an effective surface area of 3.5 cm by 33 cm and was mounted perpendicular to horizontal airflow, flush with the base of the test section; Figure 4.2 gives an infrared (IR) image of the heater element. The top surface of the wind tunnel was open to air, and the other three sides were formed by cement board, used as an insulator, mounted onto wood. The temperature controller provided precisely-controlled temperatures of the air output from the heater. Because the heater's dimensions were much smaller than the size of the wind tunnel test section, the heater was placed symmetrically in the middle, resulting in little-to-no side wall effects on the air flow.

After a paper strip soaked with Vaseline was placed on the heater's top side, the heater controller, which used a thermocouple for continuous temperature monitoring, was set to a temperature of interest and then the heater was turned ON. Once the heater's top surface achieved desired temperature, images were acquired using the camera.

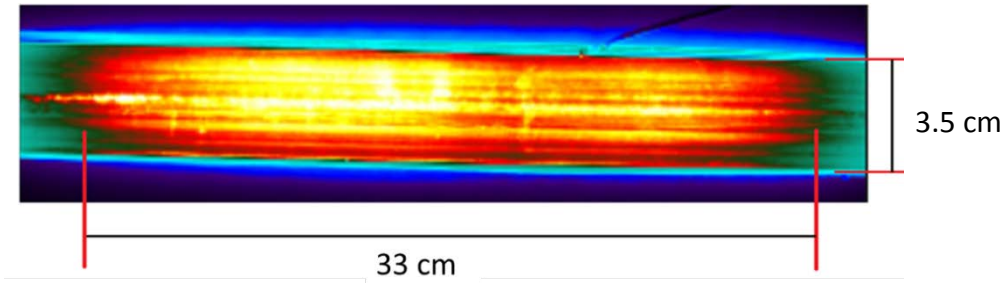

Figure 4.2 Infrared image (top view) of the electrical heater at temperature of 260ºC.

Besides illumination using the laser sheet, the smoke streaks were also illuminated using a LED compact light placed inside the test section and mounted on its top side at different locations depending on angle of image acquisition. The LED did not affect the air flow through the test section. This illumination allowed 3D visualization of smoke streaks from different angles, the results of which are presented in the following sections. Interpretations of the complicated 3D flow patterns imaged with LED illumination were assisted by use of the laser sheet illumination which effectively enabled flow visualization in 2D, the locations of which were moved along horizontal positions

perpendicular to the flow and the images of which were sequentially examined relative to the 3D images.

The diode pumped, solid state laser produced a wavelength of 532 nm (green) and output power of 300 mW. It was coupled with a cylindrical lens the produced a 2D laser sheet with vertical orientation (z direction) and directed parallel to the heater and perpendicular to the flow (x-y direction); the width of the laser beam after exiting the lens was 2 mm and it had an opening angle of 30^{o} The position of the laser, placed in front of the test chamber as shown in Figure 4.1, was changed in increments of one centimeter from the front (upstream) edge of the heater to 30 cm downstream from that point. The camera was mounted downstream of the test section and captured images of the flow approaching the camera. The camera and the laser were moved simultaneously to maintain a constant distance between them.

A series of preliminary tests showed that 200^{o}C was the minimal temperature of the heater's surface which gave smoke streaks thick enough for visualization. However, as temperature increased above 200^{o}C the time of smoke generation was reduced dramatically; as discussed in Section 4.2, several experiments were performed at temperature between 200-500^{o}C with no horizontal flow. At 200^{o}C, stable smoke generation continued for approximately 20 minutes while at 300^{o}C the duration of smoke generation dropped to about 3 minutes; ignition of the Vaseline soaked paper occurred when temperatures were greater than 400^{o}C. Because establishing appropriate camera focus settings took up to a few minutes and was the main difficulty at the beginning of each test for imaging the approaching smoke flow, it was decided to use a constant temperature of 200^{o}C for all visualization tests involving external horizontal flow. However, several temperatures were used during the visualization of upward motion when no horizontal flow was imposed (see Section 4.2).

The horizontal air flow generated by the fan had three controlled velocity regimes of 8, 11 and 15 cm/s (±15%). These three velocities were chosen during preliminary experimentation in which it was found that the 8 cm/s flow speed was the lowest possible for the setup while velocities above 15 cm/s were too high and caused erratic flow behavior. These flow velocities were measured inside the test section at heights of 1.5 -

30 cm above the base. Smoke streaks were also tracked through the test section when the heater was OFF to ensure uniformity and steadiness.

At a temperature of 200°C, the convective heat flux from the heater surface was estimated based upon a boundary layer thickness of 2.0 ± 0.3 kW/m^2, depending on the flow speed. Parameters used for scaling calculation included: L_w, which represents fire zone depth (Figure 2.3) and was taken as the heater width perpendicular to the horizontal air flow = 3.5 cm; L_f, the flame height; and L_e, the preheating length. The values of L_f and L_e were measured using an IR camera, and both represent a region with temperatures significantly above ambient.

4.2 Visualization of buoyant induced upward flow

The first step in investigating flow behavior was visualization of buoyant driven, upward flow. During these tests, the mesh sheets described for the experimental set-up in Figure 4.1 were replaced by acrylic sheets to establish an enclosed, transparent box with no horizontal flow entering or leaving it. The images of smoke flow during these tests, displayed in Figures 4.3 - 4.5, show in detail the upward flow structure from smoke arising from the heated Vaseline soaked paper on the heater at different temperatures.

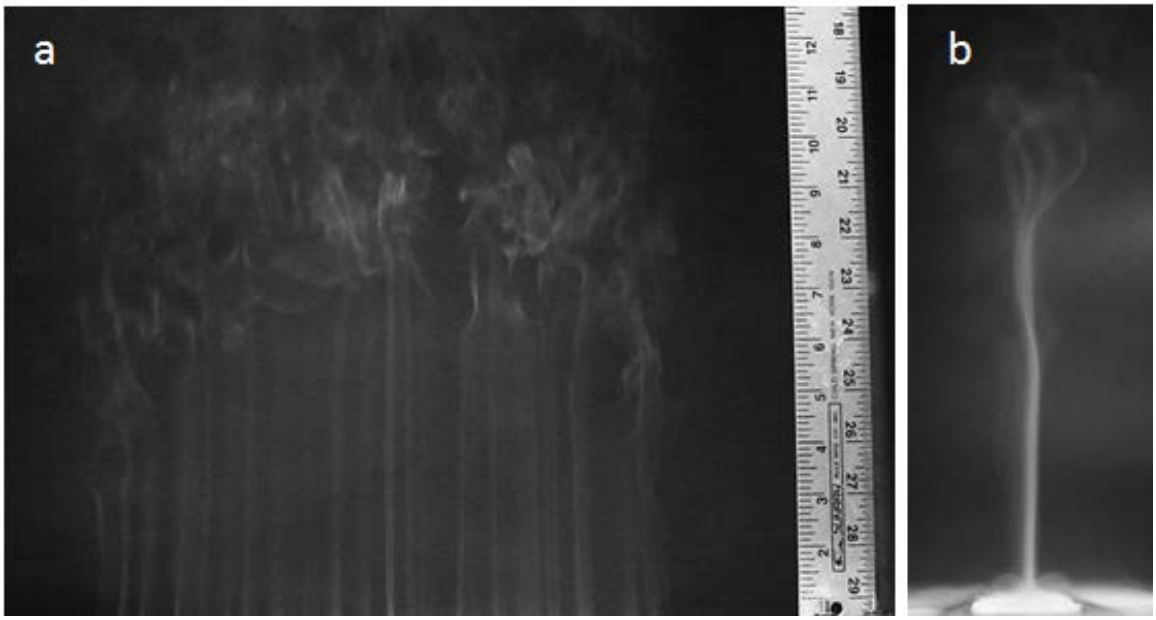

Figure 4.3 Smoke streaks arising from the heated surface at a temperature of 200°C under no horizontal flow: a – front view, and b – side view.

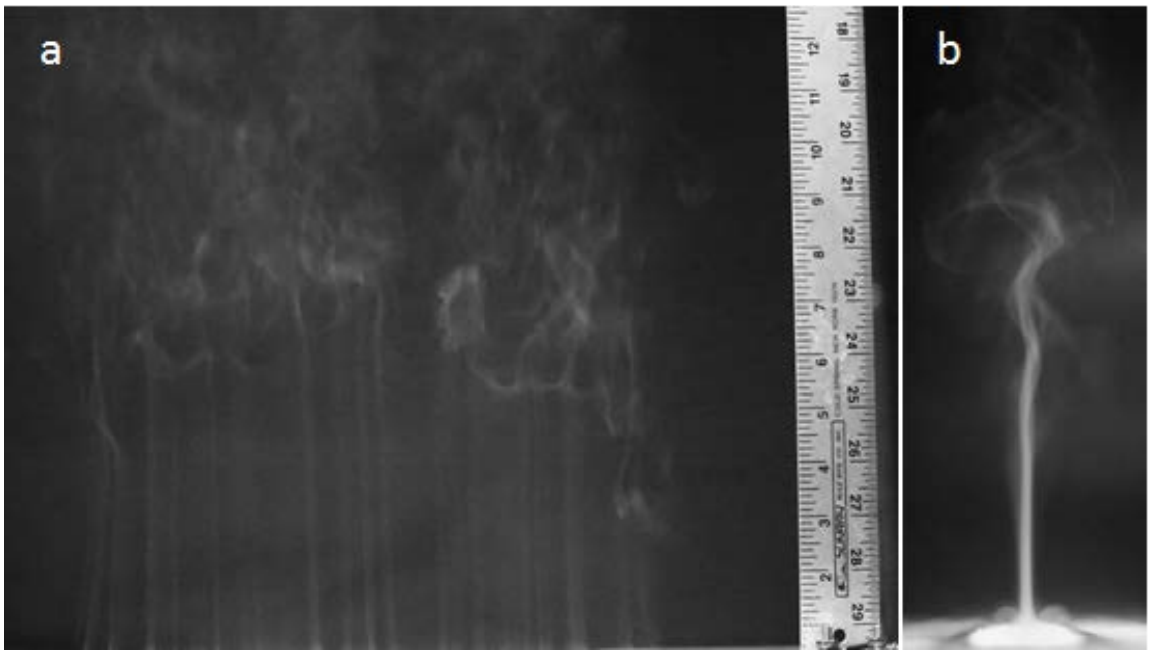

Figure 4.4 Smoke streaks arising from the heated surface at a temperature of 250^{o}C under no horizontal flow: a – front view, and b – side view.

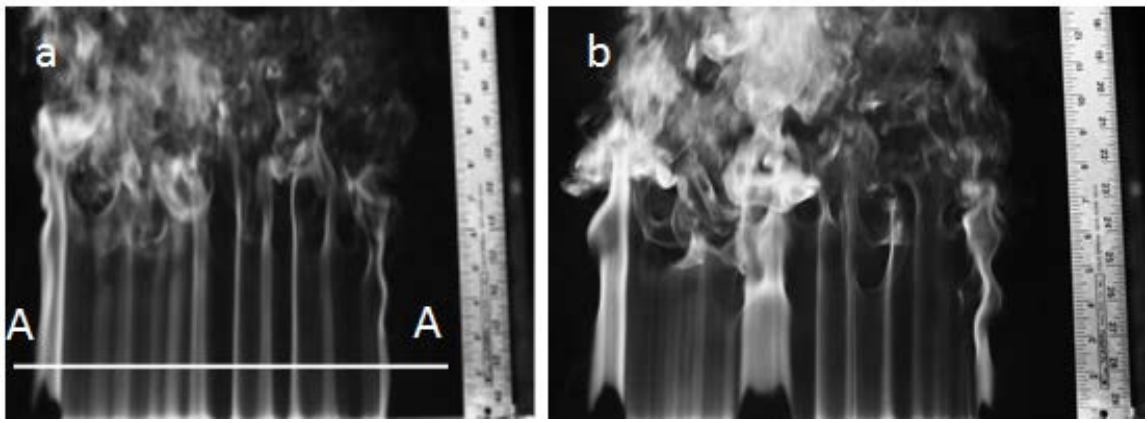

Figure 4.5 Smoke streaks arising from the heated surface under no horizontal flow at a temperature of 400^{o}C (a) and 500^{o}C (b). Cross section A-A is schematically shown at the Figure 4.8.

Generally, the buoyant-induced flow patterns were similar regardless of the temperature of the heater. In all cases, the rising smoke formed discrete vertical columns organized along the length of heater surface, and the locations of these columns remained constant during each test. Additionally, as seen in the side view images of Figures 4.3 and 4.4, the smoke columns emanated from the middle and along the length of the heater. They consisted of laminar upward flow, which after a certain distance of travel evolved

into turbulent flow. As the temperature of the heater was increased, the number of columns (Figure 4.6) decreased and their diameters increased. Also, the data in Figure 4.6 show that the average distance at which turbulent flow was established above the heater became smaller as the heater temperatures were increased; the error bars in Figure 4.6 represent minimum and maximum measured values. Fluctuations in the upward laminar flow increased with increasing temperature, example of which is presented in Figure 4.7. The same trend was observed in the variations in the number of columns: at higher temperature, the variation in the number of columns became larger. This behavior could be explained by ignition and the appearance of flames at temperatures above 400^{o}C that introduced additional heat flux and uncontrolled temperatures at the Vaseline soaked paper.

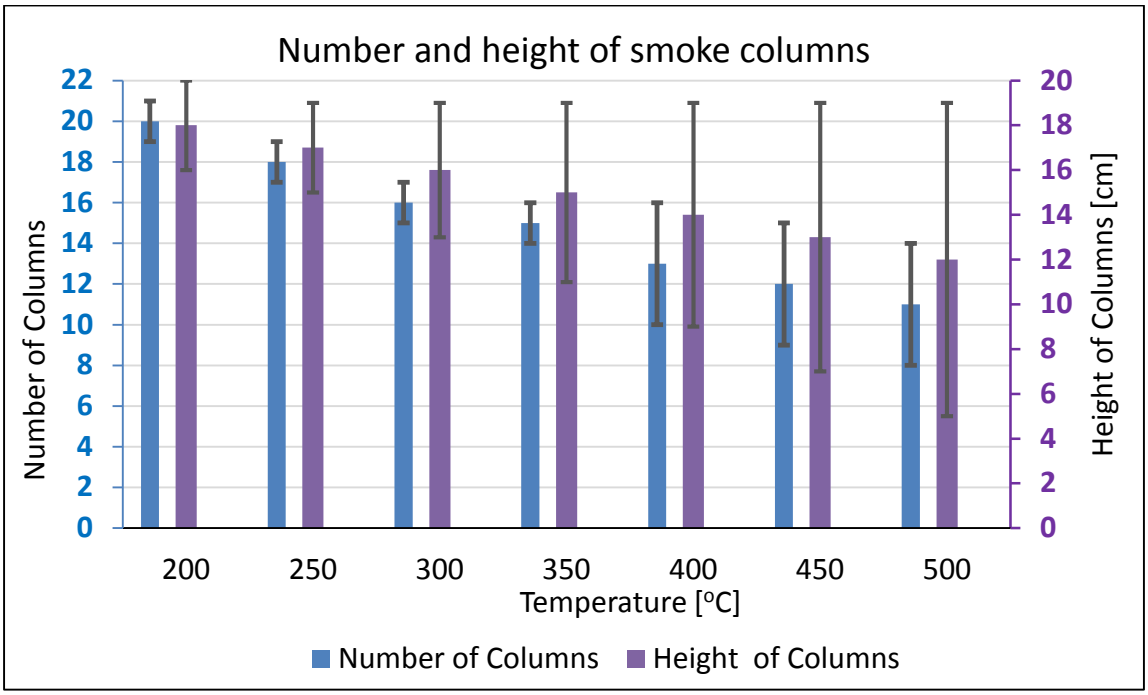

Figure 4.6 Number and height of smoke columns depending on temperature.

These results were confirmed in several repeated experiments and the formation of the buoyant-driven smoke columns was considered as a natural phenomenon. An analogy was drawn between this behavior and that of actual flames with no horizontal flow in which the flames split into towers separated by valleys. Assuming that the heater represented a fire zone, the smoke from it would represent the flow field above a flame.

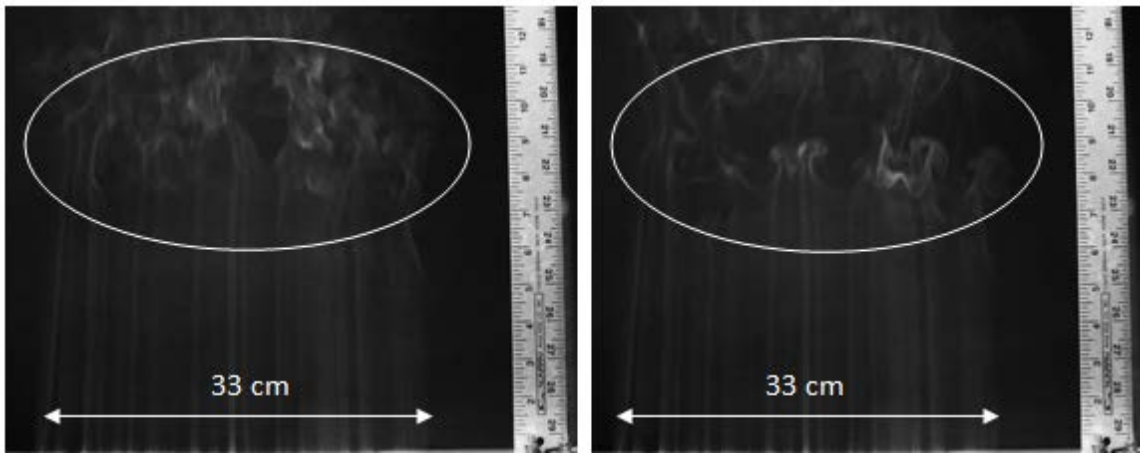

Figure 4.7 Fluctuations of the laminar upward flow at 200^{o}C.

The smoke columns formed along the entire surface of the Vaseline soaked paper on the heater (Figure 4.3-4.7) were schematically shown at the Figure 4.8. With increasing temperature, higher smoke generation rates and even ignition occurred, the smoke columns became wider and their average quantity per unit length fewer. Higher temperature resulted in larger vertical flow velocity which stimulated instability and transition to the turbulent regime.

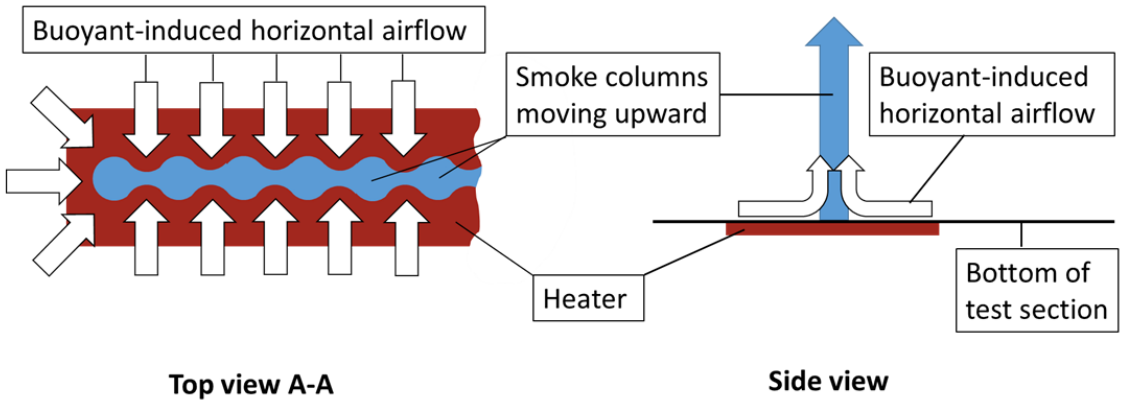

Figure 4.8 Schematic diagram of buoyant-induced flow.

4.3 Visualization of the interaction between horizontal and buoyant-driven upward flows

4.3.1 Illumination using LED light

The second step in the visualization work was to capture images of the dynamic interaction between buoyant-induced upward flow and horizontal airflow. Smoke from the Vaseline soaked paper on the heater was blown horizontally into the test section and illuminated with the LED light. Images of the flow are presented in Figure 4.9, showing horizontal and slightly upward flow. Visualization was accomplished from four main views: Figure 4.9a is a top view, Figure 4.9b is a frontal view looking into the approaching flow, and 4.9c and 4.9d are side views at locations downstream and upstream of the heater. The smoke formed discrete streaks moving downstream at a small upward relative to the horizontal.

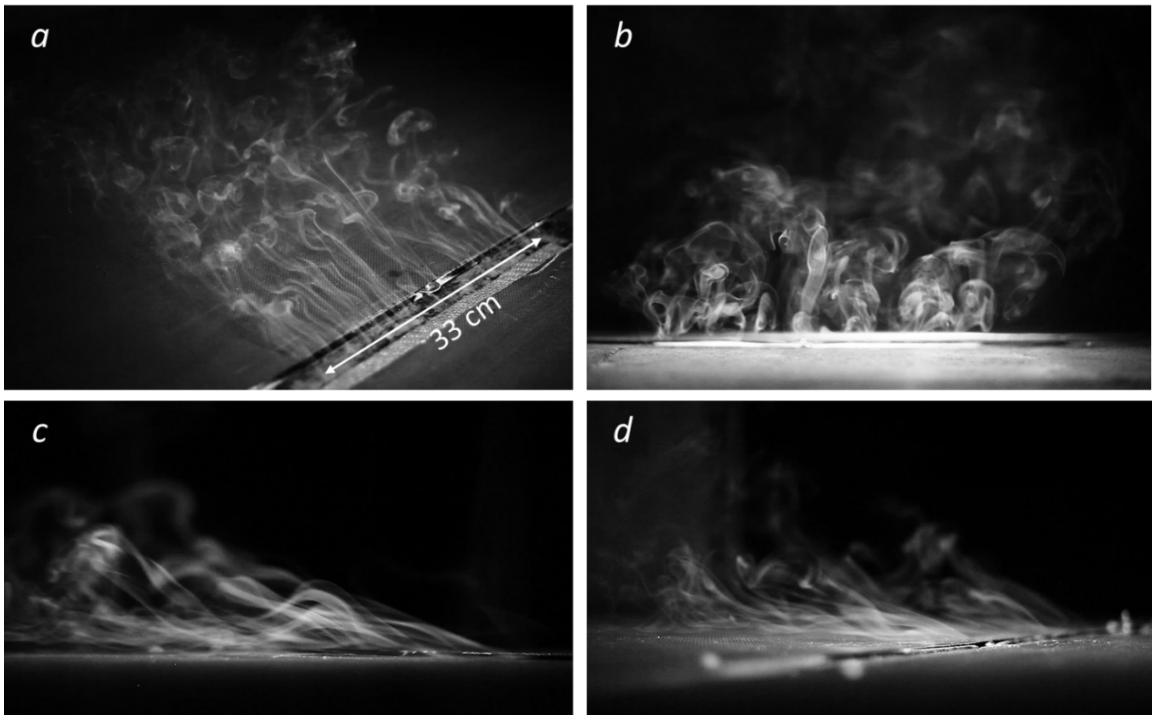

Figure 4.9 Flow visualization using LED light at 200^{o}C; a – top view, b – front view of approaching flow, c – side view downstream of the heater and d – side view upstream of the heater.

It was concluded, after carefully examining the images, that the structures of the individual smoke streaks were vortex tubes. They are discussed in a following.

The entire heater's surface was covered by 3.5 cm width paper strip soaked with Vaseline during initial experiments. From these, the side view images in Figure 4.9c and 4.9d show the vortex tubes occasionally formed multiple-level structures where tubes that originated close to the upstream edge of the heater were generally higher above the base than tubes formed closer to tail edge of the heater. This observation initiated investigations into whether it would be possible to use thinner paper strips that would produce more well-organized and single-level smoke flow structures consisting of discrete vortex tubes of the same height. Hence, studies were conducted in which 1 cm width paper strips were placed at three different locations on the heater; images acquired while producing smoke from these positions are presented in Figure 4.10, and labeled as upstream, middle and downstream. No differences in the flow structure could be detected for these three locations, and the flow patterns stayed approximately constant independent of whether the strips were 3.5 cm wide or 1 cm wide at any location on the heater. The only difference was in the amount of smoke - wider stripe gave more smoke. It was impossible to constantly sustain a single-level and stable smoke flow pattern because the flow remained unchanged even if the smoke was not visually seen along the entire heater's surface. In other words, even if vortex tubes were initiated ahead or behind the 1 cm paper strips but could not be observed, the flow structures downstream indicated they still existed and affected the flow, and interactions between the vortex tubes resulted in identical visualization results for all three locations and widths of the Vaseline soaked strips.

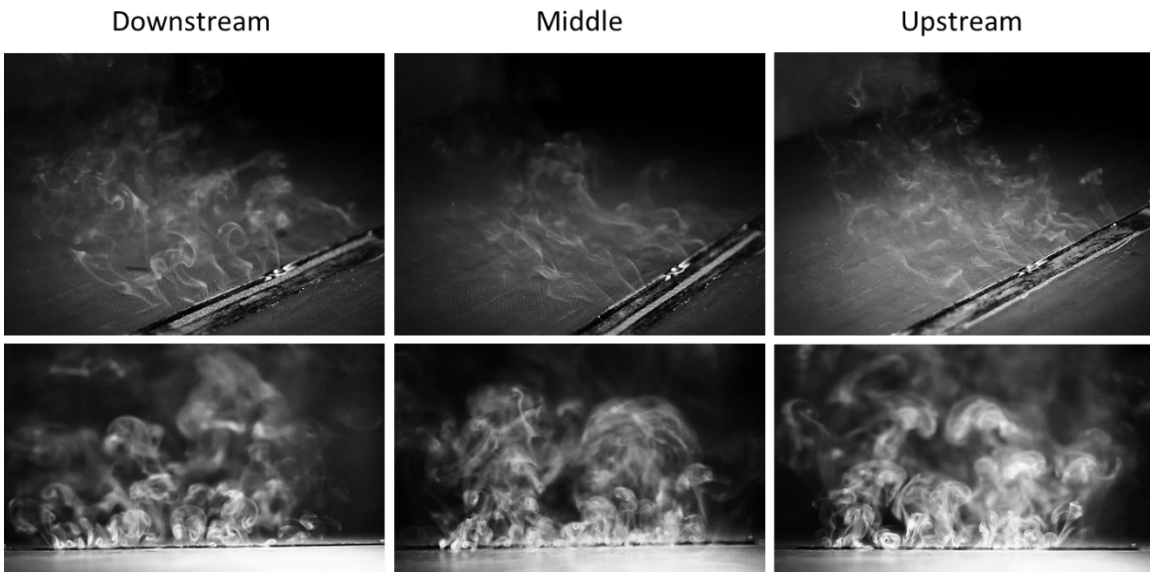

Figure 4.10 Visualization of smoke generated by 1 cm paper strips at three different locations along the heater (flow velocity = 8 cm/s).

The effects of varying the horizontal air velocity were studied while the heater temperature was maintained at 200ºC. Figure 4.11 shows that the flow behavior was similar for the three velocities, 8, 11 and 15 cm/s, tested. Smoke formed vortex tubes at the heater surface, continued to flow downstream, and then interacted with each other with an eventual transition into turbulent flow. The main differences were in the length of the vortices, in the direction, x, of the horizontal flow and height above the base, y, of the test section at various locations along the x direction. Increased horizontal airflow velocities resulted in longer vortices at lower heights. As can be seen from top views of Figure 4.11, at an airflow velocity of 15 cm/s the flow of discrete vortices was well-organized and remained intact for greater distances than did at 8 and 11 cm/s. This behavior may be related to decreased interactions between the vortices at the higher velocity.

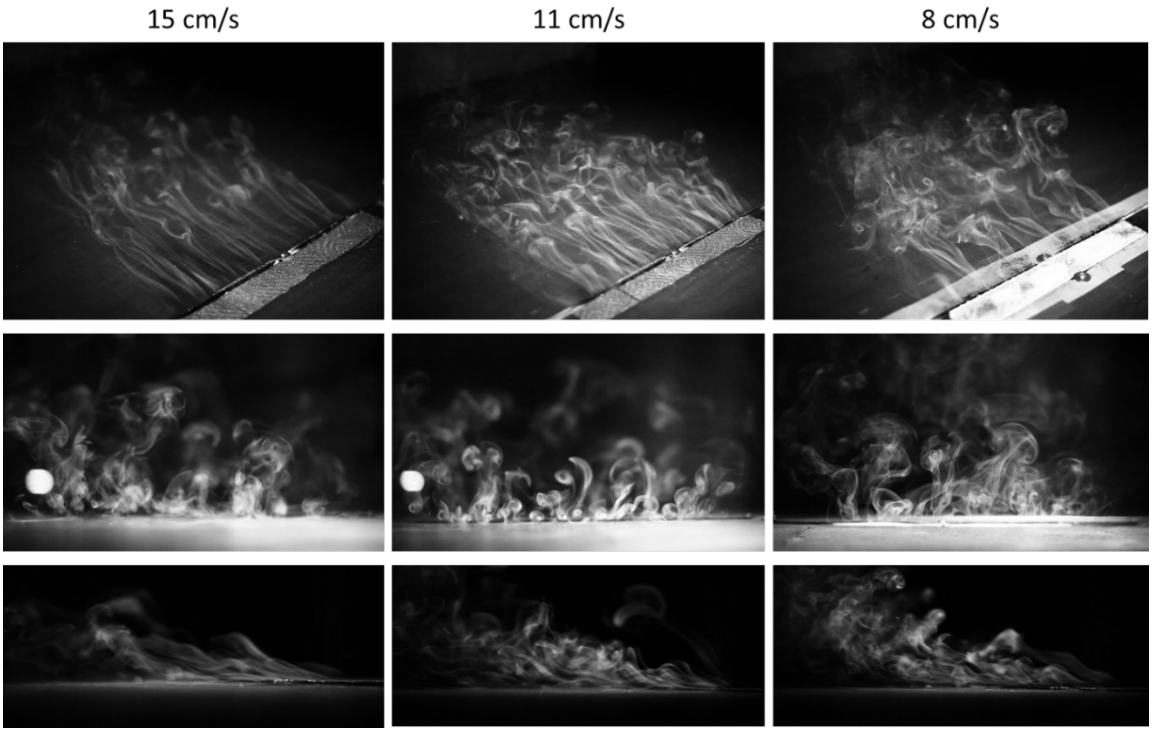

Figure 4.11 Visualization of smoke streaks' behavior at three airflow velocities.

Figure 4.12 gives the range of, and averaged values for, the lengths and heights of the vortices. The smoke flow height and its variance decreased with increased horizontal velocity; as was predicted because of higher horizontal air velocities, smoke streaks moved at a smaller angle with respect to the horizontal as the air velocities were increased.

At an air velocity of 8 cm/s, the well-organized vortex region had a length up to 14 cm, and at larger lengths the flow transitioned to turbulent. The flow height and its variance increased with distance x, i.e. in the direction of air flow. Dramatic increases in flow height were noted when the x distance was between 0 - 5 cm (where vortices were formed), and between 14 - 18 cm (transition to turbulent flow) while flow was almost horizontal between the x distances of 5 - 14 cm.

An air flow velocity of 11 cm/s shifted the turbulent transition region to a distance x between 16 - 20 cm; it produced well-organized vortex flow for an average distance up to 16 cm.

The even higher air flow velocity of 15 cm/s resulted in formation of vortices with average length of around 19 cm and the turbulent transition region was between 19 and 25 cm.

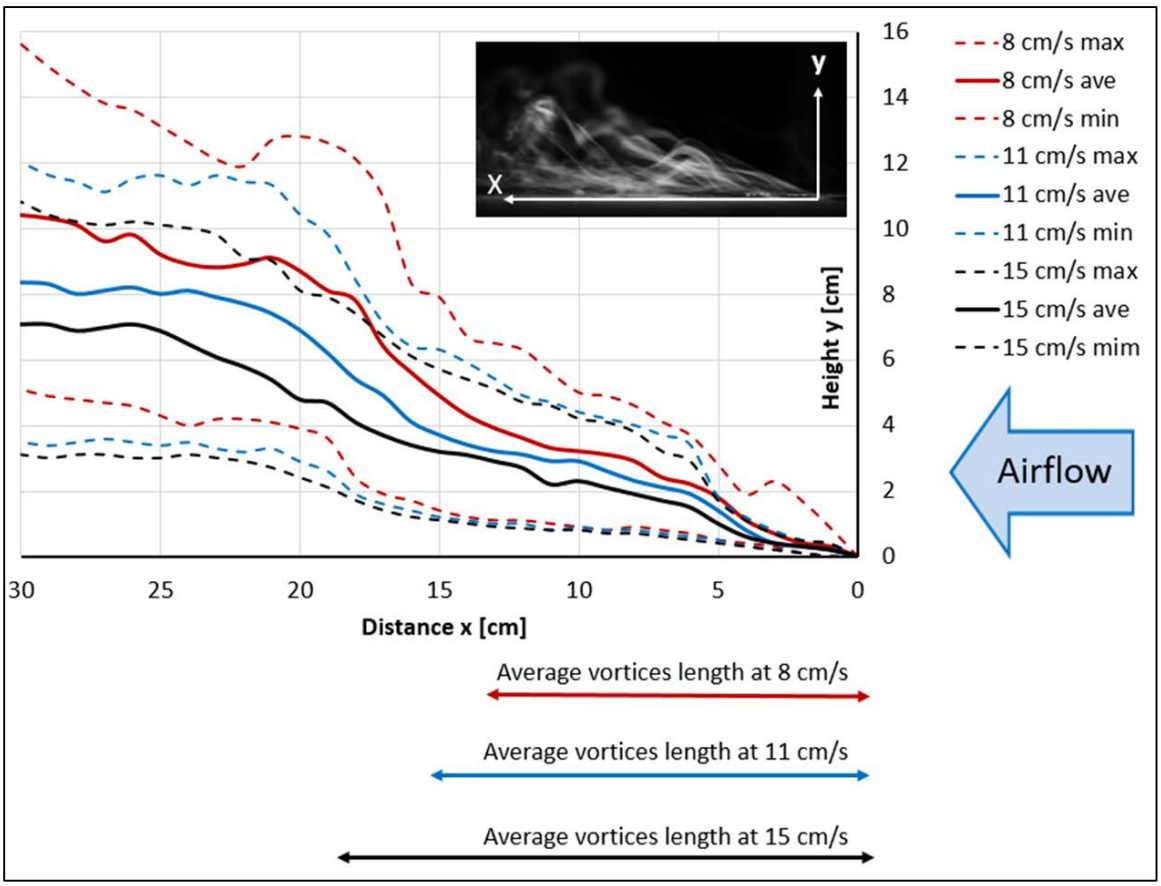

Figure 4.12 Smoke flow height as a function of distance x and horizontal airflow velocity.

Figure 4.13 presents some height variations when using an air velocity of 8 cm/s; it can be seen that the images on the left side of the figure (both front and side views) demonstrated flow which was much closer to the base of the test section, i.e. smaller y distance, than the images on the right side of the figure.

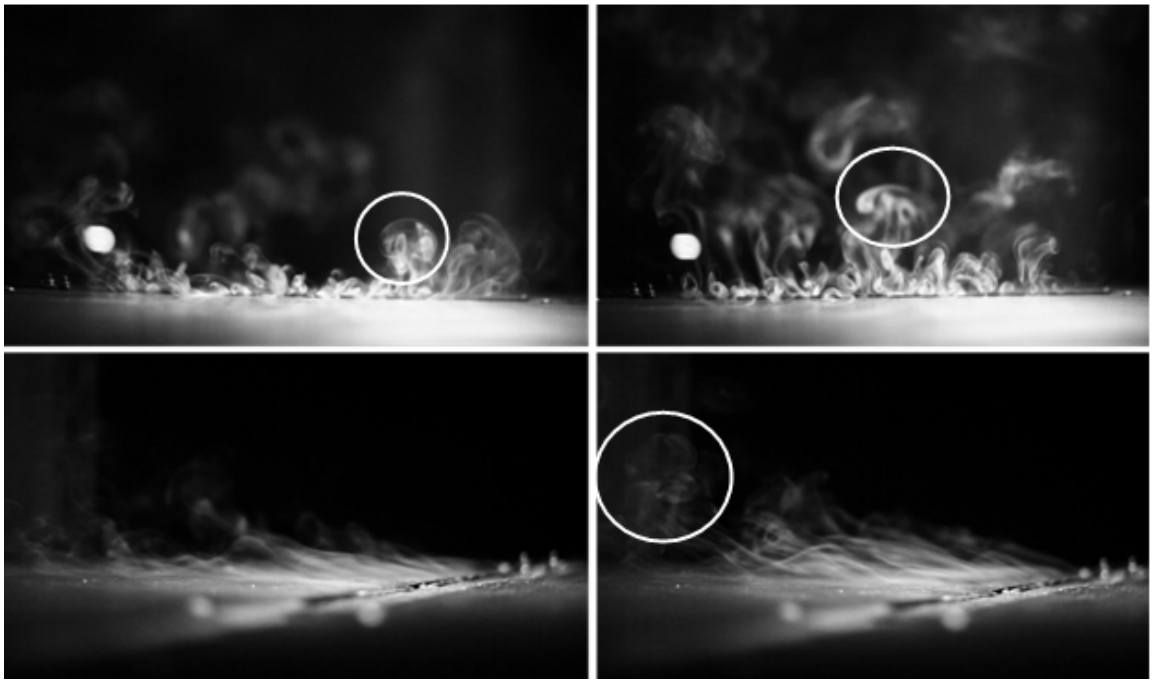

Figure 4.13 Variations in flow height at an air velocity of 8 cm/s.

In addition to vortex tubes, Figures 4.13, 4.14 and 4.15 show other often observed flow features (in the circled areas). The “mushroom shape” upward motion circled on the Figures 4.13 and 4.14 were often observed at a horizontal distance x close to and within the turbulent transition region, however, it also occasionally appeared at smaller x distances. This type of motion was the main contributor to the variations in smoke flow height and is represented by the upper dotted lines in Figure 4.12.

Variations in the length of vortex tubes were usually a consequence of upward motion of the “mushroom shape”; they destabilized and then broke the vortex tubes. After the formation of the “mushroom shapes”, vortices could re-establish, as shown at the Figure 4.14d. “Mushroom shape” motions never were present simultaneously along the entire length of the heater; rather, they normally were observed at random locations and, thus, some vortex tubes became longer than others (Figure 4.14c).

Rotational motion of the bulk flow was also observed in the transition between laminar-to-turbulent flow and in the turbulent regime. This rotational motion formed smoke peaks and valleys as shown at the figure 4.14a. Sometimes, when this motion

appeared closer to the heater, i.e. at smaller distance x, individual vortex tubes were involved, as demonstrated in Figure 4.15.

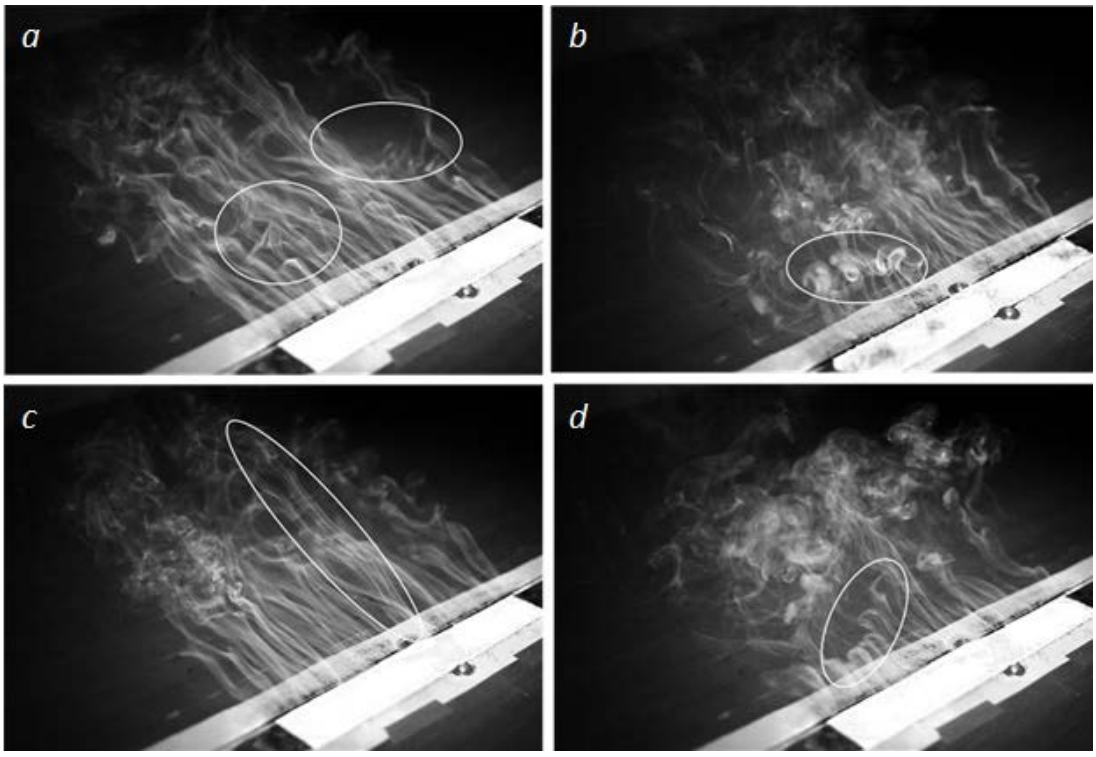

Figure 4.14 Flow features of interest (circled): a – bulk rotational motion; b – upward "mushroom shape" motion; c – vortex tubes; and d – variation in vortex tubes length.

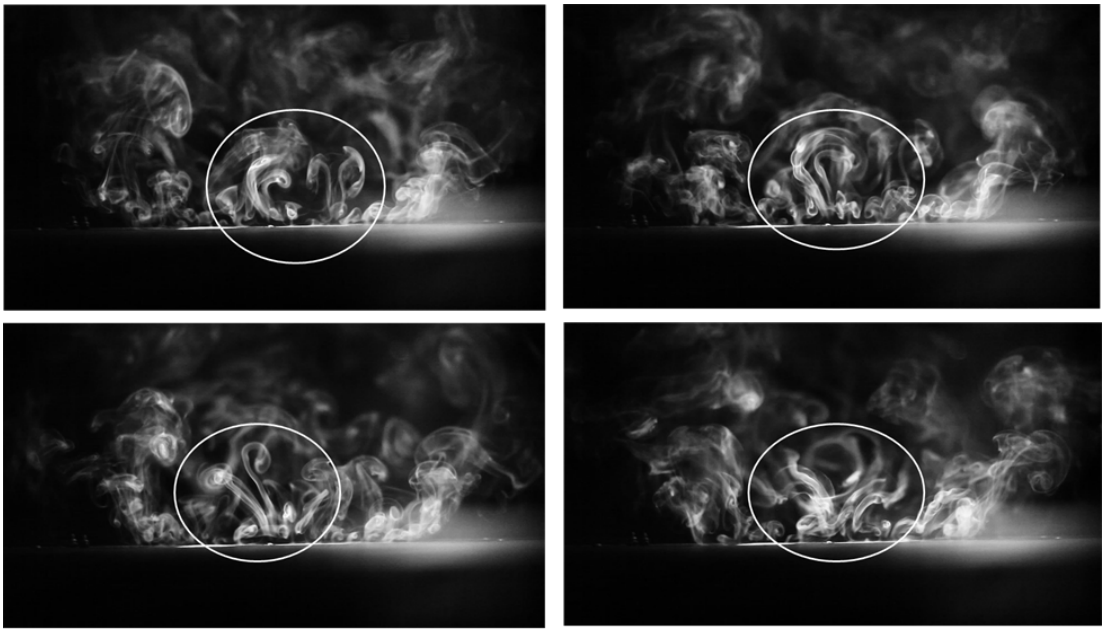

Figure 4.15 Interaction between vortex tubes and bulk rotational motion.

The main difficulty during imaging was to focus the camera on dynamic flow features. Smoke was always present between the camera and focus plane which hid some flow patterns; smoke behind the focus plane also complicated the acquisition of clear images. Hence, 2D illumination of the smoke using a laser with a cylindrical lens was used to provide greater detail of flow characteristics. This approach transformed the 3D imaging approach into sequences of 2D snapshots at different locations.

4.3.2 Illumination using a green laser

Considering that the flow behavior was similar for the three velocities studied, the 2D laser sheet illumination and data collection were accomplished using only an airflow velocity of 8 cm/s. Flow characteristics were recorded using 28 slices within a range of $3 \leq x \leq 3\,0$ cm from the leading edge of the heater. The frontal view of assessing the approaching flow was of main interest, some image of which are shown at the Figure 4.16. More images can be found in the Appendix A.

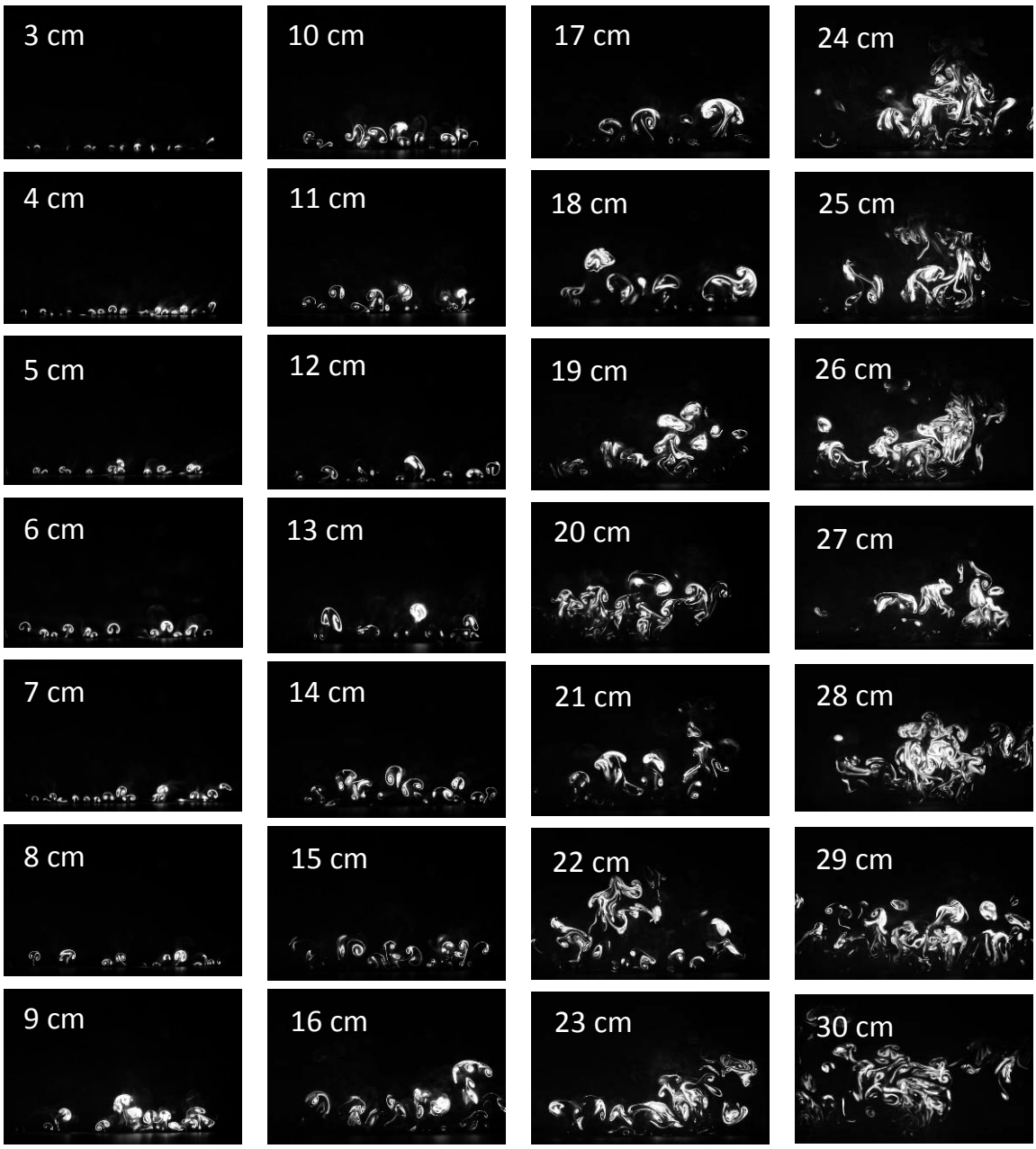

Figure 4.16 A collection of images taken at all 28 laser sheet locations with flow velocity of 8 cm/s.

Recorded images confirmed that, at a distance x of up to 14 cm, the smoke appeared as vortex tubes; additionally, they clearly showed these tubes were always in pairs. The vortex pairs consisted of two vortex tubes with opposite directions of rotation, as shown at the figure 4.17.

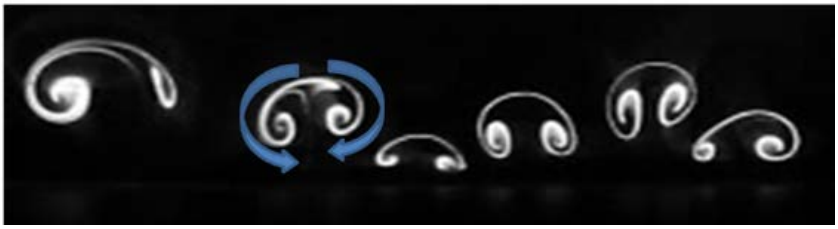

Figure 4.17 Vortex pairs at x = 8 cm.

Four different flow regimes were identified: Regime (1) included the formation of vortex tube pairs; Regime (2) was where vortex tubes began to actively interact; Regime (3) was a transition region from an organized flow of vortex pairs to convective-driven chaotic motion; and Regime (4) included convective-driven chaotic flow. These regimes are identified in Figure 4.18.

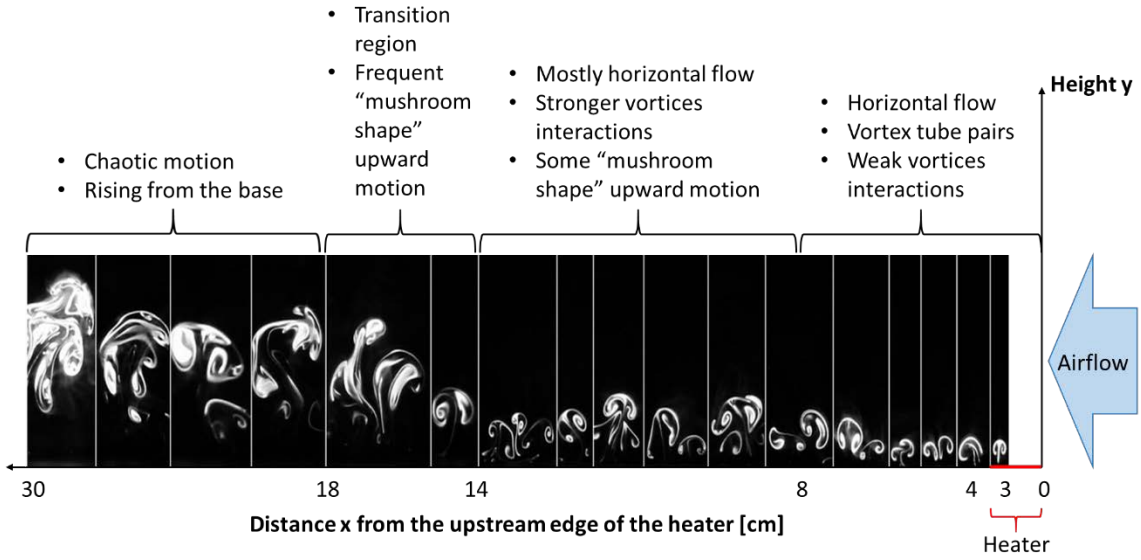

Figure 4.18 Flow structures along the horizontal distance x from the upstream edge of the heater identified from laser sheet illumination and visual images taken at seventeen different locations.

Regime (1) was identified within the location $3 \leq x \leq 8$ cm. In it, the well-organized flow structures consisted of several vortex tube pairs, with some tubes interacting with each other and all moving almost horizontally along the base of the test section. Regime (2) was observed at $9 \leq x \leq 14$ cm and was 5.5 - 10.5 cm from the trailing edge of the heater. In this regime, the average diameter of vortex tubes increased which caused greater interactions between adjacent tubes plus the generation of

“mushroom shape” upwardly moving flow structures; in this regime the flow direction was mostly along the base of the test section. Regime (3) was located $15 \leq x \leq 18$ or 11.5 - 14.5 cm from the trailing edge of the heater; this regime was characterized by a transition from organized vortex flow structures to chaotic flow, included frequent “mushroom shape” and bulk rotational motions. Regime (4) was identified to be between $19 \leq x \leq 30$ cm, i.e. 15.5 - 26.5 cm from the trailing edge of the heater. This regime included turbulent flow that was separated from the base. Additional images of the flow structure can be found in Appendix B.

Distances from the leading edge of the heater with a range of $3 \leq x \leq 14$ cm was of particular interest because the flow was horizontal along the base of the test section and could potentially be associated with preheating length in a real fire. In particular, vortex pairs plus their interactions were examined intensely. Figure 4.19 gives some examples in this region of organized flow that consisted of individual vortex pairs imaged between $3 \leq x \leq 12$ cm; it can be clearly seen that the average diameter of vortex tubes increased with the distance x, which then could stimulate more frequent interactions between vortices at larger distances. At distances between $10 \leq x \leq 12$ cm, the vortex tubes “pushed” on each other and consequently experienced deformation. The vortex interactions at $10 \leq x \leq 14$ cm led to formation of flow structures where some vortex pairs were above others, which increased the smoke flow height. Figure 4.20 displays some examples of vortex pairs’ interactions at different x locations. Some additional images can be found in Appendix C.

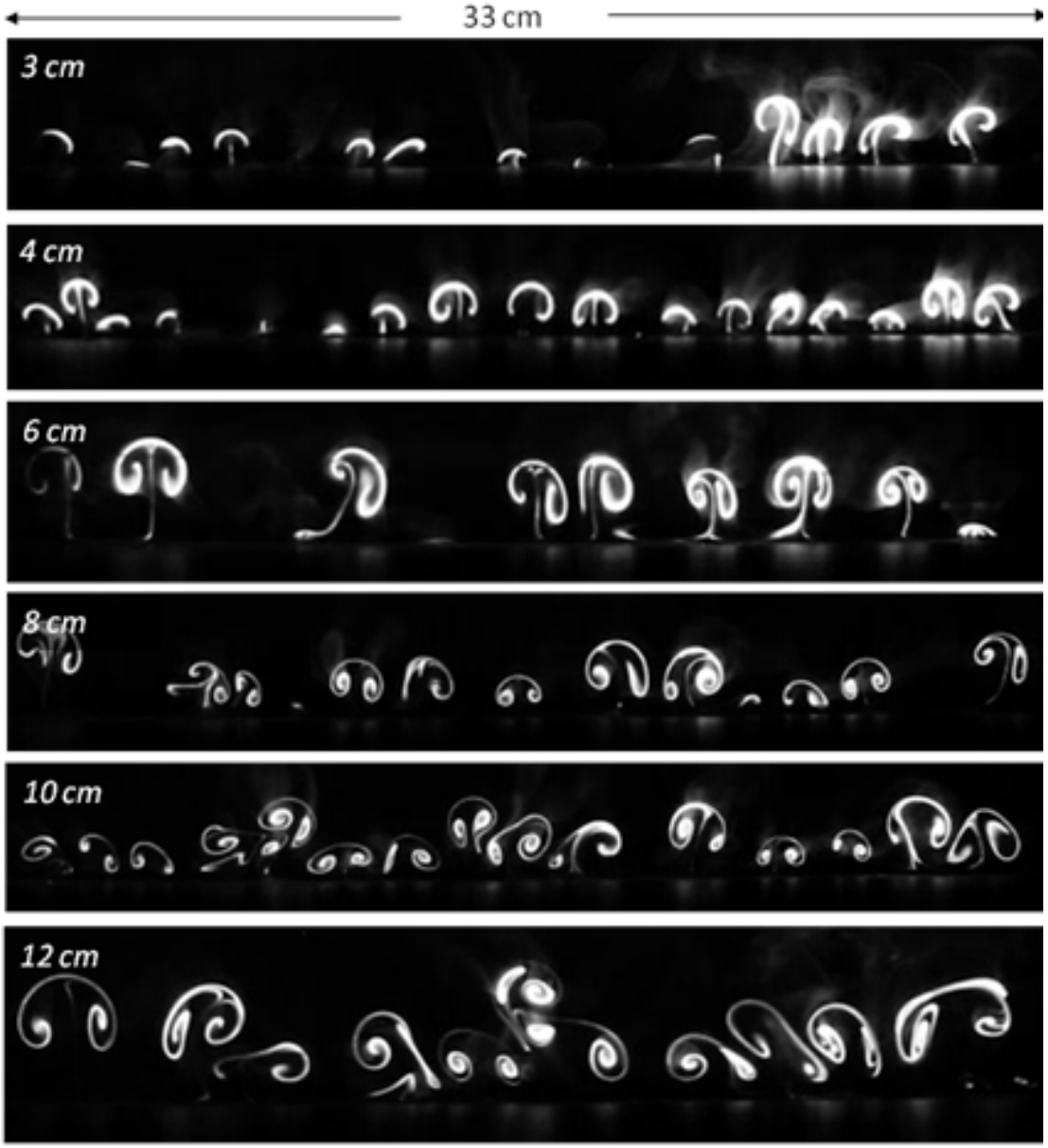

Figure 4.19 Examples of organized flow of vortex pairs between $3 \leq x \leq 12$ cm.

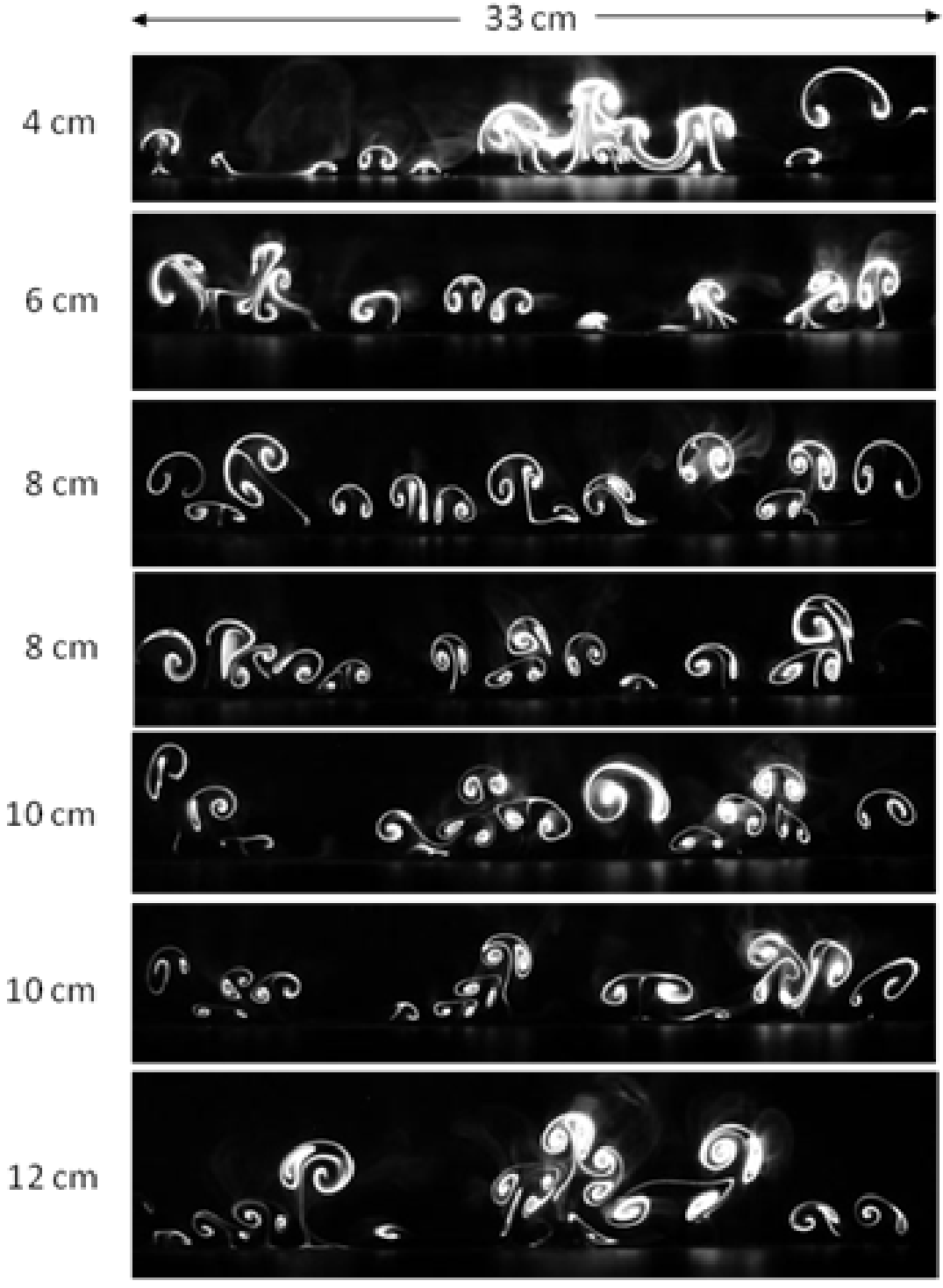

Figure 4.20 Examples of vortex pairs' interactions between $4 \leq x \leq 12$ cm.

4.4 Comparison of wind tunnel burn results and non-reactive flow experiments

The visualized flow patterns were studied from a fire research perspective, with a vision to develop a new method which could potentially assist fire spread investigations. Hence, these non-reactive flow results were compared to data from wind tunnel burns that were conducted at Missoula Fire Sciences Laboratory [75]; scaling and the scaling laws that were discussed in Section 2.5 were also used in this assessment.

Figure 4.21 shows two images of the same test but with a difference in time of 1/15 sec. In these images, the rotational motion in a specific region is highlighted which leads to a down-wash flow (Figure 4.21b), in agreement with observations made by Finney's team, as depicted in Figure 4.22 [59]. In their research it was noted that this type of down-wash motion stimulated fire spread [59]. In the current results, as shown in Figure 4.21, the down-wash motion is a purely hydrodynamic effect driven by convection because no fire or chemical reactions were present.

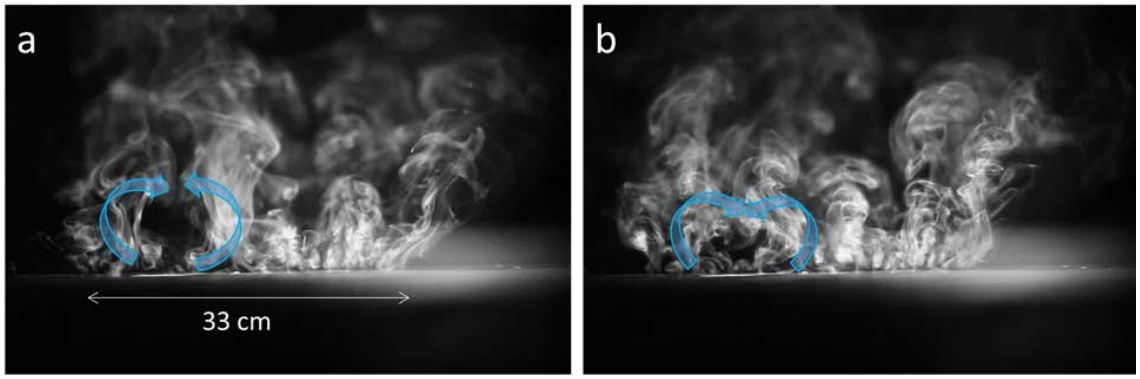

Figure 4.21 Time evolution of rotational flow within the transition region: a – 0 sec; b – 1/15 sec.

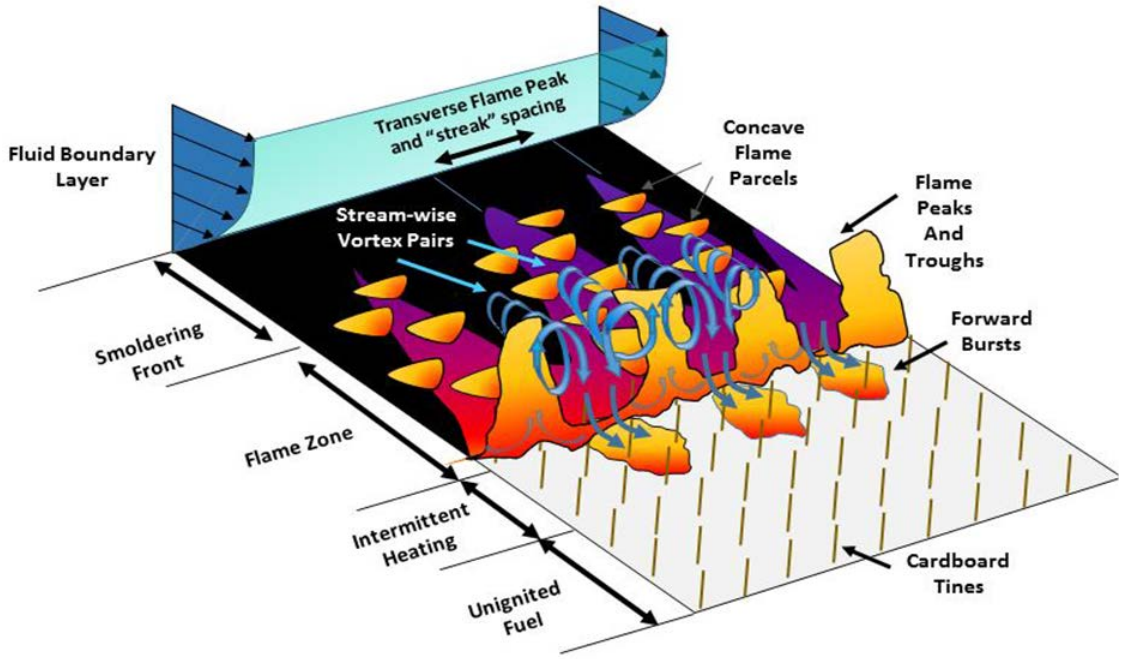

Figure 4.22 Schematic representation of flame propagating through a cardboard fuel bed [59] showing the down-wash motion that was associated with flame spread.

As a fire front propagates through a fuel bed in a wild land fire, its flame forms towers that are separated by valleys. Additionally, the flames form "mushroom shape" upwardly moving peaks (Figure 4.23c) which are the main contributor to upward fluctuations in the fire front. The behavior was observed during the current laboratory visualization testing (Figures 4.23 a and b) in all of the organized, transition and turbulent regimes. It is a common assumption that fire fronts propagate within a turbulent regime, for both wind tunnel and field burns. This assumption can be validated by careful examination of a propagating, large-scale fire by considering regions ahead of and behind the fire front (Figures 4.23c, 4.24 b and d). However, it is not clear if this assumption holds within the fire zone.

In addition to the "mushroom shape" structures circled in white on Figures 4.23 a and b, the vortex tubes circled in red represent horizontal flow which persisted until the transition region where it begins to rise. These types of vortex pairs were observed within the flame zone from a top, upstream view, shown in Figure 2.24a, but the inner flow structure within the fire zone could not be imaged because of being masked by the flame itself.

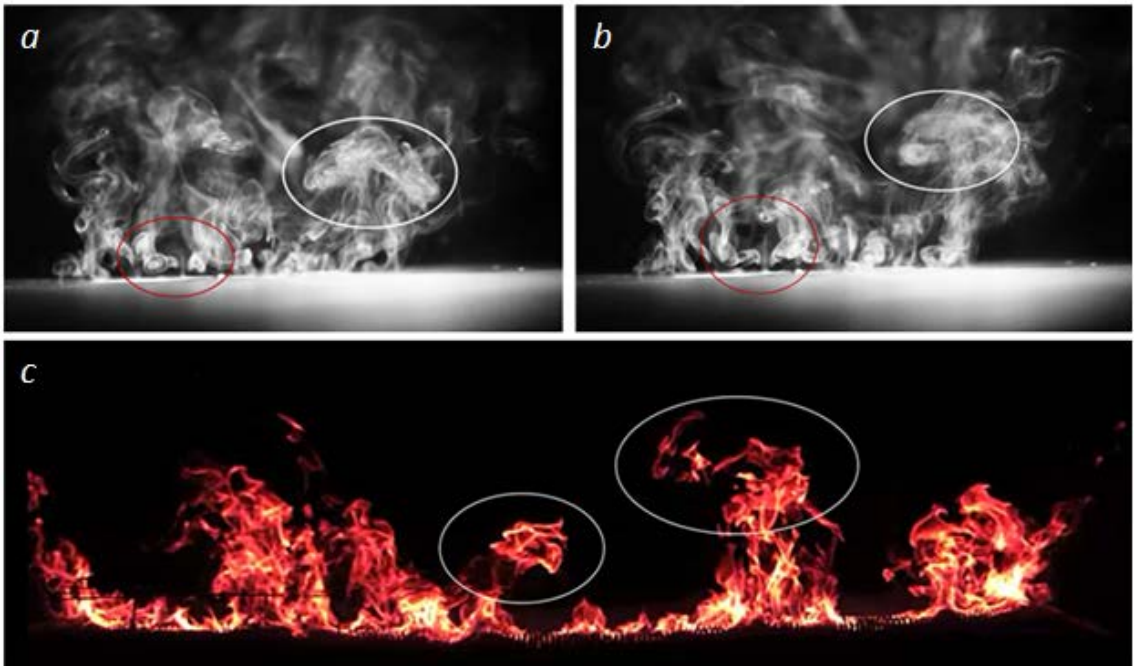

Figure 4.23 Comparison of non-reactive flow behavior (a and b) and wind tunnel fire (c).

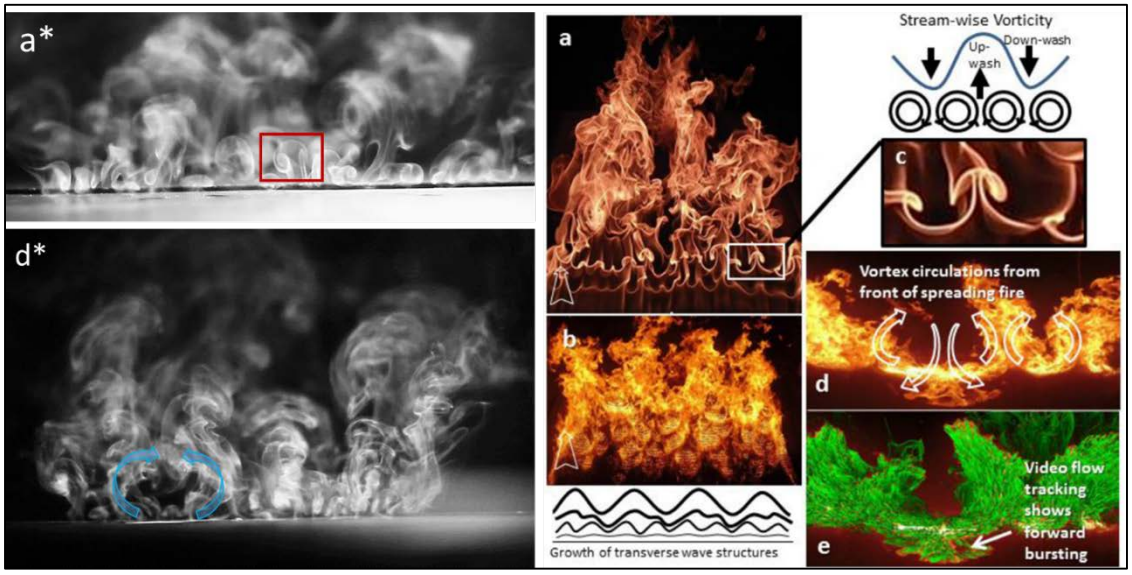

Figure 4.24 Similarities between non-reactive flow behavior and wind tunnel burns [59]. Where a* and d* present flow behavior similar to fire shown at a and d.

Figure 4.19 at distances between $3 \leq x \leq 8$ cm shows behavior similar to the well-known phenomena called Görtler vortices which have been observed in wind tunnel burns [59]; this Görtler behavior is represented by well-organized flow of discrete vortex pairs moving parallel to each other. At distances larger than 8 cm in the current study,

interactions between vortex tubes were initiated and created flow instabilities and vertical fluctuations; this type of behavior was also detected in wind tunnel burns [59, 90, 116].

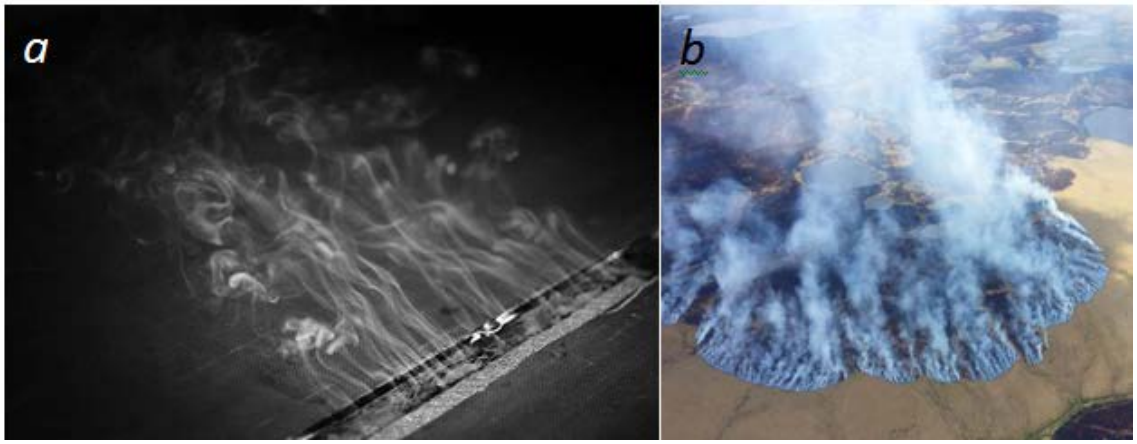

Figure 4.25 a – present research result, b – large scale wildland fire in Alaska [75].

As can be seen in Figure 4.25 a and b, distinct similarities exist between the behavior of smoke motion in the current laboratory-based images and those from large–scale, wild land fires. In both cases, the smoke moved parallel to the experimentation base or the ground and then began to rise. Despite the fact that, in a wild land fire, the temperature of the fire zone, would be much higher than the surrounding the smoke flow, the smoke remained in almost horizontal flow and then downstream it transitioned into convective–driven, upward moving flow. This behavior is similar to the current laboratory results. The horizontal flow ahead the fire front for the wild land fire may potentially be associated with piloted ignition because it can carry hot gases and ignited particles downstream to the unburnt fuel.

To assess comparisons between the current research and wind tunnel burns, the following scaling laws were applied.

$$\pi_1 = \frac{F_{i,up}}{F_b} = \frac{\rho_1 u^2}{\Delta\rho_1 L_w g} = Froude\ number$$

$$\pi_3 = \frac{Q_{c1}}{Q} = \frac{c_p \rho_1 l_2 L_a R \Delta\Theta_1}{I L_w}$$

$$\pi_7 = \frac{F_{i,down}}{F_{i,up}} = \frac{L_e w}{u} = Strouhal\ number$$

where ρ_1 = density of air and gas at ambient temperature, $\Delta\rho_1$ = density change of air and gas associated with temperature rise, u = horizontal velocity of air and gas, L_w = flame depth, g = gravitational acceleration, L_e = effective length where a major heat transfer occurs, w = flame burst frequency, c_p = specific heat of gas at atmospheric pressure, L_a = height of fire plume, R = velocity of flame spread, $\Delta\Theta_1$ = temperature rise of air and gas, l_2 = width of the fuel bed, I = fire intensity, F_b = buoyant force, $F_{i,up}$ = inertial force upstream the flame zone, $F_{i,down}$ = inertial force downstream the flame zone, Q = heat generated, and Q_{c1} = heat stored in air and gas associated with temperature rise.

These three pi-numbers were calculated for the current laboratory experiments - considered the model, and the wind tunnel fire experiments - considered the full scale, using the following relationships where prime symbol represents the laboratory experiments and those without the symbol represent wind tunnel experiments.

- $c_p = c_p'$
- $\rho_1 = \rho_1'$
- $L_a/L_a' \approx 38$, $L_a \approx 1.5$ m and $L_a' \approx 0.04$ m: L_a was approximated by examining previously published data [116]. L_a' was the height estimated by using the IR camera and represented the distance at which the smoke temperature was significantly higher than ambient temperature.
- $R/R' \approx 12.5$, $R \approx 1$ m/s based on previously published data [90]. In this particular case R' was assumed to be equal to horizontal flow velocity (0.08 m/s).
- $\Delta\theta/\Delta\theta' \approx 1000/200 = 5$
- $l_2/l_2' \approx 2/0.33 \approx 6$, where l_2 was from previously published data [90, 116, 75]; l_2' was the heater length (0.33 m).
- $L_w/L_w' \approx 1/0.035 \approx 29$, where L_w was taken from previously published data [90, 116, 75]; L_w' was the heater width (0.035 m).
- $L_e/L_e' \approx 1/0.02 \approx 50$, where L_e was taken from previously published data (using thermocouples) [90, 116]; L_e' was the distance estimated by using the IR camera and represented distance at which the smoke temperature was significantly higher than ambient temperature.
- $u/u' = 1/0.08 = 12.5$.

- w/w’ = 0.5/2, where w was based on previously published data [90]; w’ was approximated from the visualization results.
- I/I’ = 25/0.08 = 312.5, I’ = 2 kW/m^2*0.04m = 0.08 kW/m, where the value of I was from previously published data [90].

The scaling resulted in the following relations:

$$\pi_1 = k_1*\pi_1' \quad k_1 \approx 1; \qquad \pi_2 = k_2*\pi_2' \quad k_2 \approx 1; \qquad \pi_4 = k_4*\pi_4' \quad k_4 \approx 2.$$

Where: k_1, k_2 and k_3 were the scaling constants.

All three Pi-numbers were satisfied, which confirmed that both phenomena were governed by the same physics.

CHAPTER 5: CONCLUSIONS

The goal of the research was to develop a new approach for assessing fire spread that is based on experimentation in which the chemical reaction of fire, i.e. the flame, is eliminated; in the current research, a flame was replaced by using a precisely controlled electrical heater. Significant advantages were envisioned in this approach because it simplified attributes for examining fire spread and enabled precise visualization studies for the fluid dynamic aspects of fire spread which previously have been mostly masked by flames. Furthermore, convective-driven fire spread was the main interest; hence, experimental procedures were established in which radiative heat transfer was negligibly small.

A low speed wind tunnel was constructed and used in which the fire zone was represented by convective heat flux from a heater's surface and visualization of smoke flow from it. Interactions between buoyant and inertia forces, which were considered to be the main hydrodynamic forces governing convective-driven fire spread, were identified within vortex pairs of smoke streaks that were formed initially at the heater's surface. These interactions were visualized in both 3D and 2D structures illuminated by LED lighting and a sheet of light from a green emitting laser, respectively. These images provided detailed flow behaviors which were then carefully studied and compared to both wind tunnel and field burn results. Strong similarities in behavior were found between the laboratory data and the wind tunnel and field burn data even though the laboratory experimentation was accomplished with no flame. Appropriate scaling laws were established and they were used to quantitatively correlate the non-reactive flow data with data from wind tunnel burns; the three Pi-numbers that had been developed were satisfied. Therefore, the non-reactive flow approach is seen as applicable for studying and understanding fire spread.

5.1 Current results and future work from a fire research perspective

The results of the current work were mostly compared to the wind tunnel burns because of similarities in experimental environments for both cases. Horizontal airflow velocities can be well controlled in both cases and assumed to be predominantly unidirectional because of the wind tunnel designs; in the wind tunnel burns to which the

current data were compared, the airflow direction was in the direction of the fire spread. Fuel properties, and consequently temperature and heat fluxes, were known for the burns as were the temperatures and convective heat fluxes during the current research. These aspects enabled the application of appropriate scaling laws with variable flux and temperature, a feat previously impossible to accomplish because combustion temperatures were almost independent of fuelbed size. This aspect of the current results opens new opportunities in fire scaling.

The scaling laws were firstly applied to correlate results from wind tunnel burns to those of full-scale wild fires and then matched them with results from the non-reactive flow experiments. As was discussed in Section 2.5, all scaling parameters were satisfied in the correlation between wind tunnel burns and wild fires except for the parameter representing flame tower width (l_2); existing scaling laws did not give predictability for this parameter. Hence, it was replaced by the ratio of the fuelbed width to heater length, which then enabled a match between the wind tunnel burns and the current flow visualization results. However, the fuelbed width is not always an appropriate representor of scale length because flame heights, depths and pulsing frequencies may not depend on the width whereas it will depend on fuel properties like their dimensions. Unfortunately, as in was mentioned in Chapter 2, a consideration of all fuel properties is an extremely complicated task. Perhaps flame tower width, which represents a wavelength normal to the direction of fire spread (see Figure 2.3), could be an appropriate length of scale because it can be easily measured and correlated to other parameters such as flame height. Therefore, it is suggested that future research assess whether appropriate scaling laws can be developed using the flame tower width as a length of scale.

The visualization research that was accomplished showed that the behaviors of a flame propagating through a fuel bed and of smoke flow above and downstream of a heater were very similar. The heater's surface was considered to be representative of a flame zone, and was particularly useful for the scaling analysis. Indeed, differences in flow behaviors from a fire versus from the non-reactive heat transfer experiments do exist because of the significantly lower temperature of the heater (200^{o}C versus approximately 1000^{o}C in a fire) and the fact that the heater provided heat flux from the horizontal surface while in real fires the heat flux is from the entire height of a flame. This latter

difference may be crucial because in the current setup the hottest point was on the heater's surface while in the case of a fire the flame tip is the hottest spot which is usually at some distance from a floor or ground. However, the non-reactive flow visualization setup can be used to investigate flow behavior upstream of a flame zone in a real fire. For example, assume a horizontal wind in the direction of fire spread; in this case, the burned fuel behind the flame zone still has a relatively high temperature which would induce buoyant driven upward air motion. This upward motion interacts with the horizontal wind and creates vortices, described in Chapter 4, which then interact with the fire zone. Therefore, the fire zone would experience a rotational upward flow which could affect fire front structure. This rotational smoke motion, passing into the flame zone from behind, was observed by Finney's team during wind tunnel burns. As described in Section 4.3.1, the effect of such flow is a function of wind velocity; it will be necessary to conduct visualization studies of flow fields upstream of a flame zone to confirm these possibilities.

Extensive similarities were discovered to exist in wind tunnel burns and non-reactive smoke flow experiments; the latter experimentation showed detailed flow structures which, potentially, could be masked by flames in fire experiments. Therefore, an extreme need exists to develop advanced visualization techniques applicable to flame zones. Perhaps both IR and visual cameras, fitted with appropriate filters, and coupled with PIV techniques (Particle image velocimetry) could be further adapted for such investigations.

5.2 Current results and future work from the fluid dynamics perspective

Flow visualization results demonstrated flow features which deserve additional attention from a fire research perspective and from a fluid dynamics point of view. Both 3D and 2D visualization results showed that vortex pairs were initiated at the heater's surface, they continued to flow downstream in an organized manner at a small angle relative to the horizontal, i.e. base of the test section, and then, within the transition region, the flow direction moved upwards (Figures 4.18 and 4.23 a, b). The only possible cause of upward motion was the buoyant force which was due to a temperature difference. Although the largest temperature difference and, consequently, the largest

buoyant force should have been above the heater, the flow above it remained almost horizontal. Further downstream, the smoke temperature was near the ambient temperature but the vertical velocity was larger than above the heater; in contrast, the horizontal velocity remained approximately constant along the entire test section. Additionally, the duration of the transition region was much shorter than the durations of other regions whereas its location and length depended on the horizontal airflow velocity. To discover reasons for such flow behavior, it would be worthwhile to conduct experiments similar to those within the current study but in a better designed and controlled wind tunnel having a different size with a precise variation of a heater's temperature and the wind velocity.

The 2D visualization data provided detailed flow structure information and the identification of discrete vortex tube pairs that continued to flow downstream and parallel to each other at distances between $3 \leq x \leq 8$ cm (Figure 4.19). At larger distances between $9 \leq x \leq 14$ cm, these vortex tubes interacted intensively with each other. These interactions strongly deformed the vortex tubes, as shown in Figure 4.20; however, no mixing or merging of vortices was observed in this region. Instead, mixing and vortex merging occurred at distances greater than 14 cm from the heater as the flow transitioned into a turbulent regime. Because these research data were correlated to data from fire experiments, which have large Reynold's number flows and therefore negligible viscosity effects, some of the flow features from the current research could not be explained.

Although the current work described flow structures in detail, a lack of quantitative data about them still exists. Therefore, in future research it would be worthwhile to use PIV techniques to measure flow fields in non-reactive flow experimentation. Rotational velocities of vortex tubes must be measured at different locations to further investigate flow evolution. Reynold's numbers based on rotational velocity and vortex diameters must be evaluated and compared to ones based on airflow velocity and test section dimensions to quantify viscosity effects. Reynold's number analysis might potentially explain the nature of the transition regime and interaction between vortices.

APPENDICES

Appendix A: Time Sequences of Approaching Flow (200ºC, 8 cm/s)

- x = 3 cm:

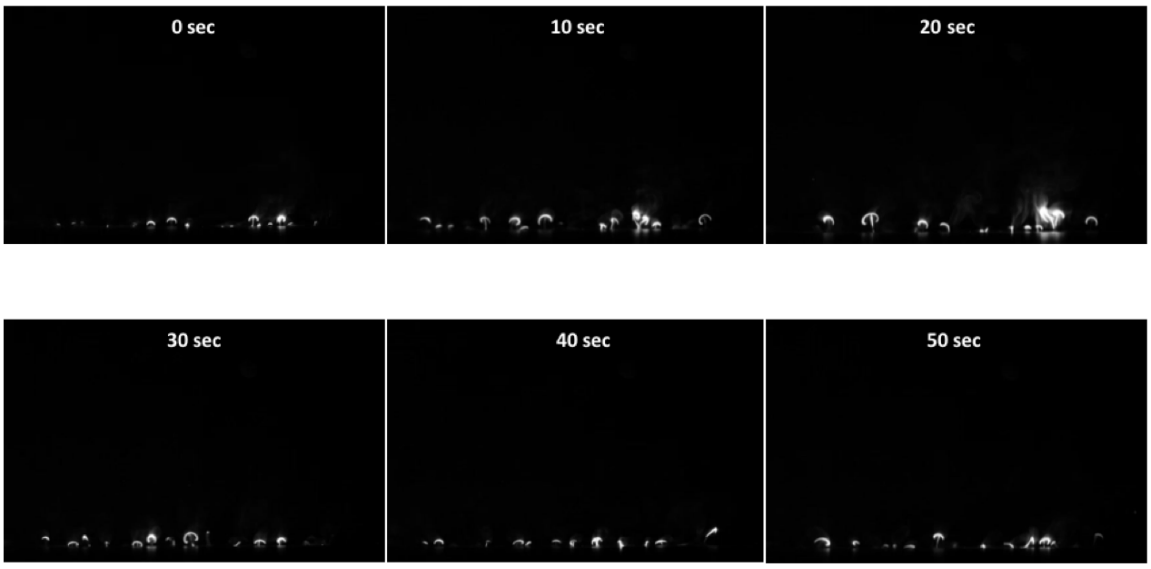

- x = 4 cm:

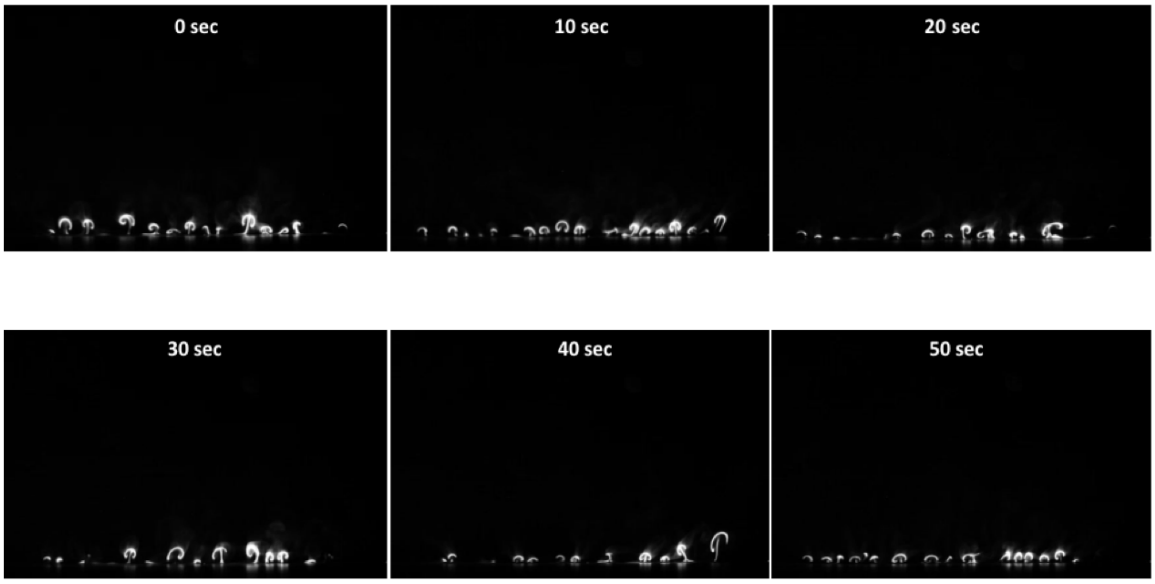

- x = 5 cm:

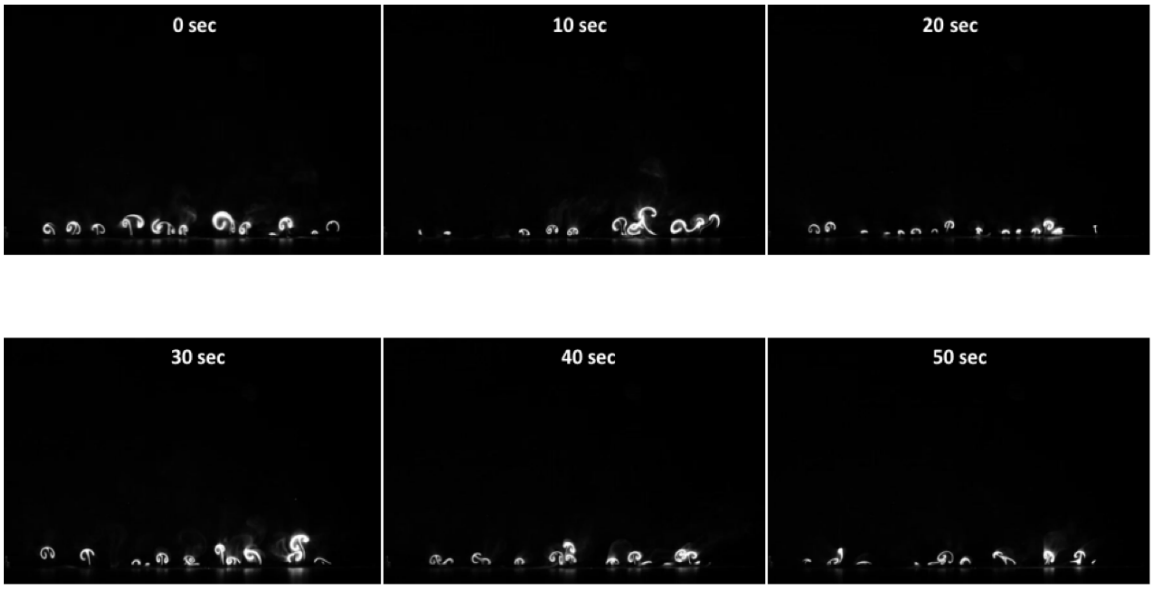
0 sec
10 sec
20 sec
30 sec
40 sec
50 sec

- x = 6 cm:

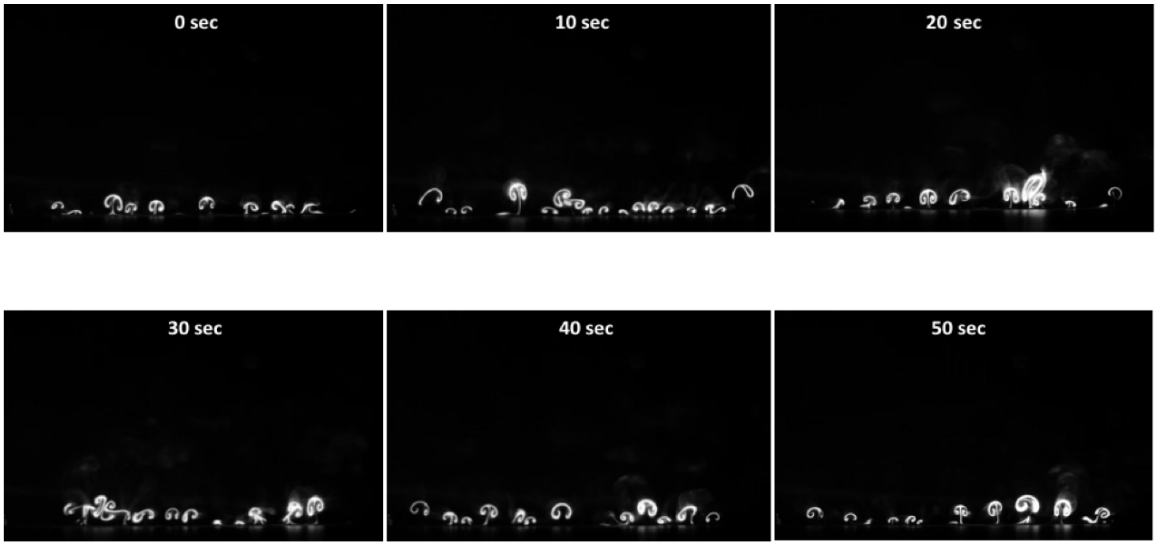
0 sec
10 sec
20 sec
30 sec
40 sec
50 sec

- x = 7 cm:

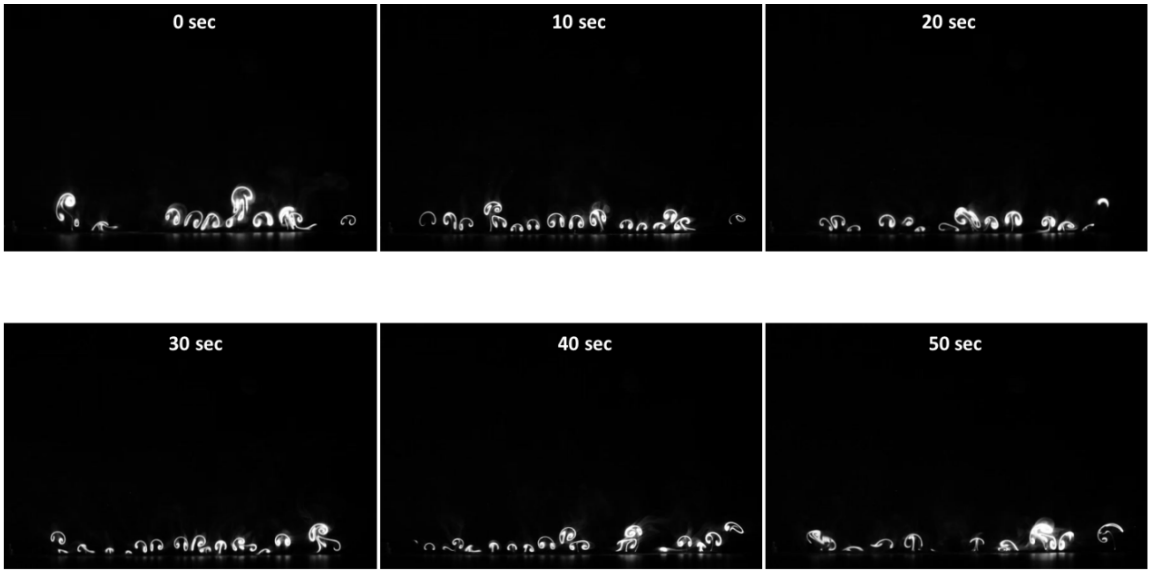
0 sec
10 sec
20 sec
30 sec
40 sec
50 sec

- x = 8 cm:

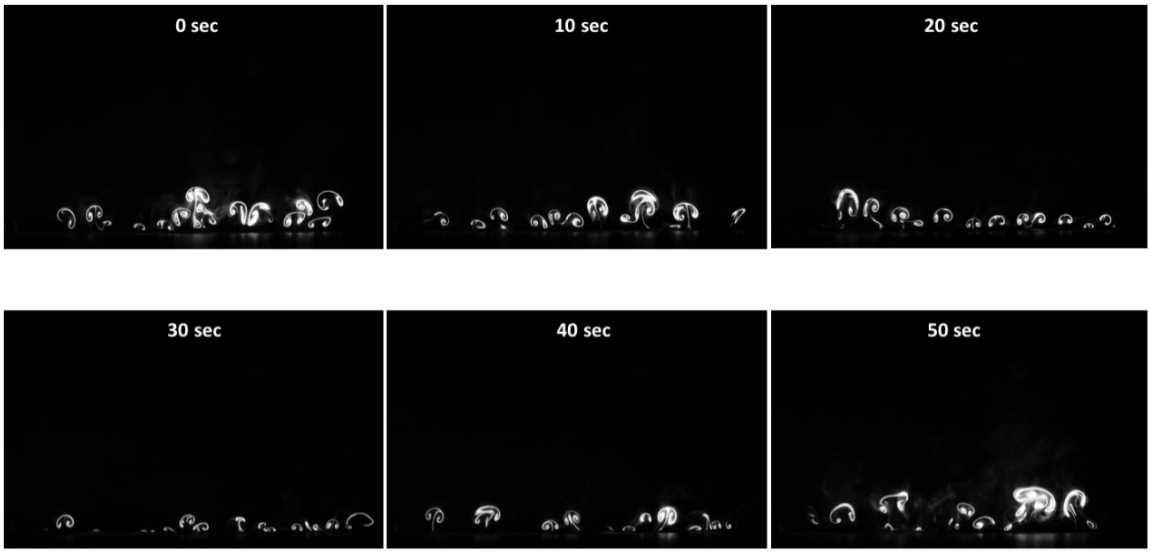
0 sec
10 sec
20 sec
30 sec
40 sec
50 sec

- x = 9 cm:

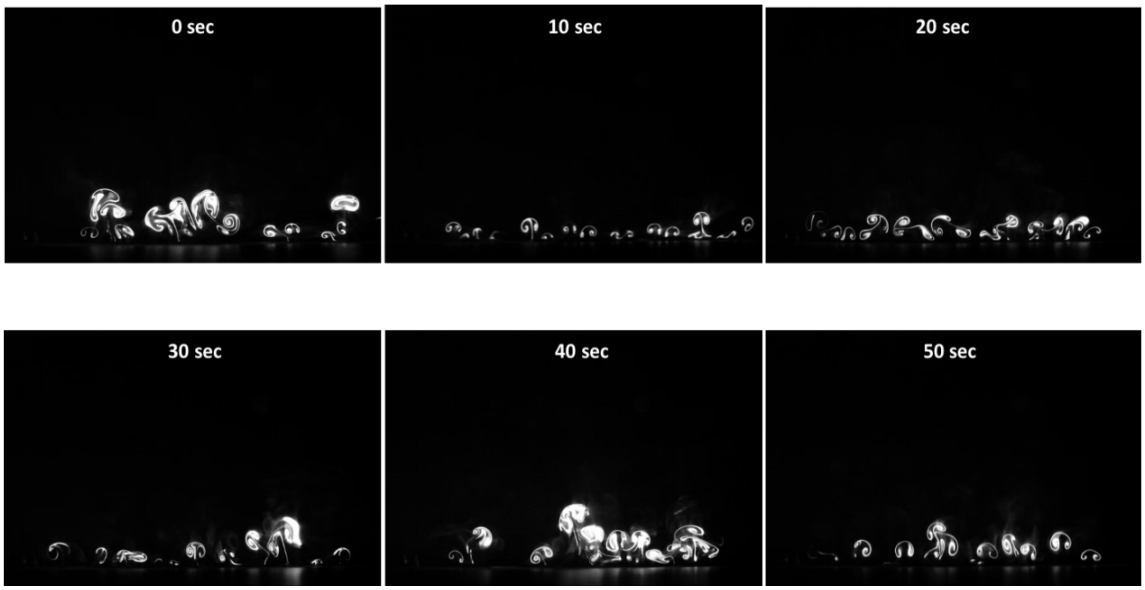
0 sec
10 sec
20 sec
30 sec
40 sec
50 sec

- x = 10 cm:

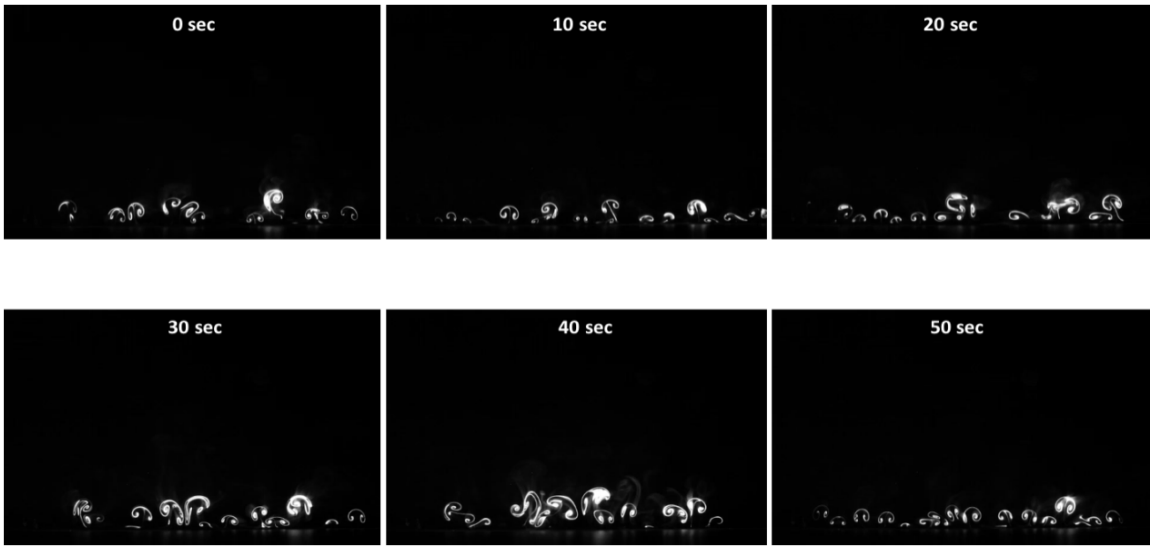
0 sec
10 sec
20 sec
30 sec
40 sec
50 sec

- x = 11 cm:

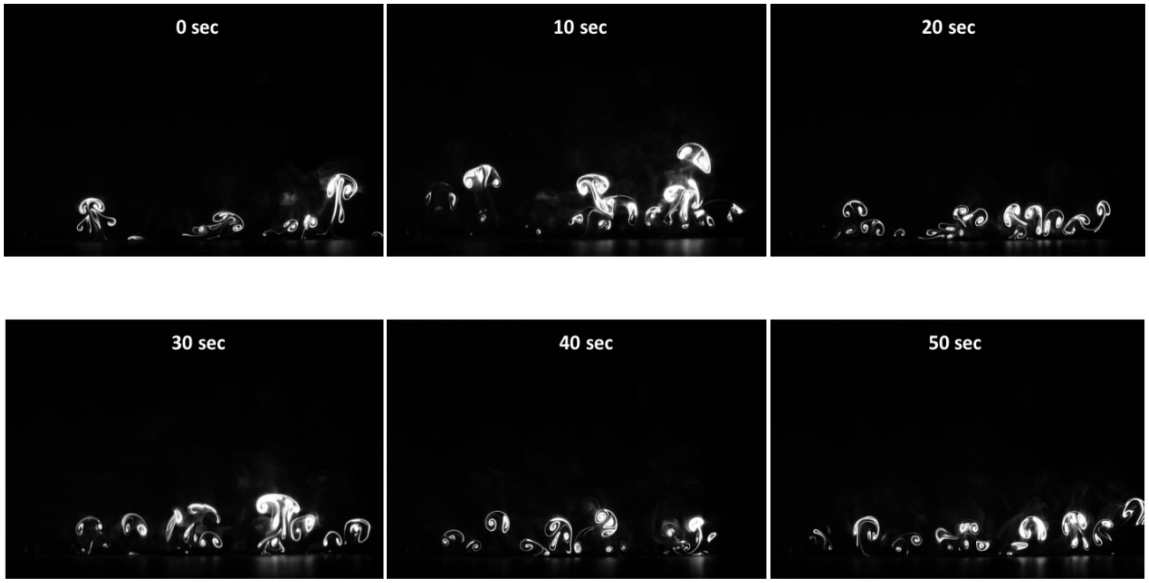
0 sec
10 sec
20 sec
30 sec
40 sec
50 sec

- x = 12 cm:

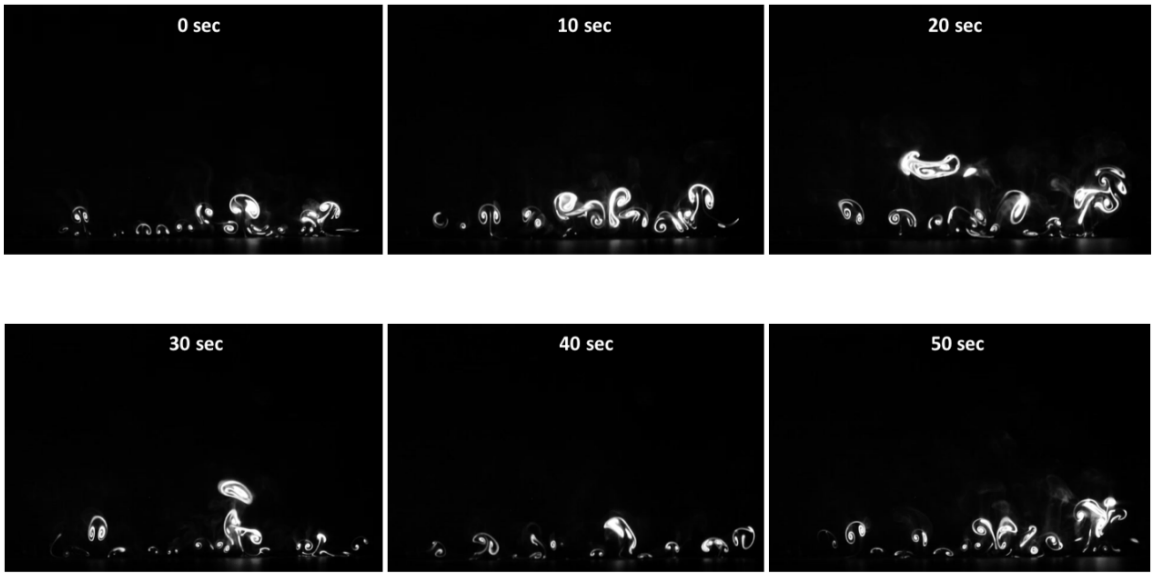
0 sec
10 sec
20 sec
30 sec
40 sec
50 sec

- x = 13 cm:

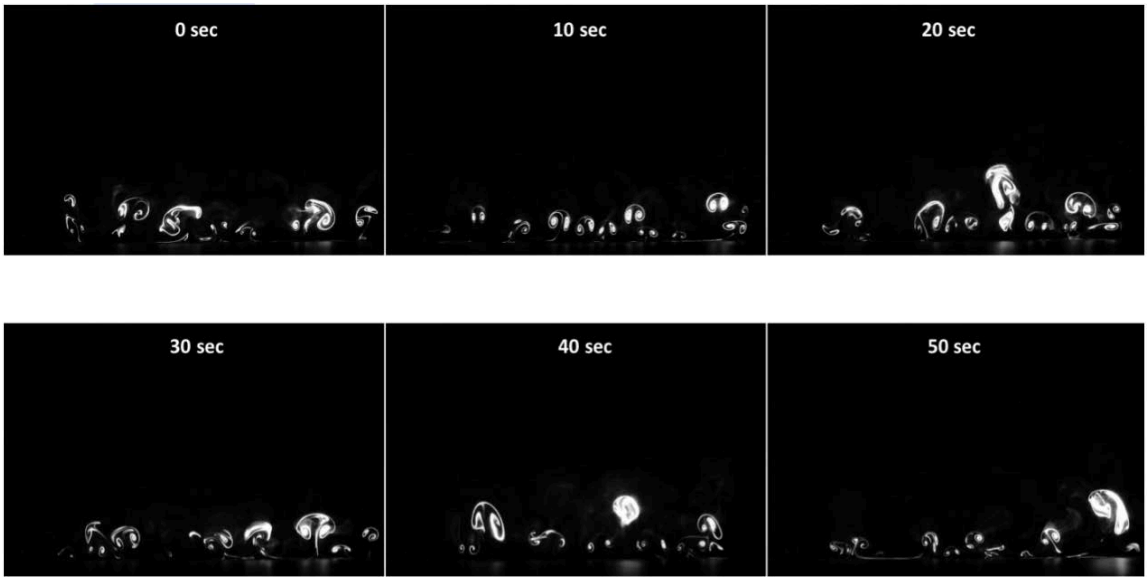
0 sec
10 sec
20 sec
30 sec
40 sec
50 sec

- x = 14 cm:

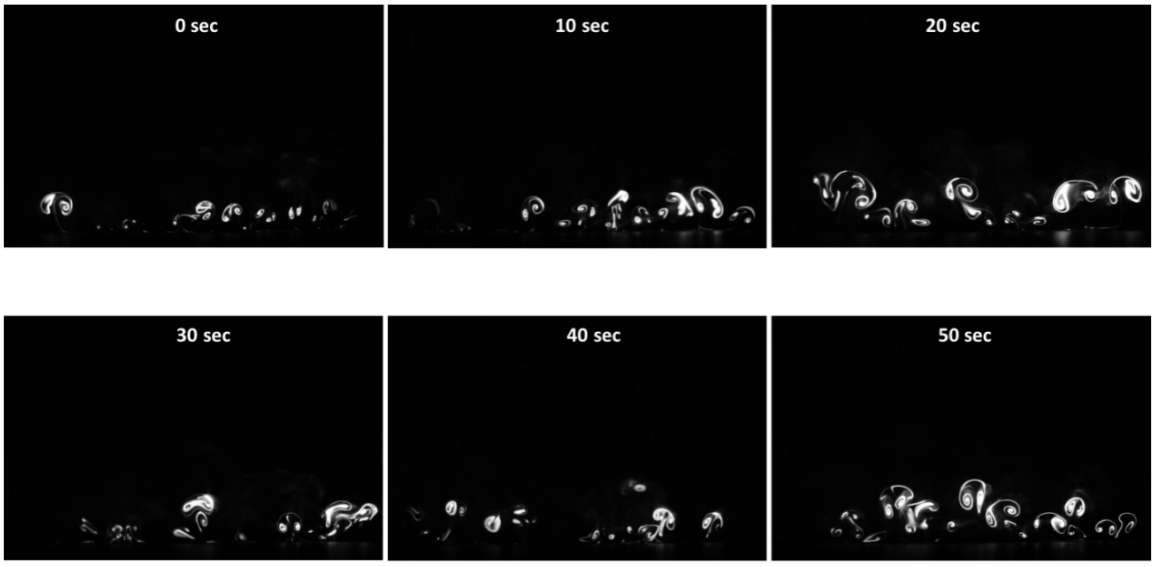
0 sec
10 sec
20 sec
30 sec
40 sec
50 sec

- x = 15 cm:

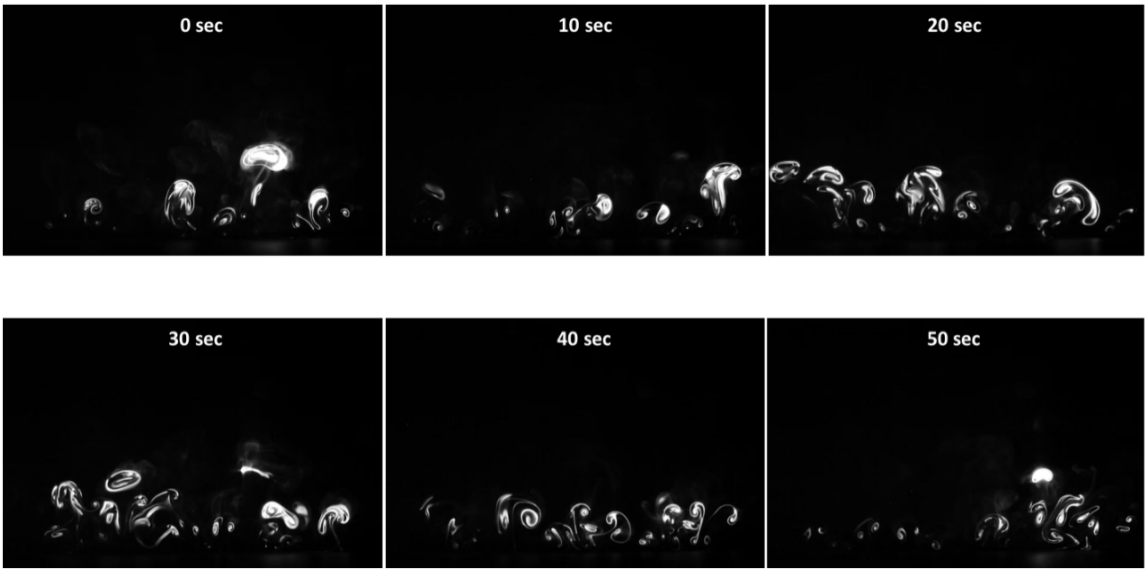
0 sec
10 sec
20 sec
30 sec
40 sec
50 sec

- x = 16 cm:

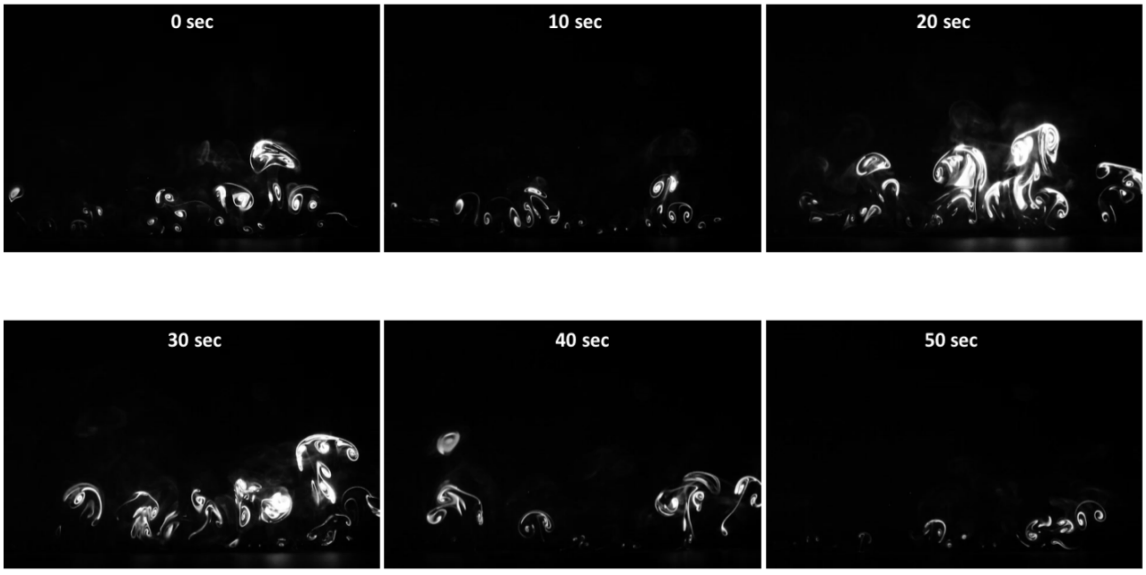
0 sec
10 sec
20 sec
30 sec
40 sec
50 sec

- x = 17 cm:

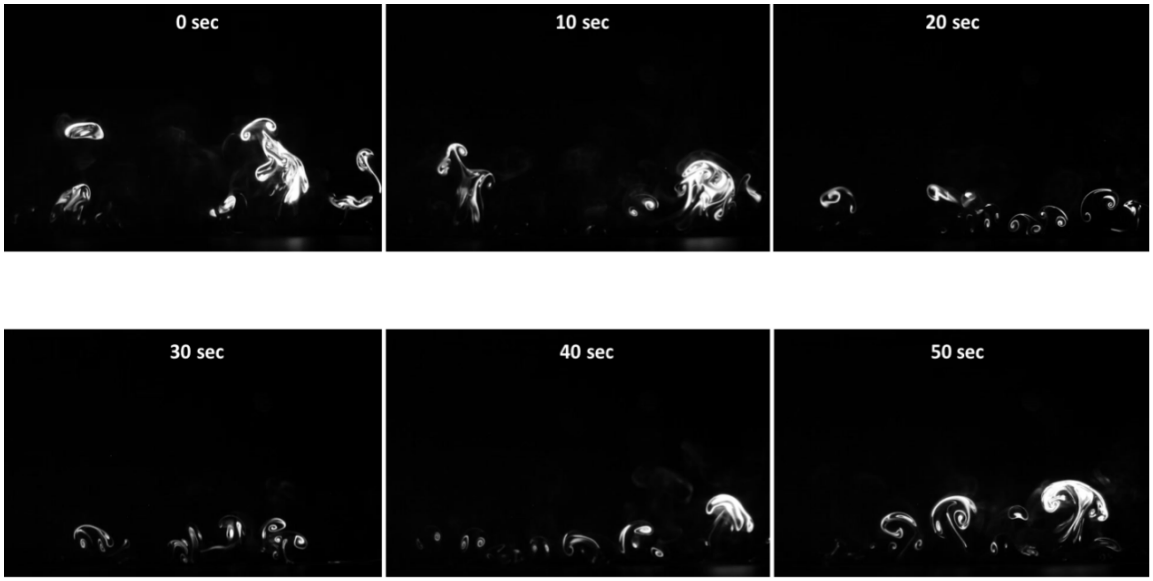
0 sec
10 sec
20 sec
30 sec
40 sec
50 sec

- x = 18 cm:

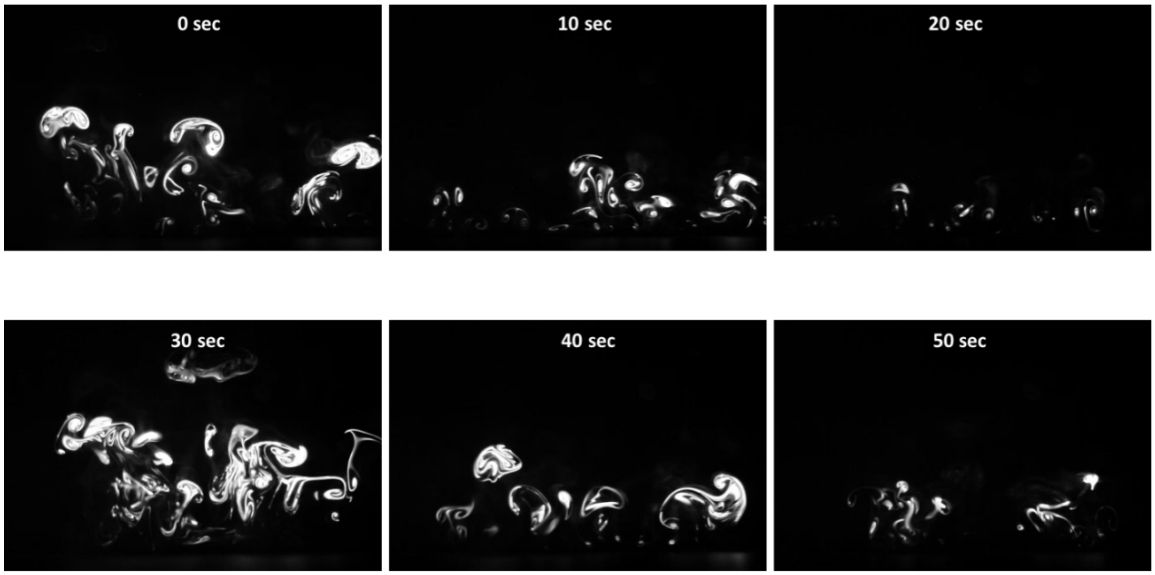
0 sec
10 sec
20 sec
30 sec
40 sec
50 sec

- x = 19 cm:

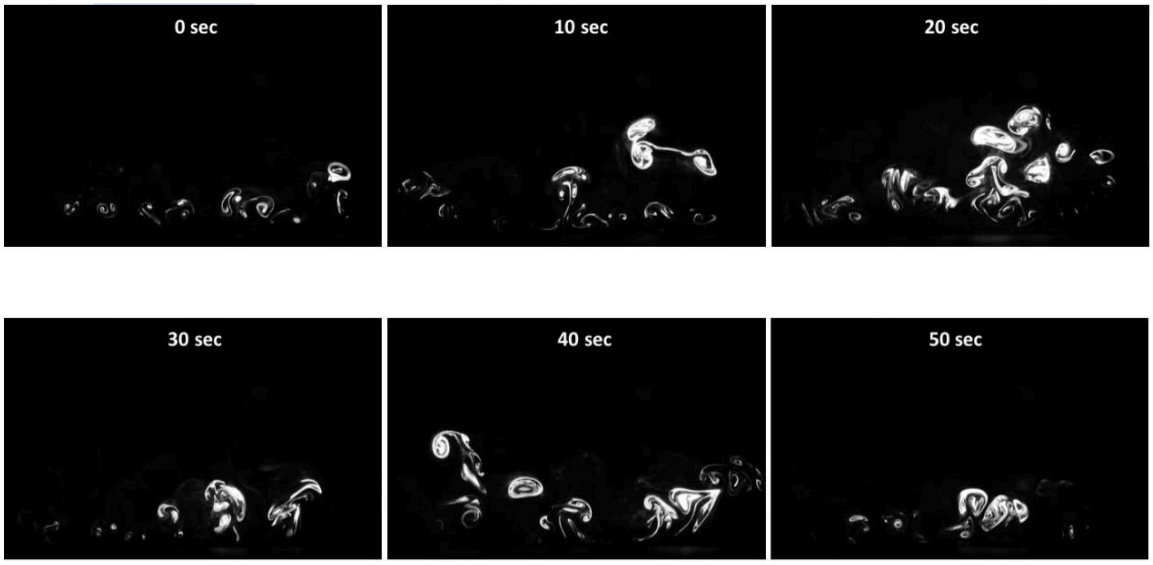
0 sec
10 sec
20 sec
30 sec
40 sec
50 sec

- x = 20 cm:

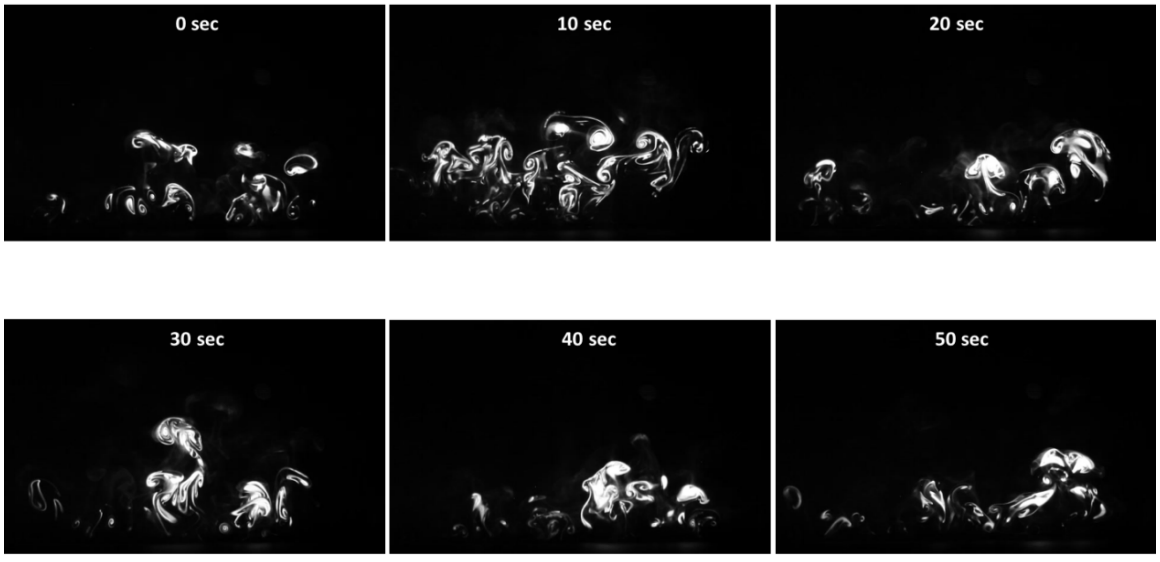
0 sec
10 sec
20 sec
30 sec
40 sec
50 sec

- x = 21 cm:

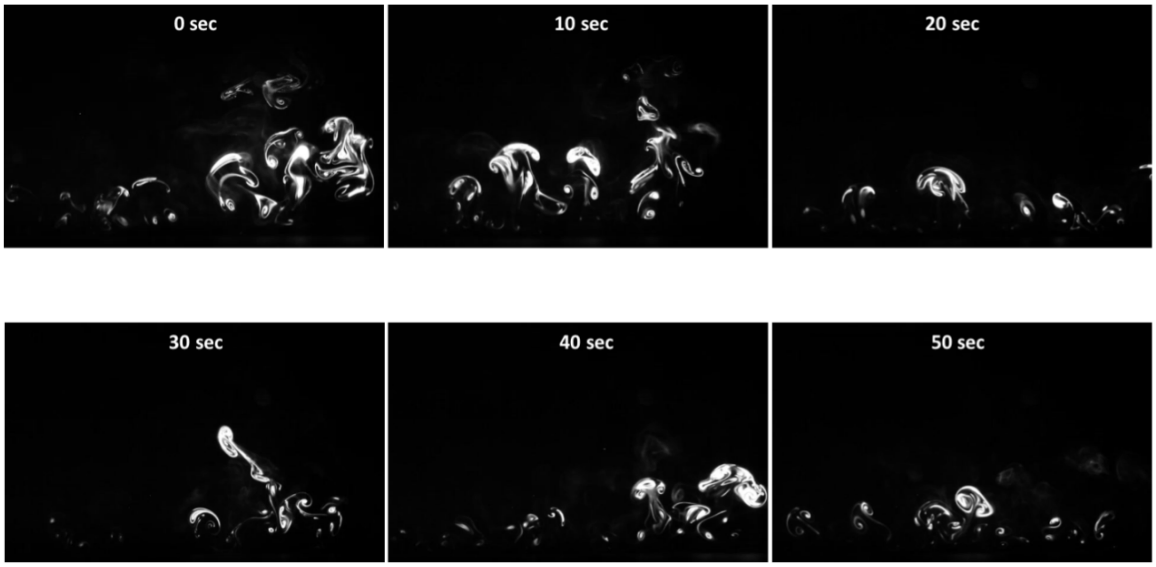
0 sec
10 sec
20 sec
30 sec
40 sec
50 sec

- x = 22 cm:

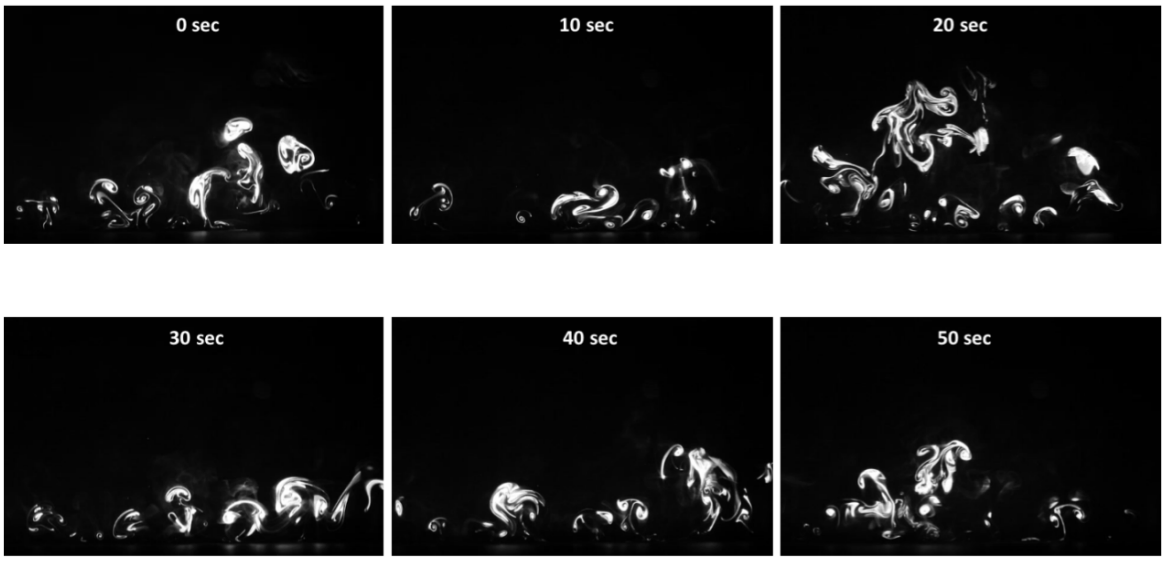
0 sec
10 sec
20 sec
30 sec
40 sec
50 sec

- x = 23 cm:

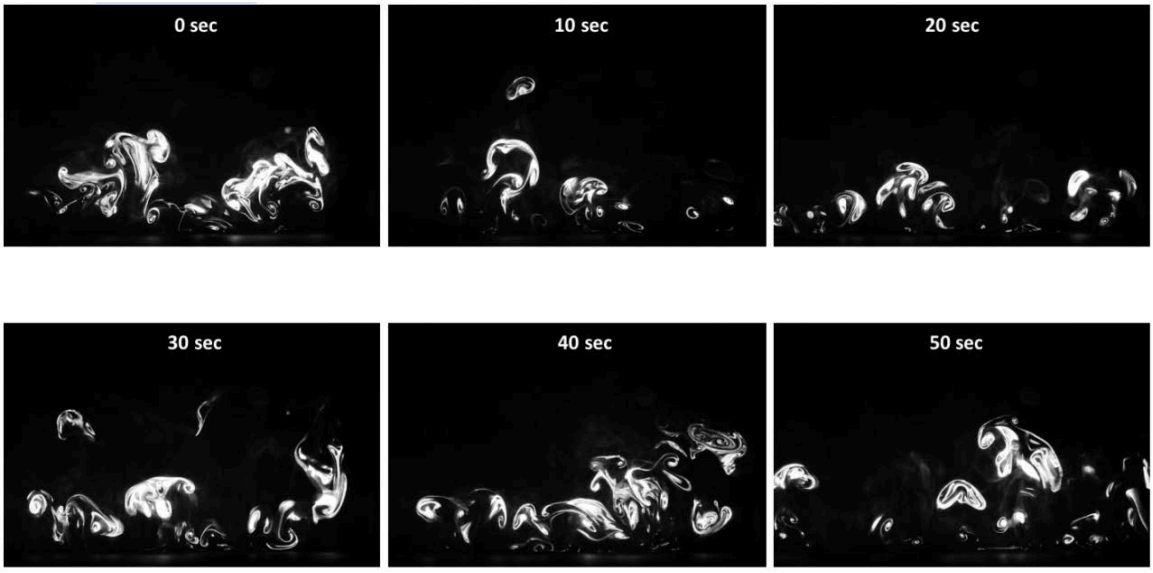
0 sec
10 sec
20 sec
30 sec
40 sec
50 sec

- x = 24 cm:

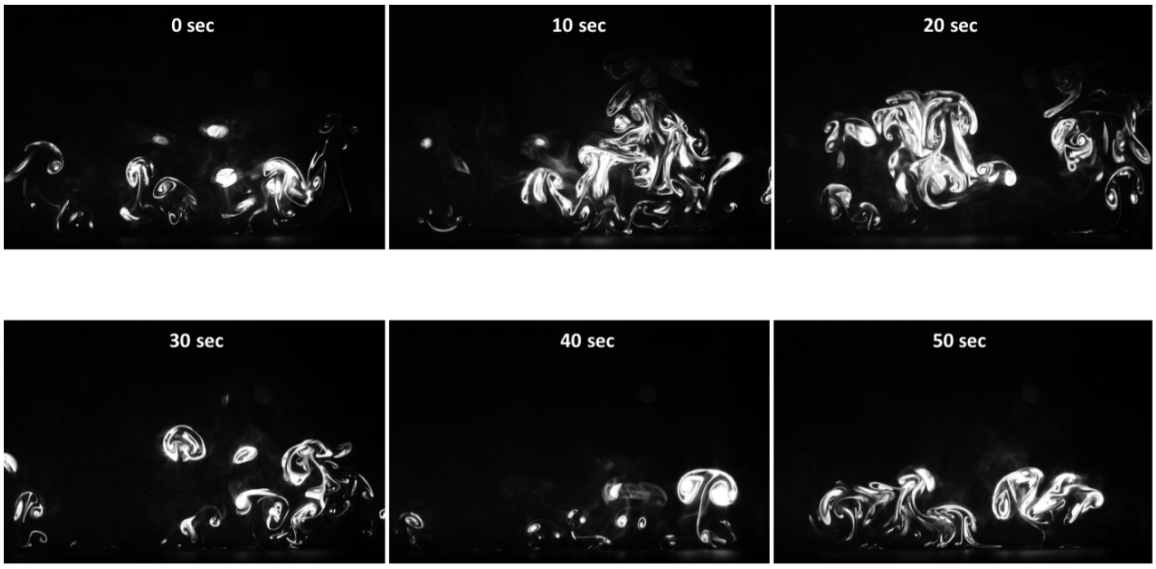
0 sec
10 sec
20 sec
30 sec
40 sec
50 sec

- x = 25 cm:

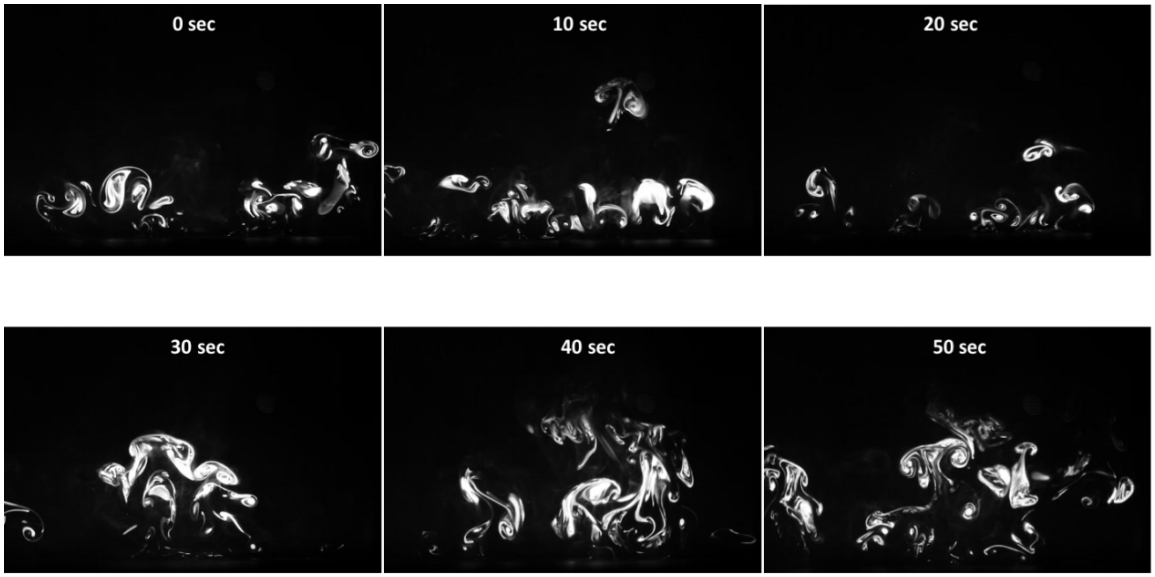
0 sec
10 sec
20 sec
30 sec
40 sec
50 sec

- x = 26 cm:

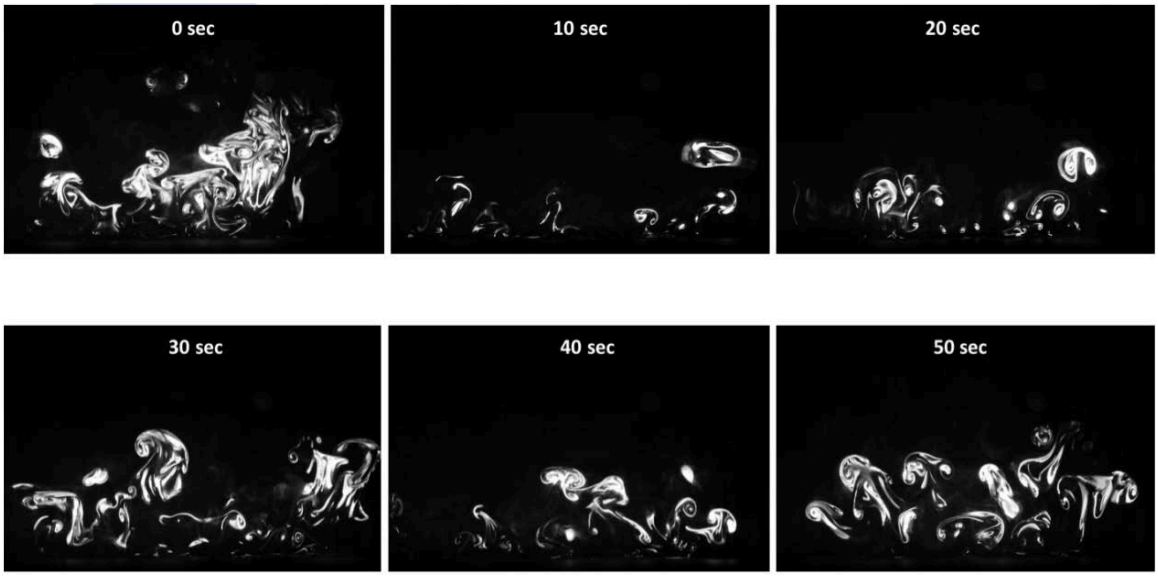
0 sec
10 sec
20 sec
30 sec
40 sec
50 sec

- x = 27 cm:

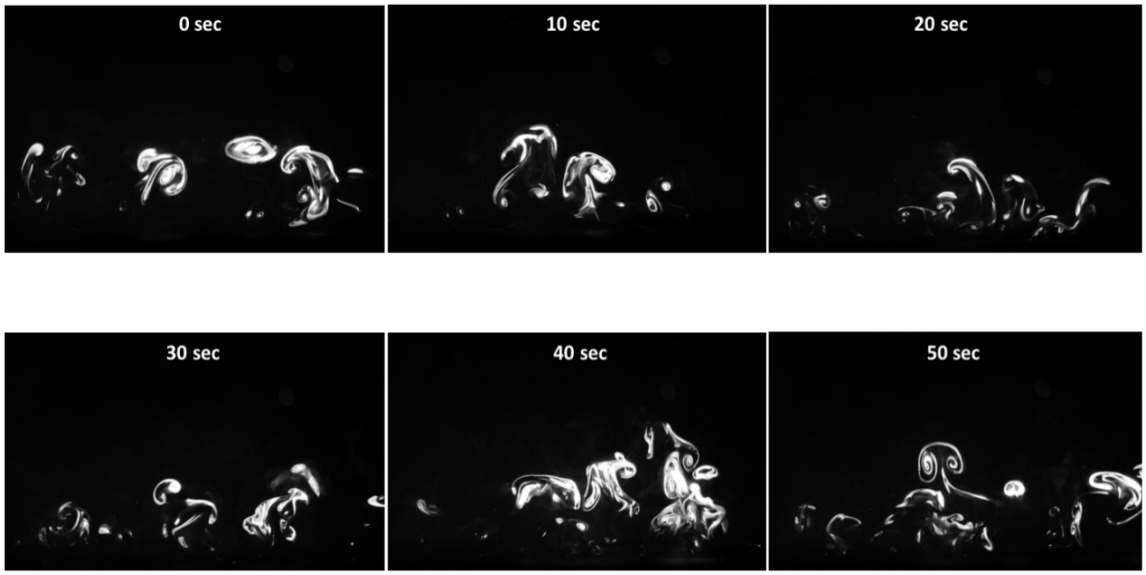
0 sec
10 sec
20 sec
30 sec
40 sec
50 sec

- x = 28 cm:

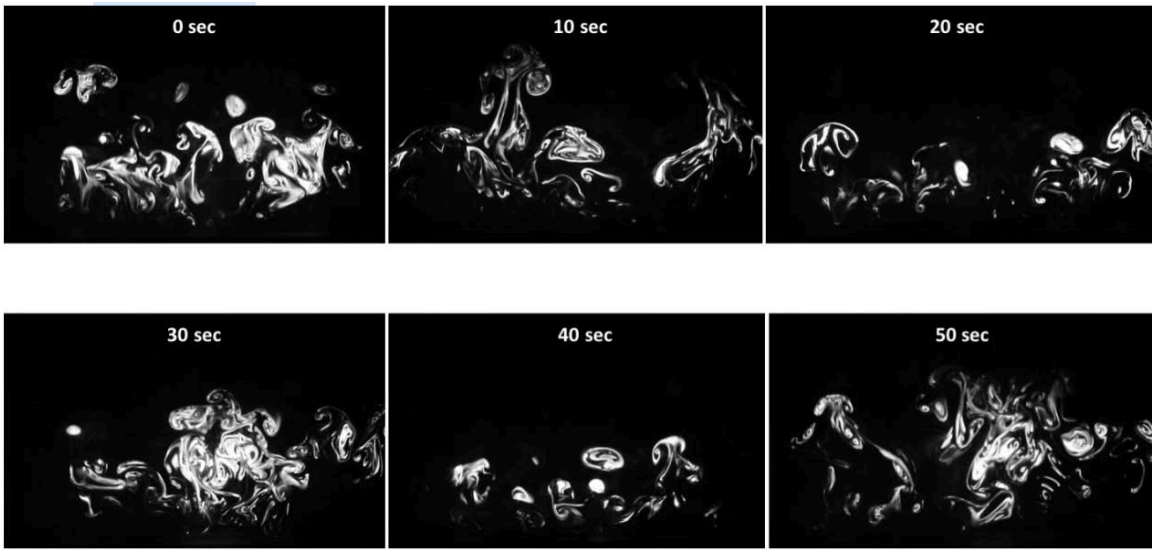
0 sec
10 sec
20 sec
30 sec
40 sec
50 sec

- x = 29 cm:

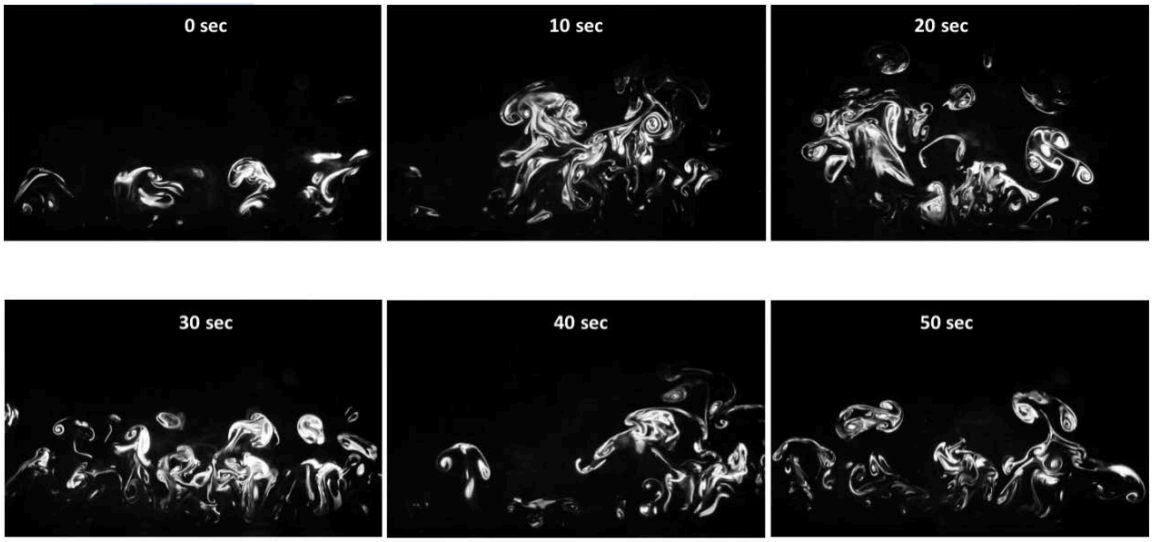
0 sec
10 sec
20 sec
30 sec
40 sec
50 sec

- x = 30 cm:

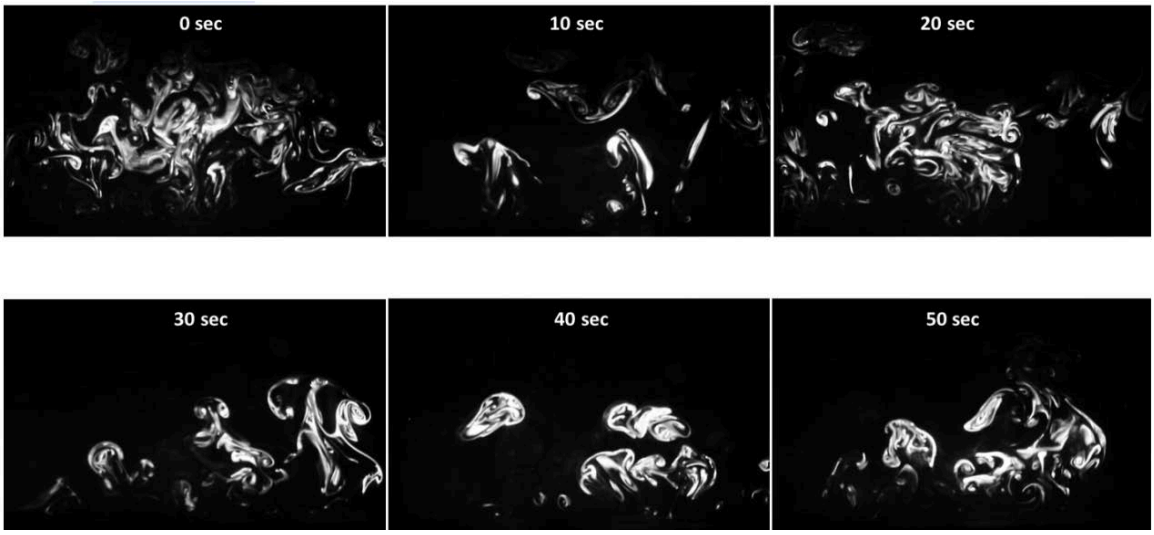
0 sec
10 sec
20 sec
30 sec
40 sec
50 sec

Appendix B: Flow Evolution (200°C, 8 cm/s)

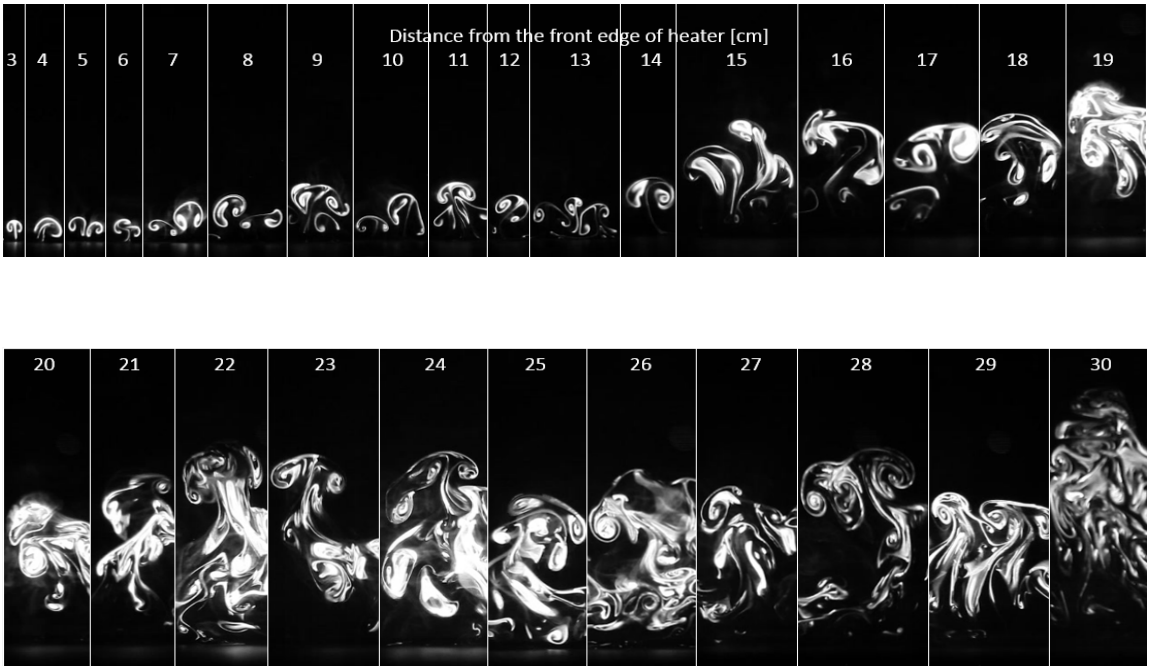

Appendix C: Vortex Pairs and Their Interactions (200°C, 8 cm/s)

- x = 3 cm:

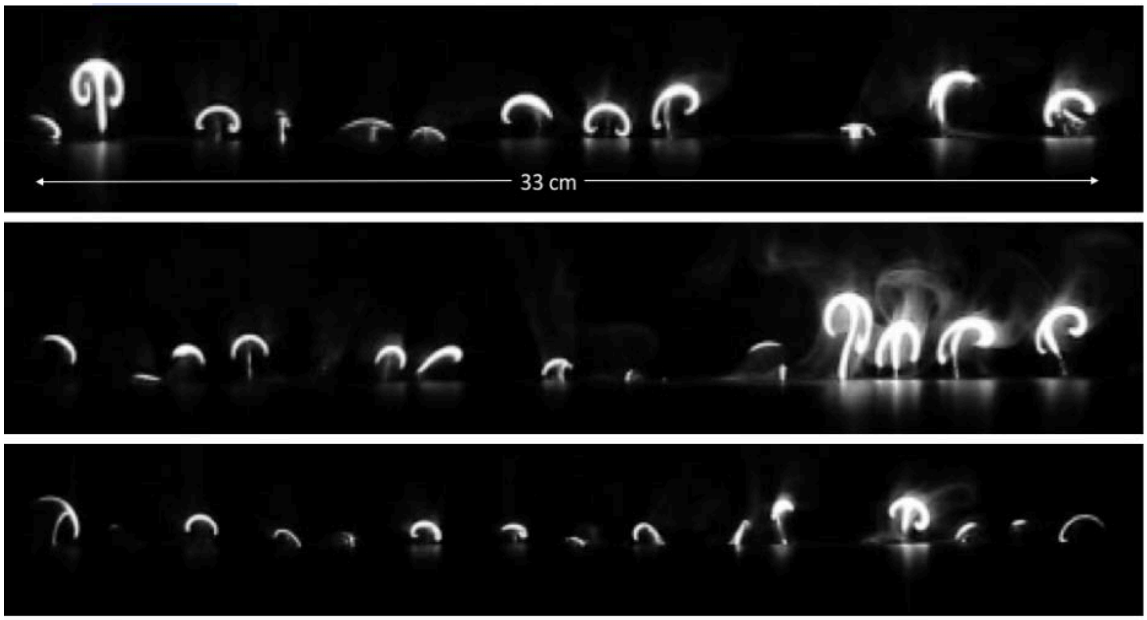

- x = 4 cm:

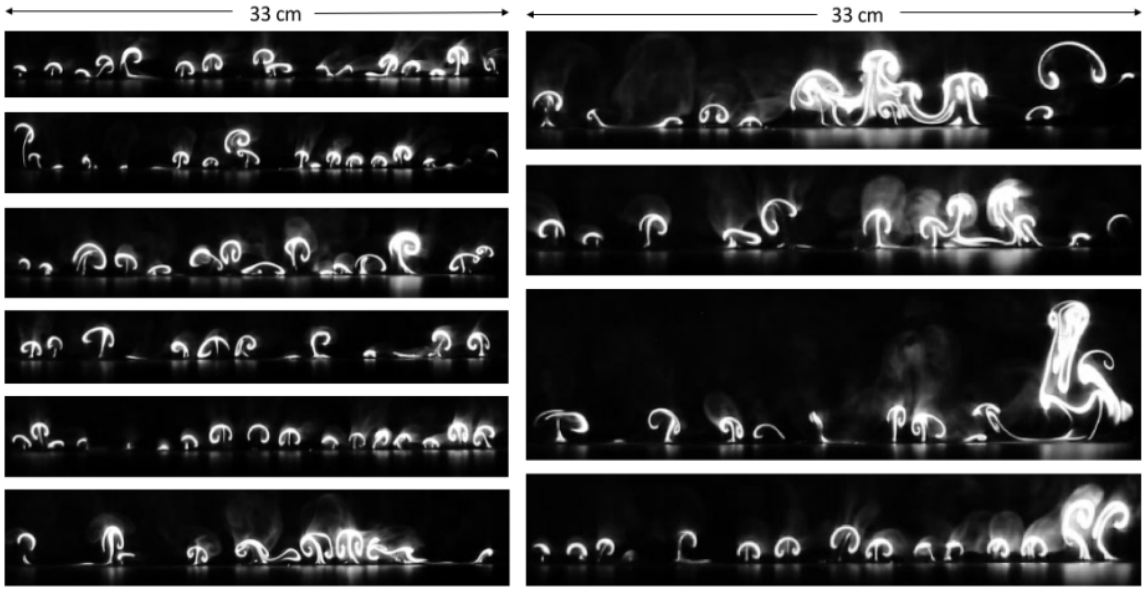

- x = 6 cm:

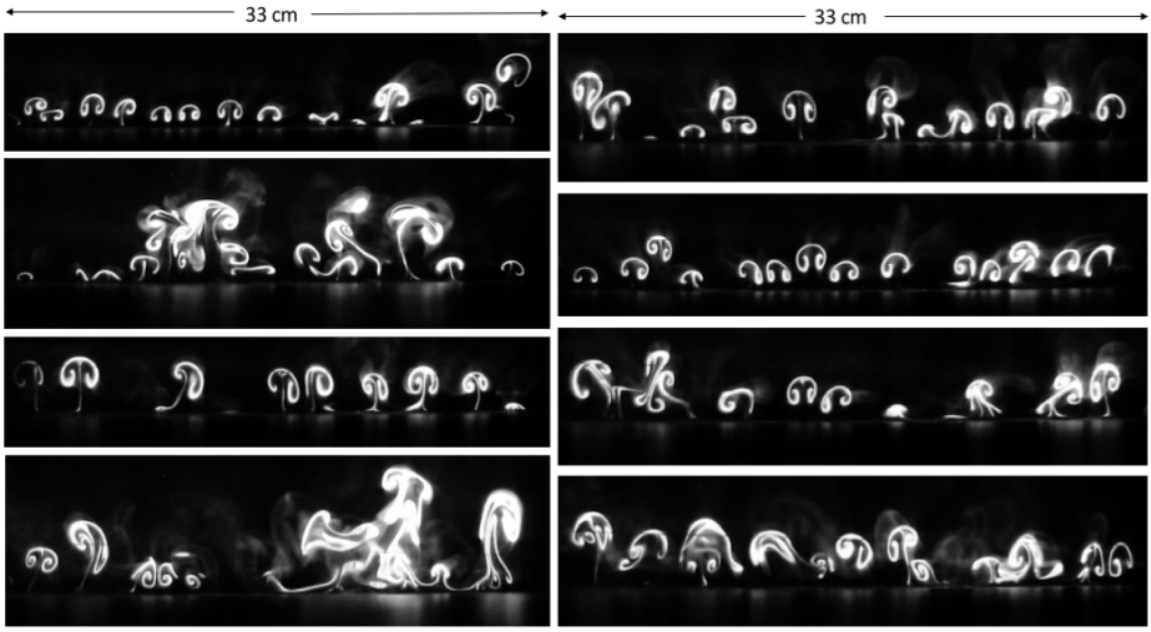

- x = 8 cm:

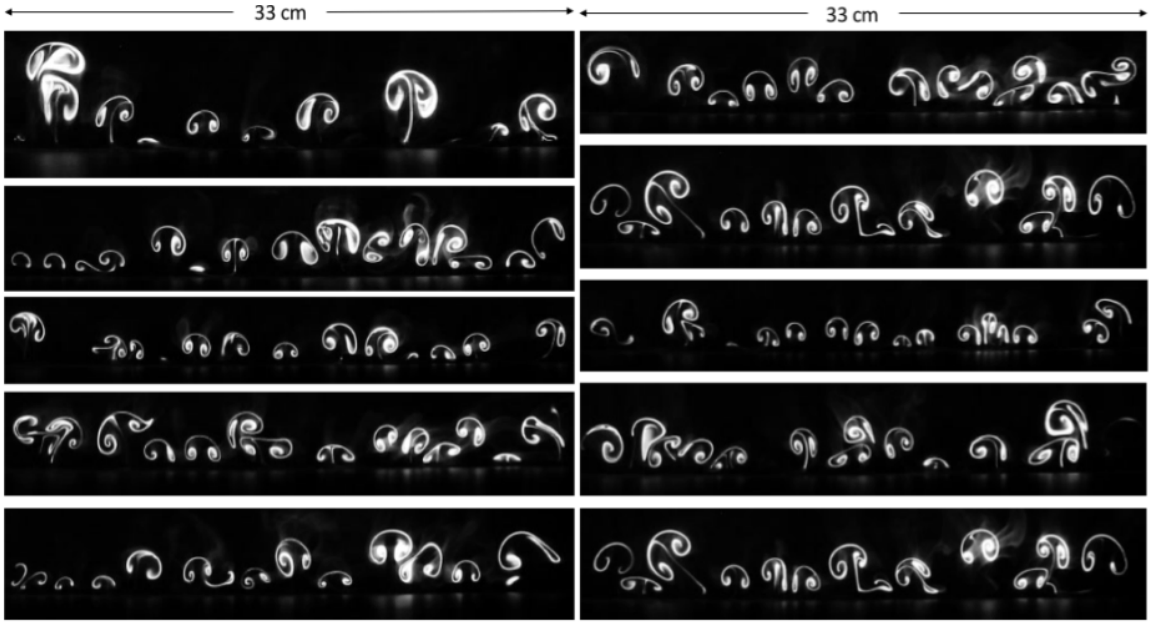

- x = 10 cm:

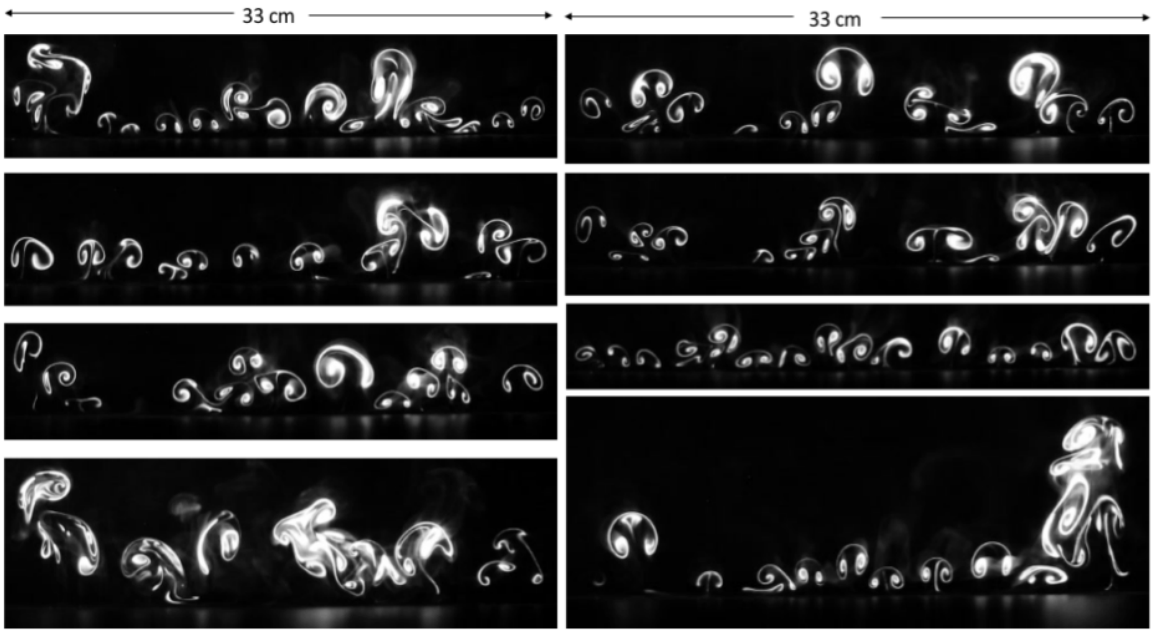

- x = 12 cm:

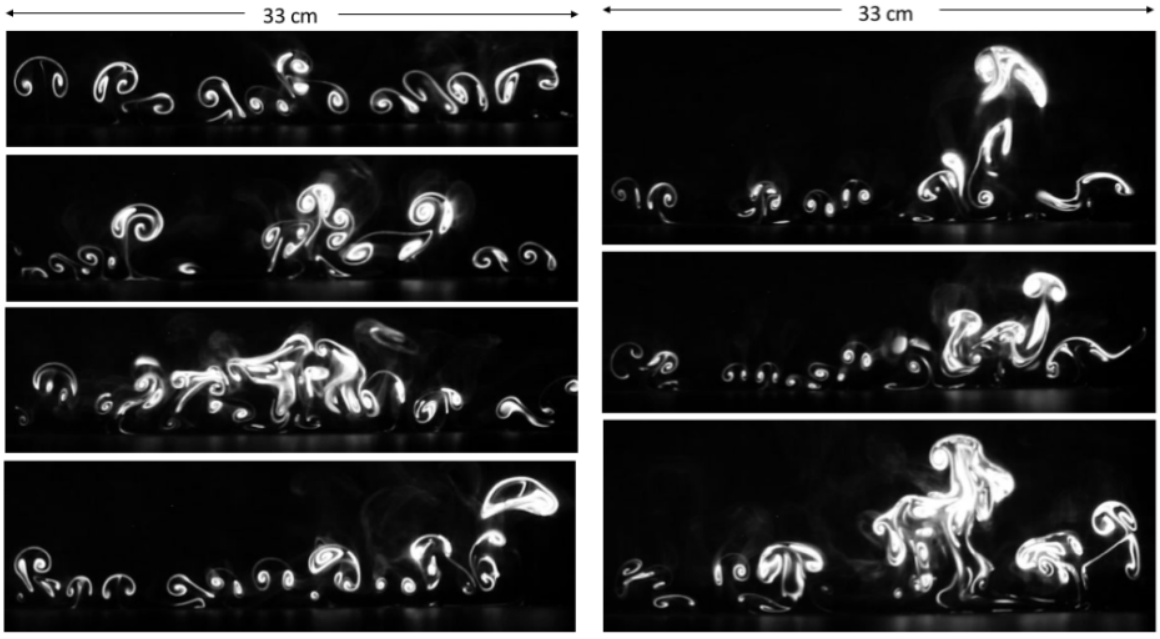

REFERENCES

1. S. Stein, S. Comas, J. Menakis, M. Carr, S. Stewart, H. Cleveland, L. Bramwell and V. Radeloff, "Wildfire, Wildlands, and People: Understanding and Preparing for Wildfire in the Wildland-Urban Interface," United States Department of Agriculture General Technical Report RMRS-GTR-299, 2013.

2. W. Covington and M. Moore, "Post settlement changes in natural fire regimes and forest structure: ecological restoration of old-growth ponderosa pine forests," Journal of Sustainable Forestry, vol. 2, no. 1-2, pp. 153-181, 1994.

3. S. Lee, "Controlling Forest Successions at Lake Itasca, Minnesota," Botanical Gazette, vol. 78, no. 2, pp. 129-174, Oct., 1924.

4. M. Rolston, "Water-impermeable seed dormancy," Botanical Review, vol. 44, pp. 365-396, 1978.

5. H. Chapman, "Prescribed burning versus public forest fire services," Journal of Forestry, vol. 45, no. 11, pp. 804-808, 1947.

6. H. Hanson, "Fire in land use and management," American Midland Naturalist, vol. 21, no. 2, pp. 415-434, 1939.

7. G. Hoxie, "How Fire Helps Forestry: The Practical vs. The Federal Government's Theoretical Ideas," Sunset, vol. 25, no. 7, pp. 145-151, August 1910.

8. J. Larsen, "Fires and forest succession in the Bitterroot Mountains of northern Idaho," Ecology, vol. 10, no. 1, pp. 67-76, 1929.

9. H. Weaver, "Fire as an ecological and silvicultural factor in the ponderosa-pine region of the pacific slope," Journal of Forestry, vol. 41, no. 1, pp. 7-15, 1943.

10. S. Stephens and L. Ruth, "Federal forest-fire policy in the United States," Ecological applications, vol. 15, no. 2, pp. 532-542, 2005.

11. L. Laverty and J. Williams, "Protecting people and sustaining resources in fire adapted ecosystems: a cohesive strategy," Forest Service, 2000.

12. E. Noonan-Wright, T. Opperman, M. Finney, G. Zimmerman, R. Seli, L. Elenz and D. Calkin, "Developing the U.S. Fire Decision Support System (WFDSS)," Journal of Combustion, 2011.

13. M. Gollner, F. Williams and A. Rangwala, "Upward flame spread over corrugated cardboard," Combustion and Flame, vol. 158, no. 7, pp. 1404-1412, 2011.

14. M. Finney, J. Cohen, S. McAllister and W. Jolly, "On the need for a theory of wildland fire spread," International Journal of Wildland Fire, vol. 22, no. 1, pp. 25-36, 2013.

15. D. Calkin, K. Gebert, J. Jones and R. Neilson, "Forest Service large fire area burned and suppression expenditure trends, 1970–2002," Journal of Forestry, vol. 103, no. 4, pp. 179-183, 2005.

16. R. Rothermel, "A mathematical model for predicting fire spread in wildland fuels," USDA Forest Service, Ogden, UT, 1972.

17. J. Scott and R. Burgan, "Standard fire behavior fuel models: a comprehensive set for use with Rothermel's surface fire spread model," USDA Forest Service, Rocky Mountain Research Station, RMRS-GTR-153, 2005.

18. C. Fernandez-Pello and T. Hirano, "Controlling mechanisms of flame spread," Combustion Science and Technology, vol. 32, no. 1-4, pp. 1-31, 1983.

19. M. Grishin, V. Zima, V. Kuznetsov and A. Skorik, "Ignition of combustible forest materials by radiant heat flux," Combustion, Explosions, and Shock Waves, vol. 38, pp. 24-29, 2002.

20. P. Mindykowski, A. Fuentes, J. Consalvi and B. Porterie, "Piloted ignition of wildland fuels," Fire Safety Journal, vol. 46, no. 1, pp. 34-40, 2011.

21. J. Fangrat, Y. Hasemi, M. Yoshida and T. Hirate, "Surface temperature at ignition of wooden based slabs," Fire Safety Journal, vol. 27, pp. 249-259, 1996.

22. J. Toreo, "Flaming ignition of solid fuels," in SFPE Handbook of Fire Protection Engineering, Quincy, MA, National Fire Protection Association, 2008, pp. 2-260-2-277.

23. S. Pyne, P. Andrews and R. Laven, Introduction to Wildland Fires, Second ed., New York, NY: John Wiley & Sons Inc., 2000.

24. F. Steward, "Fire Spread Through a Fuel Bed," in Heat Transfer in Fires: Thermo-Physics, Social Aspects, Economic Impact, Halsted Press, 1974, pp. 315-378.

25. F. Albini, "A model for fire spread in wildland fuels by radiation," Combustion Science and Technology, vol. 42, pp. 229-258, 1985.

26. G. Carrier, F. Fendell and M. Wolff, "Wind-aided fire spread across arrays of discrete fuel elements I. Theory," Combustion Science and Technology, vol. 75, pp. 31-51, 1991.

27. W. Catchpole, E. Catchpole and R. Rothermel, "Fire behavior experiments in mixed fuel complexes," International Journal of Wildland Fire, vol. 3, pp. 45-47, 1993.

28. W. Catchpole, E. Catchpole, B. Butler, R. Rothermel, G. Morris and D. Latham, "Rate of spread of free-burning fires in woody fuels in a wind tunnel," Combustion Science and Technology, vol. 131, pp. 1-37, 1998.

29. H. Emmons, "Fire in the forest," Fire Rescue, vol. 5, no. 3, pp. 163-178, 1964.

30. W. Frandsen, "Fire spread through porous fuels from the conservation of energy," Combustion and Flame, vol. 16, pp. 9-16, 1971.

31. H. Hottel, G. Williams and F. Steward, "The modeling of fire spread through a fuel bed," in Tenth International Symposium on Combustion, Pittsburgh, 1965.

32. H. Hottel, G. Williams and G. Kwentus, "Fuel pre-heating in free burning fires," in Thirteenth International Symposium on Combustion, Salt Lake City, 1971.

33. N. Kurbatskiy and G. Telitsin, "Theoretical and experimental analysis of the radiation mechanisms for the spread of forest fires," in Characteristics of the Process of Combustion in Forests, 1977, pp. 1-33.

34. H. Telisin, "Flame radiation as a mechanism of fire spread in forest," in Heat Transfer in Flames, New York, John Wiley & Sons Inc., 1974.

35. P. Thomas, "Some aspects of the growth and spread of fire in the open," Forestry, vol. 40, no. 2, pp. 139-164, 1967.

36. E. Brehob and A. Kulkarni, "Experimental measurements of upward flame spread on a vertical wall with external radiation," Fire Safety Journal, vol. 31, no. 3, pp. 181-200, 1998.

37. E. Brehob, C. Kim and A. Kulkarni, "Numerical model of upward flame spread on practical wall materials," Fire Safety Journal, vol. 36, no. 3, pp. 225-240, 2001.

38. F. Steward, "A mechanistic fire spread model," Combustion Science and Technology, vol. 4, no. 1, pp. 177-186, 1971.

39. H. Anderson, "Heat transfer and fire spread," USDA Forest Service, Intermountain Forest and Range Experiment Station, Ogden, 1969.

40. T. Beer, "The interaction of wind and fire," Boundary-Layer Meteorology, vol. 54, pp. 287-308, 1990.

41. G. Byram, H. Clements, E. Elliott and P. George, "An experimental study of model fires," USDA Forest Service, Southeastern Forest Experiment Station, Southern Forest Fire Laboratory, Macon, 1964.

42. R. McCarter and A. Broido, "Radiative and convective energy from wood crib fires," Pyrodynamics, vol. 2, pp. 65-68, 1965.

43. W. Pitts, "Wind effects on fires," Progress in Energy and Combustion Science, vol. 17, pp. 83-134, 1991.

44. A. Van Wagner, "Conditions for the start and spread of crown fire," Canadian Journal of Forest Research, vol. 7, pp. 23-34, 1977.

45. L. Sullivan, "Wildland surface fire spread modeling, 1990-2007. 1. Physical and quasi-physical models," International Journal of Wildland Fire, vol. 18, pp. 349-368, 2009.

46. R. Weber, "Modeling fire spread through fuel beds," Progress in Energy and Combustion Science, vol. 17, pp. 67-82, 1991.

47. R. Emori, Y. Iguchi, K. Saito and I. Wichman, "Simplified scale modeling of turbulent flame spread with implication to wildland fires," in Fire Safety Science - Proceedings of the Second International Symposium, 1988.

48. B. Adam, N. Akafuah, M. Finney, J. Forthofer and K. Saito, "A Study of Flame Spread in Engineered Cardboard Fuelbeds, Part II: Scaling Law Approach," in Progress in Scale Modeling, Volume 2, K. Saito, A. Ito, Y. Nakamura, and K. Kuwana, Eds., Cham, Switzerland, Springer, 2014, pp. 85-96.

49. B. Butler, J. Cohen, D. Latham, P. Schuette, K. Shannon, D. Jimenez and L. Bradshaw, "Measurements of radiant emissive power and temperatures in crown fires," Canadian Journal of Forest Research, vol. 34, no. 8, pp. 1577-1587, 2004.

50. R. Emori and K. Saito, "A study of scaling laws in pool and crib fires," Combustion Science and Technology, vol. 31, no. 5-6, pp. 217-230, 1983.

51. H. Bamford, J. Crank and D. Malan, "The combustion of wood, Part I," In Mathematical Proceedings of the Cambridge Philosophical Society, vol. 42, no. 2, pp. 166-182, 1946.

52. T. Astarita, G. Cardone, G. Carlomagno and C. Meola, "A survey on infrared thermography for convective heat transfer measurements," Optics and Laser Technology, vol. 32, no. 7-8, pp. 593-610, 2000.

53. G. Holst, Common Sense Approach to Thermal Imaging, Winter Park: JCD Publishing, 2000.

54. A. Arakawa, K. Saito and W. Gruver, "Automated Infrared Imaging Temperature Measurement with Application to Upward Flame Spread Studies. Part 1," Combustion and Flame, vol. 92, pp. 222-230, 1993.

55. C. Qian, H. Ishida and K. Saito, "Upward Flame Spread along PMMA Vertical Corner Walls Part II: Mechanism of "M" Shape Pyrolysis Front Formation," Combustion and Flame, vol. 99, pp. 331-338, 1994.

56. M. M. Delichatsios, M. A. Delichatsios, G. Lougheed, G. Crampton, C. Qian, H. Ishida and K. Saito, "Effect of external radiant heat flux on upward fire spread

and fire growth on plywood," Fire Safety Science - Fourth International Symposium, pp. 421-432, 1994.

57. M. Omar, M. Hassan and K. Saito, "Optimizing thermography depth probing with a dynamic thermal point spread function," Infrared Physics & Technology, vol. 46, pp. 506-514, 2005.

58. M. Finney, J. Forthofer, I. Grenfell, B. Adam, N. Akafuah, and K. Saito, “A study of flame spread in engineered cardboard fuel beds, Part I: Correlations and Observations,” Progress in Scale Modeling Volume II: 71-83, Springer, 2014.

59. M. Finney, J. Cohen, J. Forthofer, S. McAllister, M. Gollner, D. Gorham, K. Saito, N. Akafuah, B. Adam, J. English, “The role of buoyant flame dynamics in wildfire spread,” Proc. The National Academy of Sciences, 2015. Early version was published: http://www.pnas.org/content/112/32/9833

60. D. Frankman et al. (2013) "Measurements of convective and radiative heating in wildland fires." Int J Wildland Fire 22:157–167.

61. C. Lin, Hydrodynamic stability, Cambridge: Cambridge University Press, 1955.

62. E. Fendell and M. Wolff, "Wind-Aided Fire Spread," in Forest Fires: Behavior and Ecological Effects, E. A. Johnson and K. Miyanishi, Eds., San Diego, Academic Press, 2001, pp. 171-224.

63. G. Gaydon and H. Wolfhard, Flames: Their Structure, Radiation, and Temperature, 4th ed., New York: Halsted Press, a Division of John Wiley & Sons, Inc., Fourth edition (revised) 1979.

64. J. Buckmaster, "An Introduction to Combustion Theory," in The Mathematics of Combustion, J. Buckmaster, Ed., Philadelphia, Siam, 1985, pp. 3 - 46.

65. D. Tillman, A. Rossi and W. Kitto, Wood combustion: Principles, Processes and Economics, New York: Academic Press, 1981.

66. B. Cetegen and Y. Dong, "Experiments on the instability modes of buoyant diffusion flames and effects of ambient atmosphere on the instabilities," Experiments in Fluids, vol. 28, no. 6, pp. 546-558, 2000.

67. X. Jiang and K. Luo, "Dynamics and structure of transitional buoyant jet diffusion flames with side-wall effects," Combustion and Flame, vol. 133, no. 1, pp. 29- 45, 2003.

68. H. Gotoda, Y. Asano, K. Chuah and G. Kushida, "Nonlinear analysis on dynamic behavior of buoyancy-induced flame oscillation under swirling flow," International Journal of Heat and Mass Transfer, vol. 52, no. 23, pp. 5423-5432, 2009.

69. R. Banta, L. Olivier, E. Holloway, R. Kropfli, B. Bartram, R. Cupp and M. Post, "Smoke-column observations from two forest fires using Doppler lidar and Doppler radar," Journal of Applied Meteorology, vol. 31, no. 11, pp. 1328-1349, 1992.

70. T. Clark, L. Radke, J. Coen and D. Middleton, "Analysis of small-scale convective dynamics in a crown fire using infrared video camera imagery," Journal of Applied Meteorology, vol. 38, no. 10, pp. 1401-1420, 1999.

71. J. Coen, S. Mahalingam and J. Daily, "Infrared imagery of crown-fire dynamics during FROSTFIRE," Journal of Applied Meteorology, vol. 43, no. 9, pp. 1241-1259, 2004.

72. A. Bejan, "Plumes," in Convection Heat Transfer, third ed., Hoboken, New Jersey: John Wiley & Sons, Inc., 2004, pp. 430-439.

73. V. Kottke, "Taylor–Görtler vortices and their effect on heat and mass transfer," in Proceedings of the Eighth International Heat Transfer Conference, San Francisco, CA, 1986.

74. P. McCormack, H. Welker and M. Kelleher, "Taylor-Görtler vortices and their effect on heat transfer," Journal of Heat Transfer, vol. 92, pp. 101-112, 1970.

75. Data generated and provided by United States Department of Agriculture, Forest Service Rocky Mountain Research Station.

76. K. Saito, J. Quintiere and F. Williams, "Upward turbulent flame spread," in Fire Safety Science Proceedings of the First International Symposium, Washington, 1985.

77. W. Anderson, E. Catchpole and B. Butler, "Convective heat transfer in fire spread through fine fuel beds," International Journal of Wildland Fire, vol. 19, no. 3, pp. 284-298, 2010.

78. M. Byram and R. Martin, "Fire whirlwinds in the laboratory," Fire Control Notes, vol. 33, no. 1, p. 13–17, 1962.

79. M. M. Delichatsios, M. A. Delichatsios, G. Lougheed, G. Crampton, C. Qian, H. Ishida and K. Saito, "Effect of external radiant heat flux on upward fire spread: Measurements on plywood and numerical predictions," in Fire Safety Science-Proceedings of the Fourth International Symposium, Washington, 1995.

80. M. Zabetakis, "Flammability Characteristics of Combustible Gases and Vapors," The United States Bureau of Mines, Washington, 1965.

81. S. Soma and K. Saito, "Reconstruction of fire whirls using scale models," Combustion and Flame, vol. 86, no. 3, p. 269–284, 1991.

82. R. Emori and K. Saito, "Model rules on motion of smoke and gases in building fires," Bulletin Japanese Association of Fire Science and Engineering, vol. 29, no 2. In Japanese, pp. 41 - 49, 1979.

83. K. Saito and M. Finney, "Scale Modeling in Combustion and Fire Research," Journal of the Combustion Society of Japan, vol. 56, no. 177, pp. 194-204, 2014.

84. R. Emori and D. Schuring, Scale Models in Engineering, Fundamentals and Applications, Pergamon Press, 1977.

85. C. Hottel, "Fire modeling," Proceedings of the International Symposium on the Use of Models in Fire Research, vol. 786, pp. 32-47, 9-10 November 1959.

86. W. Berl, "First International Symposium on Fire Research," in International Symposium on the Use of Models in Fire Research, Washington D.C., 1959.

87. I. Barenblatt, Scaling, Cambridge: Cambridge University Press, 2003.

88. W. Baker, P. Westine and F. Dodge, Similarity methods in engineering dynamics: Theory and practice of scale modeling, Rochelle Park, New Jersey: Spartan Books, 1973.

89. L. Langhaar, Dimensional analysis and theory of models, vol. 2, New York: Wiley, 1951.

90. B. Adam, Incorporating dynamic flame behavior into the scaling laws of wildland fire spread (Doctoral dissertation), Department of Mechanical Engineering, University of Kentucky, 2015.

91. K. Saito ed. "Progress in scale modeling: summary of the first international symposium on scale modeling (ISSM in 1988) and selected papers from subsequent symposia (ISSM II in 1997 through ISSM V in 2006)," in ISSM, 2008.

92. R. Emori, "Analytical Approach to Automobile Collisions," SAE Technical Paper 680016, 1968.

93. E. Buckingham, "On physically similar systems; illustrations of the use of dimensional equations," Physical Review, vol. 4, no. 4, pp. 345-376, 1914.

94. A. Sonin, The Physical Basis of Dimensional Analysis, Second ed., Cambridge, MA, 2001.

95. D. Riabouchinsky., "Méthode des variables de dimensions zéro et son application en aérodynamique," L'Aérophile, vol. 19, p. 407–408, 1911.

96. E. Macagno, "Historico-critical review of dimensional analysis," Journal of the Franklin Institute, vol. 292, no. 6, pp. 391-402, 1971.

97. F. Williams, "Scaling mass fires," Fire Research Abstracts and Reviews, vol. 11, pp. 1-23, 1969.

98. M. Finney, J. Cohen, J. Forthofer, S. McAllister, B. Adam, N. Akafuah, J. English, K. Saito, D. Gorham, and M. Gollner, "Experimental evidence of buoyancy controlled flame spread in wildland fires," in Advances in Forest Fire Research, Coimbra, 2014.

99. G. Taylor, "Fire under influence of natural convection," Proceedings of the International Symposium on the Use of Models in Fire Research, pp. 10-32, 9- 10 November 1961.

100. R. Emori and K. Saito, "Model experiment of hazardous forest fire whirl," Fire Technology, vol. 18, pp. 319 - 327, 1982.

101. R. Emori and K. Saito, "A unified view of scaling laws in fires (First report): Scaling laws in stationary fires," Transactions of JSME, Vols. 29, Series B, no. in Japanese, pp. 1892 - 1898, 1985.

102. D. Spalding, "Colloquium on Modeling Principles: The art of partial modeling," Proceedings of the Combustion Institute, vol. 9, no. 1, pp. 833-843, 1963.

103. H. Emmons and T. Shen, "Fire spread in paper arrays," Symposium (International) on Combustion, vol. 13, no. 1, pp. 917-926, 1971.

104. H. Emmons, "Some observations on pool burning," In International Symposium on the Use of Models in Fire Research, pp. 50-67, 9-10 November 1959.

105. K. Saito and F. Williams, "Scale Modeling in the Age of High-Speed Computation," in Progress in Scale Modeling, Volume II, K. Saito, A. Ito, Y. Nakamura and K. Kuwana, Eds., New York, Springer International Publishing, 2014, pp. 1-18.

106. G. Heskestad, "Virtual origins of fire plumes," Fire Safety Journal, vol. 5, no. 2, pp. 109-114, 1983.

107. K. Saito, "Forest Fires: Behavior and Ecological Effects," in Forest Fires: Behavior and Ecological Effects, E. Johnson and K. Miyanishi, Eds., San Diego, CA, Academic Press, 2001, pp. 11-54.

108. C. Clements, B. Potter and S. Zhong, "In situ measurements of water vapor, heat, and CO2 fluxes within a prescribed grass fire," International Journal of Wildland Fire, vol. 15, no. 3, pp. 299-306, 2006.

109. R. Weber, "Modelling fire spread through fuel beds," Progress in Energy and Combustion Science, vol. 17, no. 1, pp. 67-82, 1991.

110. S. Taylor, B. Wotton, M. Alexander and G. Dalrymple, "Variation in wind and crown fire behavior in a northern jack pine black spruce forest," Canadian Journal of Forest Research, vol. 34, no. 8, pp. 1561-1576, 2004.

111. R. Raupach, J. Finnigan and Y. Brunei, "Coherent eddies and turbulence in vegetation canopies: the mixing-layer analogy," Boundary-Layer Meteorology, vol. 78, no. 3-4, pp. 351-382, 1996.

112. P. Cunningham, "Numerical simulations of grass fires using a coupled atmosphere-fire model: Dynamics of fire spread," Journal of Geophysical Research: Atmospheres (1984–2012), vol. 112, no. D5, pp. 1-17, 2007.

113. J. Cohen and M. Finney, "Fine fuel particle heating during experimental laboratory fires," in Advances in Forest Fire Research, Coimbra, 2014.

114. K. Saito, A. Ito, Y. Nakamura and K. Kuwana Edited, Progress in Scale Modeling, Volume II, Springer, 2014.

115. K. Saito, Personal Communication, Director of the Institute of Research for Technology Development, University of Kentucky, 2016.

116. J. English, Heat Transfer Characteristics in Wildland Fuelbeds (Master's Thesis), Department of Mechanical Engineering, University of Kentucky, 2014.

117. X. Maldague, T. Jones, H. Kaplan, S. Marinetti and M. Prystay "Chapter 2: Fundamentals of Infrared and Thermal Testing: Part 1. Principles of Infrared and Thermal Testing," in Nondestructive Handbook, Infrared and Thermal Testing, Volume 3, X. Maldague technical ed., P. Moore ed., 3rd edition, Columbus, Ohio, ASNT Press, 2001.

118. V. Poryev, G. Poryev, "Experimental determination of the temperature range of a television pyrometer," Journal of Optical Technology 71 (1), pp. 70–71, 2004.

119. A. Kylili, P. Fokaides, P. Christou, S. Kalogirou "Infrared thermography (IRT) applications for building diagnostics: A review," Applied Energy, 2014.

120. P. Tipler, "Relative intensity of reflected and transmitted light," Physics for Scientists and Engineers, Parts 1-35, Part 39 (4th ed.), Macmillan. p. 1044. ISBN 0-7167-3821-X, 1999.

121. M. Kaviany, "Figure 4.3(b) Radiation properties of an opaque surface," Principles of heat transfer. Wiley-IEEE. p. 381. ISBN 0-471-43463-9, 2002.

122. B. Venkanna, "§10.3.4 Absorptivity, reflectivity, and transmissivity". Fundamentals of heat and mass transfer. PHI Learning Pvt. Ltd. pp. 385–386. ISBN 81-203-4031-0, 2010.

123. J. Trefil, The Nature of Science: An A-Z Guide to the Laws and Principles Governing Our Universe. Houghton Mifflin Harcourt. p. 377. ISBN 9780618319381, 2003.

124. Emissivity Coefficients of Some Common Materials. Engineering Toolbox. Retrieved from http://www.engineeringtoolbox.com/emissivity-coefficients-d_447.html

125. Emissivity Values for Common Materials. Thermography. Retrieved from http://www.infrared-thermography.com/material-1.htm

126. Emissivity Table. Thermo works. Retrieved from http://www.thermoworks.com/emissivity_table.html

VITA

Author's Name

Nikolay Gustenyov

Education

Master of Science in Mechanical Engineering

University of Kentucky

May 2016

Bachelor of Engineering in Mechanical Engineering

Lancaster University, Great Britain

July 2014

Associate Degree in "Repair, Maintenance and Exploitation of Automotive Transport"

College of Automotive Transport of Kostanay, Kazakhstan

July 2010

Experience

University of Kentucky

Lexington, KY

August 2014 – May 2016

Graduate Research Assistant, Institute of Research for Technology Development (IR4TD)

University of Kentucky

Lexington, KY

June 2013 – October 2013

Research Assistant, Institute of Research for Technology Development (IR4TD)

Concrete Products Supplier

Kostanay, Kazakhstan

September 2010 – October 2011
Manager

Car Care Center
Kostanay, Kazakhstan
June 2007 – August 2010
Mechanic

Submitted Publications

N. Gustenyov, N. Akafuah, A. Salaimeh, K. Saito, M. Finney and S. McAllister. Flow Visualization of Buoyant Instability in a Cross-Flow: An implication for Flame Spread over Forest Fuel Beds. *36th International Symposium on Combustion*. 2016. Seoul

K. Seevers, N. Akafuah, D. Seevers, E. Hall, N. Gustenyov. Understanding Heat Transfer Mechanisms for Firefighter Protection in a High-Temperature Fine Fuel Particle Environment. *2016 Spring Technical Meeting Central States Section of the Combustion Institute*. Knoxville.

Awards and Certificates

Institution Best Student Certificate, *Institution of Mechanical Engineers*, Great Britain (2014)
Lean Systems Student Certificate, *University of Kentucky* (2015)

Society Memberships

University of Kentucky Judo Club (2012 – present)
University of Kentucky Racing Team (2012 – 2013)
Lancaster University Judo Club (2011 – 2014)
Lancaster University MMA Club (2011 – 2014)
Lancaster University Brazilian Jiu Jitsu Society (2013 – 2014)